ANNUAL REPORT 1998

DEPARTMENT
OF
OPTOELECTRONICS

UNIVERSITY OF ULM

Contents

Department of Optoelectronics University of Ulm

Albert-Einstein-Allee 45, D-89069 Ulm, Germany
+49–731/50–
Fax: 2 60 49
Phone: +49–731/50–

Head of Department:			
Prof. Dr.	Karl Joachim Ebeling	–2 60 51	karl.ebeling@e-technik.uni-ulm.de
Assistant Head of Department:			
Prof. Dr.	Peter Unger	–2 60 54	unger@sunrise.e-technik.uni-ulm.de
Cleanroom Management:			
Dr.-Ing.	Jürgen Mähnß	–2 60 53	juergen.maehnss@e-technik.uni-ulm.de
Senior Research Assistant:			
Dr.-Ing.	Rainer Michalzik	–2 60 48	rainer.michalzik@e-technik.uni-ulm.de
Secretaries:			
	Christine Bunk	–2 60 50	karl.ebeling@e-technik.uni-ulm.de
	Sükran Kilic	–2 60 59	
Research Staff:			
Dipl.-Phys.	Hin Yiu Anthony Chung	–2 60 43	hin-yin.chung@e-technik.uni-ulm.de
Dipl.-Ing.	Eckard Deichsel	–2 60 57	eckard.deichsel@e-technik.uni-ulm.de
Dipl.-Ing.	Franz Eberhard	–2 60 39	franz.eberhard@e-technik.uni-ulm.de
Dipl.-Ing.	Irene Ecker	–2 60 41	irene.ecker@e-technik.uni-ulm.de
Dipl.-Ing.	Matthias Golling	–2 60 43	matthias.golling@e-technik.uni-ulm.de
Dipl.-Ing.	Martin Grabherr	–2 60 36	martin.grabherr@e-technik.uni-ulm.de
Dipl.-Phys.	Roland Jäger	–2 60 40	roland.jaeger@e-technik.uni-ulm.de
Dipl.-Ing.	Jürgen Joos	–2 60 35	juergen.joos@e-technik.uni-ulm.de
Dipl.-Phys.	Günter Jost	–2 60 46	guenter.jost@e-technik.uni-ulm.de
Dr.rer.nat.	Markus Kamp	–2 64 54	kamp@sunrise.e-technik.uni-ulm.de
Dipl.-Ing.	Roger King	–2 60 35	roger.king@e-technik.uni-ulm.de
Dipl.-Ing.	Christoph Kirchner	–2 60 40	christoph.kirchner@e-technik.uni-ulm.de
Dipl.-Ing.	Thomas Kndl	–2 60 35	thomas.knoedl@e-technik.uni-ulm.de
M.S.	Safwat William Mahmoud	–2 60 44	safwat.mahmoud@e-technik.uni-ulm.de
Dipl.-Ing.	Felix Mederer	–2 60 37	felix.mederer@e-technik.uni-ulm.de
Dipl.-Ing.	Ulrich Martin	–2 60 38	ulrich.martin@e-technik.uni-ulm.de
Dipl.-Phys.	Michael Miller	–2 60 36	michael.miller@e-technik.uni-ulm.de
Dipl.-Phys.	Markus Schauler	–2 60 39	markus.schauler@e-technik.uni-ulm.de
Dipl.-Ing.	Wolfgang Schmid	–2 60 44	wolfgang.schmid@e-technik.uni-ulm.de
Dipl.-Phys.	Peter Schnitzer	–2 60 37	peter.schnitzer@e-technik.uni-ulm.de
Dipl.-Ing.	Veit Schwegler	–2 60 66	veit.schwegler@e-technik.uni-ulm.de
Dr.-Ing.	Georgi Stareev	–2 60 43	georgi.stareev@e-technik.uni-ulm.de
Dipl.-Ing.	Heiko Johannes Unold	–2 60 36	heiko.unold@e-technik.uni-ulm.de
Technical Staff:			
	Susanne Menzel	–2 60 41	
	Sophie Pfetsch	–2 60 41	sophie.pfetsch@e-technik.uni-ulm.de
	Josef Theisz	–2 60 30	

Preface

The year 1998 was again very successful for the Department of Optoelectronics. Two major achievements of the VCSEL group, namely the diode cascade VCSEL and the high power VCSEL array were listed in the top developments in laser diode research in 1998 a s published by the III-V Compound Semiconductor Journal in its December 1998 issue. Peter Unger's group has developed high-power single-mode selectively oxidized edge-emitting laser diodes with record performance. Markus Kamp's group used homoepitaxy to demonstrate narrowest photoluminescence lines in GaN and to obtain pn-junction light emitting diodes on GaN bulk substrates for the first time world wide. The systems group achieved 12.5 Gb/s optical data transmission over various types of fiber. More hi ghlights are to be found in the various contributions in this review.

The Department was delighted to host world-famous Dr. Shuji Nakamura from Nichia Chemicals, Japan, and Prof. Dr. Alexander E. Junovich from Moscow State University, Russia, as distinguished Guest Professors for a shorter and longer period, respectively. Three former members of the Department, Gernot Reiner, Dirck Sowada, and Klaus Faltin received their Dr.-Ing. degrees in electrical engineering. All three of them already held attractive positions in industry before they submitted the final version of their theses. In total 14 diploma theses and 5 semester projects were completed by the various students in the Department. Unfortunately, Margit Kohler, a most helpful, skilled, and friendly technical staff member left us for joining her husband in Munich.

As in recent years, close cooperation with industry, in particular in the areas of laser diodes and optical interconnects, joint projects granted by the Federal Ministry of Research and Technology as well as the European Community, and project support fr om the National Science Foundation and the Volkswagen Foundation form the basis for the high tech research of the Department. Excellent clean room facilities and laboratory equipment, funded by the local government, provide a favorable environment for co mpetitive research. Numerous invitations to international conferences and a large number of paper publications document the activities of the Department. A detailed list can be found at the end of the present review.

The Head of the Department still serves as an elected Vice-President of the University of Ulm. Unexpectedly, he was elected as a Regular Member of the Heidelberg Academy of Science.

Karl Joachim Ebeling January 1999

Fabrication and Characterization of Laser Diodes with Native Oxide as Surface Passivation

Eckard Deichsel

To simplify the fabrication sequence of broad-area lasers, the deposition of a surface passivation layer has been replaced by a self-aligning oxidation step. The oxide resistivity of 4 kΩcm^2 is comparable to a conventional Si_3N_4 passivation layer. Due to the self-aligning process, two lithography steps have been combined resulting in a reduced fabrication time. The device characteristics show optical output powers in cw operation of 2.4 W and wall-plug efficiencies of 55 %. The additional $Al_{0.8}Ga_{0.2}As$ layer does not influence the series resistance.

1. Introduction

High-power laser diodes offer lots of applications, for example the use in medical systems, pumping of solid state laser, and material processing. The increasing demand for such devices leads to enforced research. For manual fabrication in research laboratories a quick and easy process technology is desired.

The conventional fabrication sequence for broad-area lasers described in [1] usually needs five lithography steps which are required for ridge etching, surface passivation, p-contact metallization, electroplating, and top metallization. Additionally, four vacuum processes are necessary. To simplify and accelerate the fabrication, two changes to the existing fabrication process have been introduced. First, the surface passivation has been replaced by a self-aligning oxidation step. This saves one lithography step and one vacuum step. Secondly, the lithography steps for electroplating and top metallization have been combined. This also saves one lithography step. Compared to the conventional process, the effort needed for fabrication is reduced by 20 %.

2. Fabrication

A 200-nm-thick $Al_{0.8}Ga_{0.2}As$ layer is included under the highly-doped p-contact layer of the MBE-grown GRINSCH structure. The definition of the ridge is performed by wet-chemical etching. An accurate control of the etching depth is very important to avoid the removal of the $Al_{0.8}Ga_{0.2}As$ layer which is needed for the formation of the native oxide. The oxidation is performed in a 400 °C steam atmosphere. Due to lateral oxidation, the width of the contact area is reduced. However, for broad-area lasers this reduction is nearly negligible. The p contact is formed by a Ti/Pt/Au metallization. Fig. 1 schematically shows the laser structure with native oxide as surface passivation.

For combining electroplating and top metallization, a thick AZ photoresist treated with chlorobenzene before development provides good conditions, particularly with regard to the top-metallization lift-off step where negatively-sloped sidewalls are needed. After substrate thinning and n-contact metallization, the sample is cleaved into single lasers which are mounted junction-side down on a diamond heat spreader fixed on a copper submount.

The SEM micrographs of cleaved laser facets are shown in Fig. 2. The native oxide for surface passivation of the $Al_{0.8}Ga_{0.2}As$ is darker than the conductive $Al_{0.8}Ga_{0.2}As$ layer.

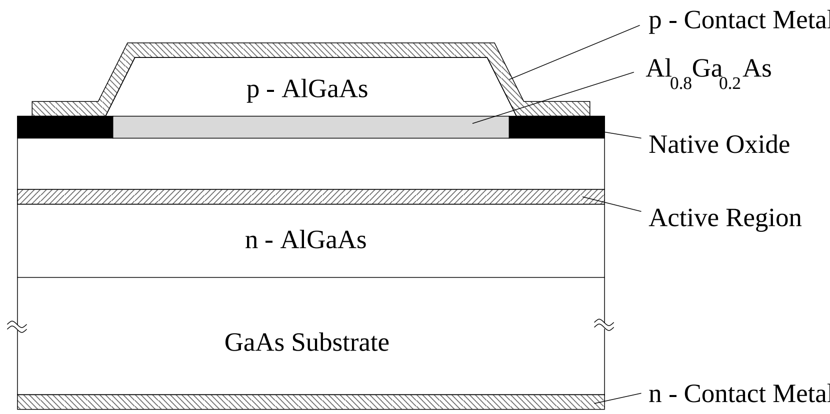

Fig. 1. Schematical view of a laser with native oxide as surface passivation.

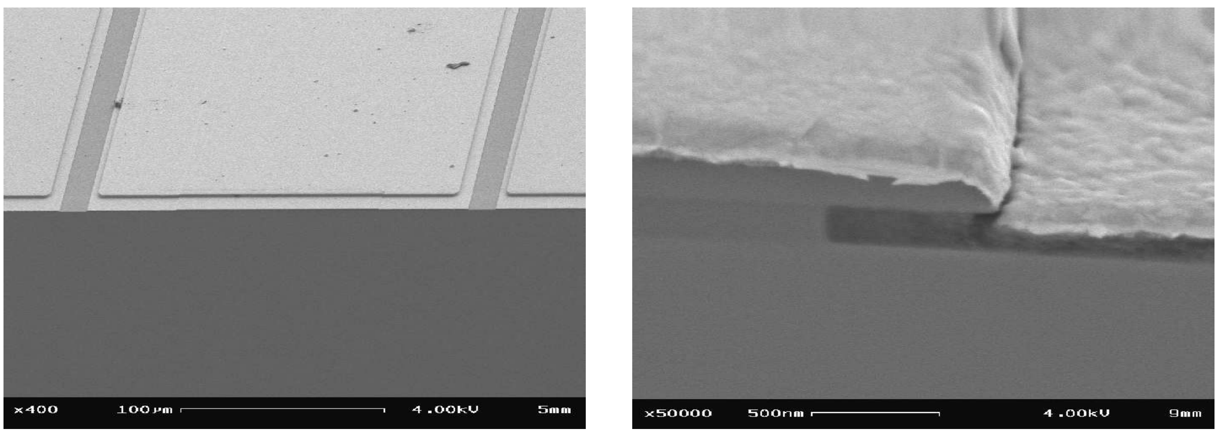

Fig. 2. SEM micrographs of cleaved facets of a 100-μm-wide broad-area laser. On the right side, the native oxide appears as darker areas.

3. Characterization

For the electrical characterization of the surface passivation, several 200 μm $\times$ 200 μm metallization pads on the native oxide have been applied with voltages up to 10 V. The leakage currents are shown in Fig. 3. The break-through voltages are above 10 V in each case. The specific series resistance is about 4 kΩcm^2 which is 7 orders of magnitude larger compared to the resistance of $2 \cdot 10^{-4}$ Ωcm^2 for a forward-biased laser diode. One sample shows a much deeper mesa etching than the other. Therefore, the native oxide was much thinner (about 50 nm instead 200 nm) which leads to increased leakage currents at voltages above 3 V and a break-through voltage of only 5 V. This proves the need for an accurately-controlled etching process. Additionally, a sample with a 120-nm-thick Si_3N_4 passivation layer has been measured showing similar series resistances and break-through voltages above 10 V.

The P-I and I-V characteristics of a 1000 μm $\times$ 100 μm laser measured at 18 °C with an integrating sphere are shown in Fig. 4. Optical output powers of 2.4 W have been achieved at 3 A. The threshold current is 135 mA and the differential resistance 165 mΩ. Also shown is the wall-plug efficiency which reaches values up to 55 %.

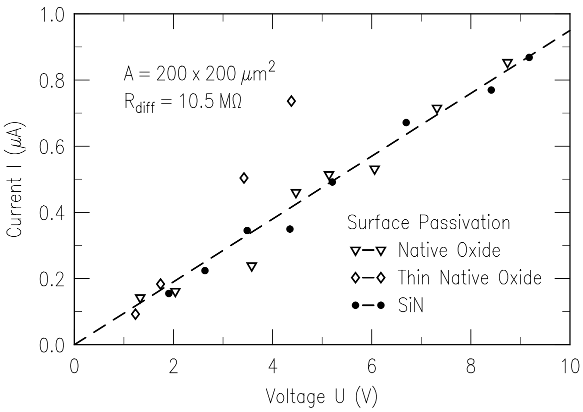

Fig. 3. Leakage currents for surface passivation with a normal (▿) and a very thin (◇) native oxide, and a 120-nm-thick Si_3N_4-passivation layer (●).

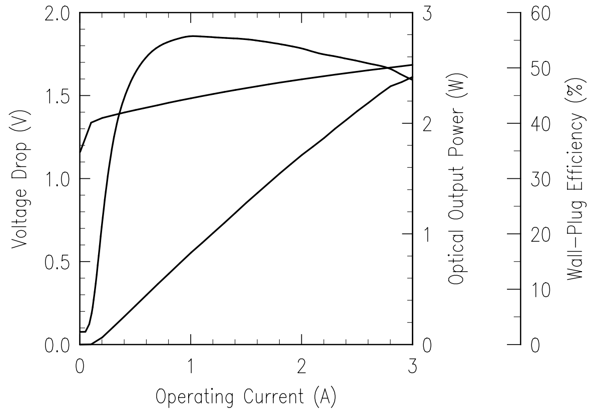

Fig. 4. P - I, I - V characteristics and wall-plug efficiency of a 1000 μm $\times$ 100 μm laser measured at 18 °C with an integrating sphere.

4. Summary

In conclusion, we have reduced the fabrication effort for broad-area laser diodes using a self-aligning oxidation process. The optical and electrical characteristics are not influenced by the 200-nm-thick $Al_{0.8}Ga_{0.2}As$ layer. Especially the series resistance does not increase noticeable compared to epitaxial material without the $Al_{0.8}Ga_{0.2}As$ layer.

References

[1] J. Heerlein, E. Schiehlen, R. Jäger, and P. Unger, "63 % wall-plug efficiency InGaAs/AlGaAs broad area laser diodes and arrays", in *Proc. CLEO/Europe 98, CThG2*, p. 267, Glasgow, UK, Sept., 1998.

12.5 Gbit/s data rate fiber transmission using single-mode selectively oxidized GaAs VCSELs at $\lambda = 850$ nm

Felix Mederer and Peter Schnitzer

We demonstrate for the first time 12.5 Gbit/s data rate fiber transmission using high performance single-mode GaAs VCSELs with 12.3 GHz modulation bandwidth. The bit-error rates remain better than 10^{-11} *for transmission of PRBS signals over 100 m multimode fiber and 1 km single-mode fiber, respectively.*

1. Introduction:

Over the past years vertical-cavity surface-emitting lasers (VCSELs) have become devices with excellent electrical and optical properties. Selective oxidation has led to VCSELs with threshold currents in the sub-100 μA range [1,2], low threshold voltages and high wallplug efficiencies [3], and modulation bandwidths of up to 21.5 GHz [4]. High bit rate data transmission of 10 Gbit/s over 500 m multimode fiber (MMF) using proton implanted InGaAs VCSELs [5] and 10 Gbit/s over 100 m MMF using oxidized InGaAs VCSELs [6] have been reported. These experiments show that VCSELs are very attractive light sources for fiber based local area networks like the Gigabit Ethernet standardized for data rates of 1 Gbit/s, 850 nm wavelength and 50 μm core diameter MMF of lengths up to 550 m [7]. The continuously increasing need to provide higher network capacities mainly initiated by the Internet boom will require even faster networks than the Gigabit Ethernet.
In this work, we report 12.5 Gbit/s data transmission over 100 m MMF and 1 km single-mode fiber (SMF) using single-mode selectively oxidized GaAs VCSELs emitting at 850 nm. In both cases the bit-error rate (BER) remains better than 10^{-11} for pseudo-random bit sequence (PRBS) transmission.

2. Device structure:

The one-wavelength thick inner cavity of the VCSEL contains three active GaAs-$Al_{0.2}Ga_{0.8}As$ quantum wells designed for 850 nm gain peak wavelength. Lateral current confinement is achieved by selective wet oxidation of a single 30 nm thick AlAs layer. This layer is shifted towards a node of the standing wave pattern in order to reduce the built-in effective index guiding and optical losses for increased single-mode output power. Polyimide passivation serves to reduce the parasitic capacitance of the electrical contacts.

3. Device characteristics:

Current is supplied using a microwave probe and light is launched in a butt-coupled 50 μm core diameter MMF or 5 μm core diameter SMF. Fig. 1 summarizes the CW output characteristics of the laser diode with 3 μm active diameter. Threshold current and voltage are 1.3 mA and 2 V, respectively. Laser emission at 3 mA driving current and about 275 μW output power is centered at 846 nm as displayed in the inset in Fig. 1. The side-mode suppression ratio is 30 dB even under modulation.

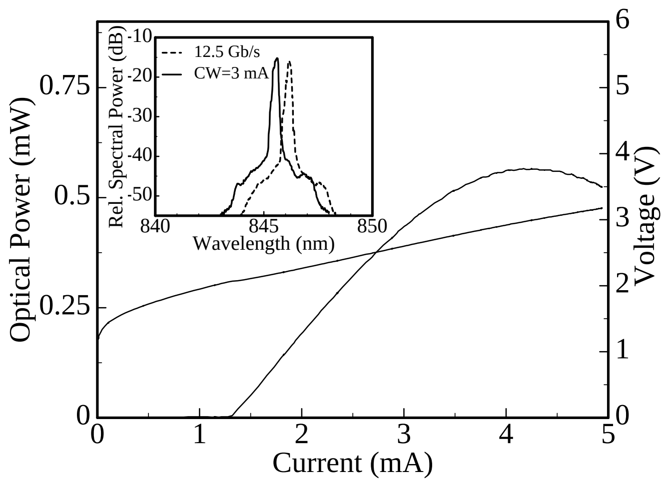

Fig. 1. Output characteristics and spectra at CW and modulated operation with $V_{pp} = 1$ V at 3 mA bias of the 3 μm active diameter, laterally oxidized GaAs VCSEL.

To measure the modulation characteristics free from external parasitics the laser diode is contacted with a microwave probe. The modulated light is detected with a 15 GHz bandwidth InGaAs pin photodiode and recorded with an RF spectrum analyzer. Fig. 2 depicts typical small-signal amplitude characteristics. The modulation bandwidth increases with increasing driving current. The maximum electrical and optical bandwidth obtained at a current of 3 mA is 12.3 GHz and 13.3 GHz, respectively.

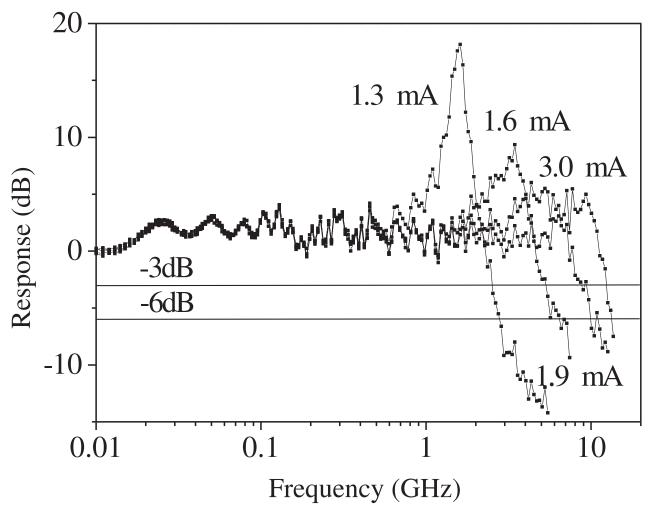

Fig. 2. Small-signal frequency response of 3 μm active diameter VCSEL for various bias currents.

4. Fiber data transmission:

Fig. 3 summarizes the transmission experiments performed at 3 mA bias current and 12.5 Gbit/s PRBS transmission over 100 m of MMF with a wordlength of $2^7 - 1$ and $V_{pp} = 1$ V modulation voltage. Circles denote back-to-back (BTB) testing, triangles represent 1 km 5 μm core diameter SMF transmission, and squares depict 100 m 50 μm core diameter MMF transmission. In all cases the BERs remain better than 10^{-11}. The received optical power for a BER of 10^{-11} is -12.5 dBm and the power penalties for 1 km SMF and 100 m MMF transmission are 1.2 and 7 dB, respectively. The relatively high optical powers necessary for BERs of 10^{-11} are primarily due to the low sensitivity of the InGaAs photodetector used. The eye diagram in the inset of Fig. 3 is recorded at a BER of 10^{-11}. The eye opening is about 400 mV

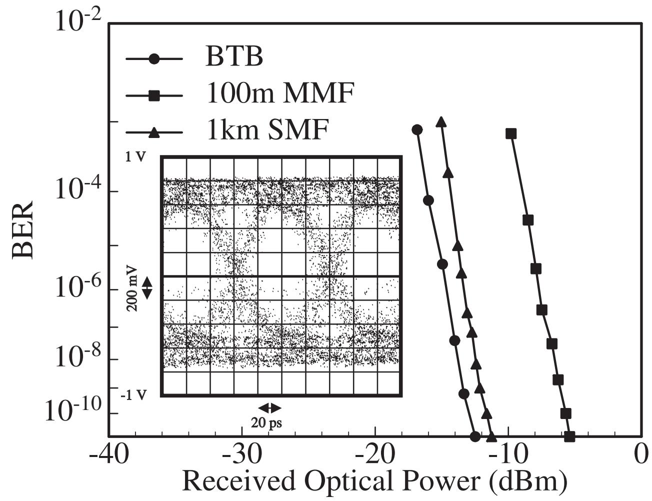

Fig. 3. BER characteristics for $2^7 - 1$ word length PRBS data fiber transmission over 100 m MMF and 1 km SMF. For comparison, results for back-to-back (BTB) testing are also given. The inset shows the eye diagram recorded for BER = 10^{-11} after 100 m transmission.

with a slightly asymmetric shape but without any significant relaxation oscillations. The relatively broad rising traces of about 40 ps width are due to the pattern dependent turn-on jitter.

5. Conclusion:

In summary, we have for the first time demonstrated 12.5 Gbit/s data fiber transmission using selectively oxidized GaAs VCSELs. The BER remains better than 10^{-11} for 100 m MMF as well as for 1 km SMF transmission. 12.5 Gbit/s is the limit of the bit-error test set used. Due to dispersion the transmission distance for MMF is limited to about 100 m which is in accordance with the graded-index fiber bandwidth-length product of 1.25 Gbit/s·km at $\lambda = 850$ nm. Transmission experiments with 5 μm core SMF were restricted by the available fiber length. The obtained results clearly indicate that GaAs VCSELs are attractive transmitters for high speed fiber optic interconnects.

6. Acknowledgement:

This work was supported by the German Science Foundation (DFG). Thanks are due to Anritsu Inc. for providing the bit-error analyzer.

References

[1] D.G. Deppe, D.L. Huffaker, T. Oh, H. Deng, Q. Deng, "Low-threshold vertical-cavity surface-emitting lasers based on oxide-confined and high contrast distributed Bragg reflectors", *IEEE J. Sel. Topics Quantum Electron.*, vol. 3, pp. 893–904, 1997.

[2] Y. Hayashi, T. Mukaihara, N. Hatori, N. Ohnoki, A. Matsutani, F. Koyama, and K. Iga, "Lasing characteristics of low-threshold oxide confinement InGaAs-GaAlAs vertical-cavity surface-emitting lasers", *IEEE Photon. Technol. Lett.*, vol. 7, pp. 1324-1326, 1995.

[3] R. Jäger, M. Grabherr, C. Jung, R. Michalzik, G. Reiner, B. Weigl, and K.J. Ebeling, "57 % wallplug efficiency oxide-confined 850 nm wavelength VCSELs", *Electron. Lett.*, vol. 33, pp. 330–331, 1997.

[4] K.L. Lear, V.M. Hietala, H.Q. Hou, M. Ochiai, J.J. Banas, B.E. Hammons, J.C. Zolper, and S.P. Kilcoyne, "Small and large signal modulation of 850 nm oxide-confined vertical cavity surface emitting lasers", *OSA Trends in Optics and Photonics*, vol. 15, pp. 69–74, 1997.

[5] U. Fiedler, G. Reiner, P. Schnitzer, and K.J. Ebeling, "Top-surface emitting laser diodes for 10 Gb/s data transmission", *IEEE Photon. Technol. Lett.*, vol. 8, pp. 746–748, 1996.

[6] N. Hatori, A. Mizutani, N. Nishiyama, A. Matsutani, T. Sakaguchi, F. Motomura, F. Koyama, and K. Iga, "An over 10-Gb/s transmission experiment using a p-type delta-doped InGaAs-GaAs quantum-well vertical-cavity surface-emitting laser", *IEEE Photon. Technol. Lett.*, vol. 10, pp. 194–196, 1998.

[7] http://www.gigabit-ethernet.org/technology/whitepapers/gige_97/technology.html

Gas Source MBE Growth of 1.3 μm-InAsP/InGaAsP MQWs GRINSCH Laser showing Low Threshold Current Density and High Output Power

Hin Yiu Chung, Georgi Stareev, Jürgen Joos, Jürgen Mähnß

We report the successful fabrication of the first Gas Source MBE grown InAsP/InGaAsP multiple-quantum well lasers with compositional linearly graded InGaAsP confinement layers. The optical quality of the InAsP/InGaAsP quantum wells are investigated by room temperature photoluminescence (PL) spectroscopy; Intense PL-signal with small FWHM is observed in structures containing three quantum wells indicating that our structures are of high optical quality. Nonlinear temperature-ramps are developed and applied to the gallium effusion cell in order to grow lattice-match compositional linearly graded InGaAsP confinement layers. X-ray rocking curves show that the lattice-mismatches of the graded InGaAsP layers are well below 1×10^{-3}. These results indicate that the control of material supply during growth of the InGaAsP layers is highly precise. Laser structures containing graded confinement layers and three quantum wells are grown and fabricated into broad-area laser diodes. Threshold current density of 160A/cm^2 was obtained for 1.5 mm long lasers. This value is among the lowest ever achieved for 1.3μm lasers grown by any kind of MBE process.

1. Introduction

Low threshold current density lasers operating at 1.3 μm wavelength are of particular importance for optical data links and optical telecommunications. To meet this need, laser diodes containing active zones with large carrier and optical confinements are of great interest. In this work, we use strained InAsP/InGaAsP MQWs instead of conventional lattice-matched InGaAsP MQWs as the active zone. The benefits of using InAsP/InGaAsP MQWs include a larger conduction band offset, $\Delta E_c/\Delta E_g = 0.5$ [1] and the incorporation of compressive strain in the QWs. The larger conduction band offset tightly confine carriers in the QWs, where the compressive strain in the QWs helps to reduce the Auger recombination and inter-valence band absorption [2]. Since the strain in the InAsP QWs is usually quite high, it is desirable to use a small number of QWs in the active zone. Therefore, we have decided to investigate the behaviour of the lasers containing three QWs. Tensily strained barriers are used in the MQWs for compensating the compressive strain in the wells. However, no attempt is made to achieve zero-net-strain condition. Compositional linearly graded index separate confinement heterostructure (GRINSCH) made up of InGaAsP provides an effective optical confinement in the active region and hence helps to further reduce the threshold current density of the laser. By combining these two techniques, a drastic reduction of threshold current density can be expected. Up to now, nearly all the laser diodes containing InGaAsP GRINSCH are grown exclusively by MOVPE [3]. It is mainly due to the fact that in MOVPE process, the material compositions seem to be easier to control by the precise mass flow controller. In this work, we use Gas Source (GSMBE) to grow 1.3μm InAsP/InGaAsP lasers with InGaAsP GRINSCH. Precise nonlinear temperature ramps are developed for the gallium effusion cell and linear ramps are used for the AsH_3 gas supply in order to achieve the highly demanding GRINSCH region.

2. Epitaxy and Characterization

The growth of epitaxial layers was carried out in a Riber 32 GSMBE system using elemental In and Ga as the group-III source materials. Pure AsH_3 and PH_3, precracked at 900^0C, were used as the group-V precursors. Be and Si were used as the p-type and n-type dopants respectively. All layers were grown on (100) InP substrates, 2^0 off towards the nearest $(1\bar{1}0)$ direction. The substrate temperature during growth was 480 ^{0}C for all layers and was measured by an Accufiber pyrometer.

One of the main concern of using GSMBE for the growth of GRINSCH lasers is its capability of growing high quality quaternary InGaAsP layers with graded compositions on InP without crystal relaxation. In order to grow lattice-matched graded InGaAsP layers, the material supplies of In, Ga, As and P have to be precisely controlled during growth . For As and P supplies, the AsH_3 and PH_3 precursors can be controlled with a relatively high precision by using Pressure-Control loops. In our control system an accuracy of better than 0.12% in the process gas supply can be achieved even during ramping of the setpoint of the gases.

For the Ga supply, the situation is far more complicated. Since this group-III source material is in form of melt and is evaporated from the effusion cell, achieving a continuously and linearly graded material flux means that a ramping of the effusion cell temperature will be necessary. Although ramping the effusion cell temperature with high precision (better than 0.1% in temperature) is no longer a difficult task, the material flux coming out from the effusion cell does not always follow the profile of the temperature ramp of the effusion cell. It is mainly due to the fact that the temperature response of the material flux is in general nonlinear. Furthermore, flux transient due to heat loss immediately after opening of the cell shutter makes the flux control at the growth-start of the GRINSCH region non-trivial. In this work we use nonlinear temperature ramps for the Ga effusion cell in order to linearize the material flux. In Fig . 1, two nonlinear temperature ramps with their corresponding responses in material flux are shown.

In Fig. 1(a), the effusion cell temperature is ramped from a lower temperature to a higher one immediately after opening of the shutter. The steep slop at the beginning of the temperature ramp serves to compensate the heat loss during shutter opening. After that, the ramping rate is continuously regulated in order to maintain the flux-linearity. With this nonlinear ramp (Ramp 1) the linear Ga flux ramp shown in Fig.1(c) is obtained. In Fig. 1(b), the nonlinear temperature ramp (Ramp 2) for achieving a linearly decreasing Ga flux is also shown. Again, an acceptably linear Ga flux variation is achieved.

Two compositional graded InGaAsP layers are needed for the GRINSCH lasers. The first graded InGaAsP layer (lower GRINSCH) starts with InGaAsP (λ=0.98μm), Q(098), and ends up with InGaAsP (λ=1.10μm), Q(110), and in the second graded InGaAsP layer (upper GRINSCH) the compositional grading of the quaternary layer is vice versa. For the growth of the lower GRINSCH, the temperature of the Ga effusion cell is ramped according to Ramp 1 and a linearly ascending ramp is applied to the AsH_3 supply. For the growth of the upper GRINSCH, Ramp 2 is used. The AsH_3 supply, in this case, is varied linearly in a descending manner. In all cases, the In and PH_3 sources are kept constant.

The graded InGaAsP layers are characterized by X-ray diffraction measurements. The rocking curves of the two kinds of graded layers are shown in Fig . 2. We find out that in both cases, the lattice-mismatches are below 1×10^{-3}. These results clearly show that graded InGaAsP layers grown by GSMBE are excellent. Another prerequisite for achieving laser diodes with low threshold current is the ability to grow high quality QWs structures. The QWs structure used in this work consists of 8 nm thick InAsP QWs with a compressive strain of 1.5% and 16 nm thick InGaAsP quantum barriers (QBs) with a tensile strain of 1.1%. Room temperature PL measurement is carried out on a structure containing three QWs. An

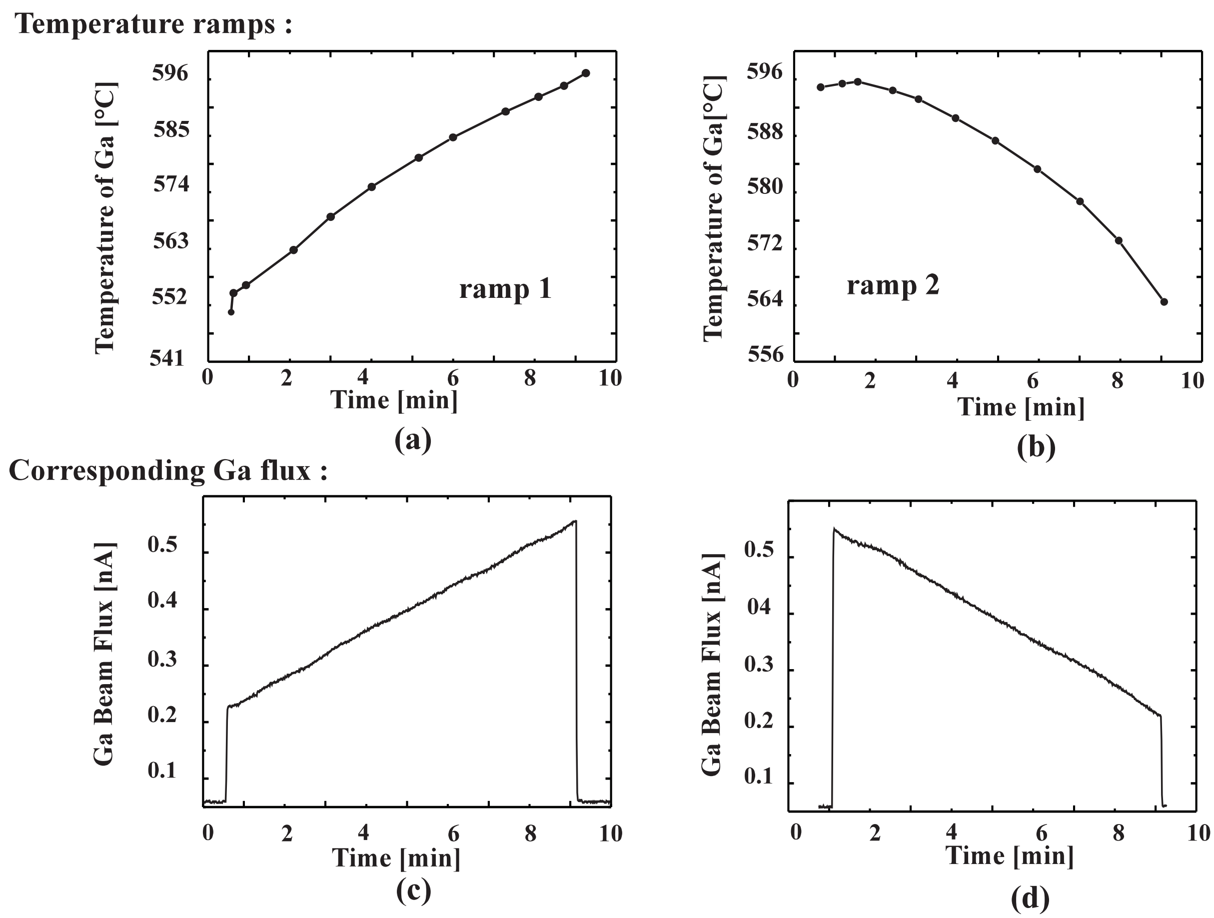

Fig. 1. Nonlinear temperature ramps applied to the Gallium effusion cell for the generation of linearized Gallium material flux. (a) Nonlinear ascending temperature ramp; (b) Nonlinear descending temperature ramp; (c) Linearized Ga flux generated by ramp 1; (d) Linearized Ga flux generated by ramp 2.

intense and sharp PL peak is observed at around 1.295 μm wavelength. The FWHM of the PL peak is 52 meV which indicates that the optical quality of our QWs is high.

3. Laser Structure and Performances

The laser structures contain three QWs surrounded by two 150 nm thick graded InGaAsP layers. The cladding layers are 1.2 μm thick Si-doped InP and 1.2 μm thick Be-doped InP, respectively. A 50 nm thick highly Be-doped InGaAs forms the upper contact layer. After the epitaxy, the laser samples are processed into broad-area ridge-waveguide lasers having 50 μm stripe width and various lengths. The facets of the lasers are as-cleaved and non-coated. No heat-spreader or special mounting technique is used.

The laser diodes are investigated at room temperature under pulse condition. The pulse width is 5 μs and the duty cycle is 0.1%. The lasing wavelength for all devices is around 1.3 μm. In Fig.4, the output power of a 1.5 mm long laser is plotted as a function of the driving current. The threshold current density j_{th} is 160 Acm^{-2} which is among the lowest values achieved for 1.3 μm lasers grown by MBE methods

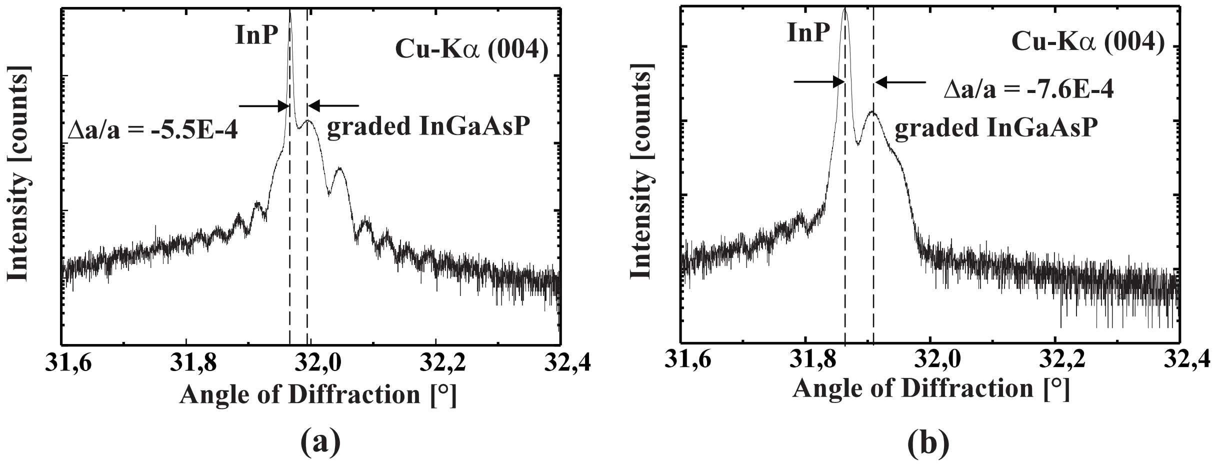

Fig. 2. X-Ray Rocking curves of 150nm compositional linearly graded InGaAsP layers. (a) Material grading from Q(0.98μm) to Q(1.10μm); (b) Material grading from Q(1.10μm) to Q(0.98μ).

[4]. At 10$\times$j$_{th}$, a maximum peak power of up to 307 mW per facet is measured. With these results, a differential quantum efficiency η_d of 58.3% is obtained. Lasers with various lengths are also investigated with respect to their threshold current densities and differential quantum efficiencies. By plotting the threshold current density as a function of the inverse cavity length, we obtain a threshold current density of 130Acm^{-2} for infinitely long cavity. The internal quantum efficiency η_i and the internal loss α_i are 88% and 4 cm^{-1}, respectively. The transparent current density j$_0$ and the modal gain Γg_0 are calculated graphically according to the equation [5]:

$$j_{th} = \frac{N_w j_0}{\eta_i} exp(\frac{\alpha_i + (1/L)\ln(1/R)}{\Gamma g_0} - 1) \tag{1}$$

Here N_w is the number of quantum wells and R the reflectance of the facets. For j$_0$ we obtain a value of 90 Acm^{-2} and for Γg_0 the value is around 30 cm^{-1} . The characteristic temperature of the lasers is also estimated for the temperature range between 10^{0}C and 60^{0}C and has a value of 50K.

4. Conclusion

In conclusion, we have successfully fabricated the first GSMBE grown InAsP/InGaAsP triple QW lasers with compositional linearly graded InGaAsP confinement layers. Nonlinear temperature ramps have been developed for the Ga effusion cell for the growth of the graded InGaAsP layers. X-ray rocking curves show that the lattice-matchings of the graded layers are excellent. 1.5mm long broad area ridge-waveguide lasers exhibit a threshold current density of 160 A/cm^2. At 10$\times$j$_{th}$, a maximum peak output power of up to 307mW per facet is observed. By extrapolation, a threshold current density of 130Acm^{-2} is obtain for infinitely long cavity. The differential quantum efficiency η_d and the internal quantum efficiency η_i are 58.3% and 88%, respectively. The value of internal loss is 4 cm^{-1}. The transparent current density j$_0$ of the laser is found to be 90 Acm^{-2} and the modal gain $\Gamma g_0$is around 30 cm^{-1}. These values are among the best achieved for 1.3 μm lasers grown by MBE techniques.

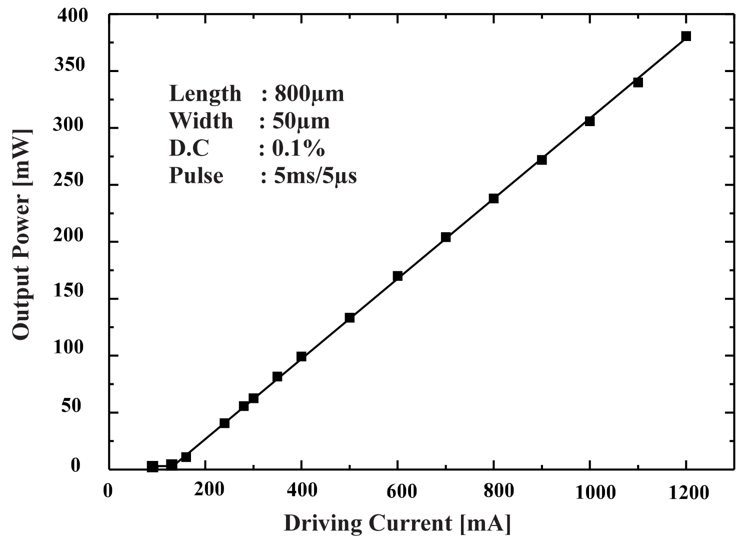

Fig. 3. Output Power vs Current characteristic of a 1.5mm long 3X(InAsP/InGaAsP) QWs laser.

References

[1] H. Sugiura, M. Mitzuhara, H. Oohashi, T. Hirono and K. Nakahima, J. Crystal Growth, vol. 147, pp. 1–7, 1995.

[2] A. Adams, Electron. Lett., vol. 22, pp. 249–250, 1986.

[3] T. Tanbun-Ek, R. A. Logan, N. Olsson, H. Temkin, A. M. Sergent and K. W. Wecht, Appl. Phys. Lett., vol. 57, pp. 224–226, 1990.

[4] H. Uenohara, M. R. Gokhale, J. C. Dries and S. R. Forrest, Electron. Lett., vol. 33, pp. 1263–1264, 1997.

[5] P.W.A. McIlroy, A. Kurobe and Y. Uematzu, IEEE J. of Quantum Electron., vol. QE-21, No. 12, pp. 1958–1963, 1985.

Infrared Light-Emitting Diodes with Lateral Outcoupling Taper

W. Schmid

We present a non-resonant light emitting diode with a novel concept of light outcoupling. Light is generated in the center of a radially symmetric structure and propagates between two mirrors to a tapered region where outcoupling occurs. Different process routes are developed resulting in on-substrate as well as substrateless devices.

1. Introduction

One of the cardinal problems limiting the performance of light emitting diodes (LEDs) is their low efficiency caused by total internal reflection (TIR). Different approaches already exist to overcome this problem. Among those are resonant cavity LEDs with their modified internal direction of spontaneous emission [1], surface textured devices with a back side mirror where photons repeatedly try to escape [2], or the use of transparent substrate [3]. We introduce a new concept of efficient outcoupling for both top and bottom emitting devices. While top emitters have the advantage of remaining on the original substrate, substrateless bottom emitters require no distributed Bragg reflector (DBR) allowing an easy process transfer to other materials and wavelengths. In both devices the light is generated in a central area of a radially symmetric structure and the total internally reflected part of light propagates between a high reflecting mirror and the surface of the semiconductor to a laterally tapered region. Here light is coupled out by successively decreasing the incident angle of the light to the tapered surface until it overcomes the condition of TIR. Because light is redirected in a more systematical rather than random way compared to surface textured devices only a few reflections are required. This relaxes the requirements to be met by the mirror which is realized in the top emitting device as an AlGaAs/GaAs DBR combined with a thick wet oxidized AlAs layer. In the bottom emitter the reflector consists of a Au layer deposited on a passivation layer.

2. LED Structure and Processing of Top-Emitting Devices

Fig. 1 shows a schematic cross-section of a processed LED. The layers are MBE grown on GaAs substrate. The lowermost layer stack consists of an AlGaAs/GaAs DBR with an additional thick ($\approx$ 160 nm) AlAs layer which is completely wet oxidized. A following 1.5 μm thick n-GaAs layer offers lateral optical confinement and is employed to create an n-short to substrate. The $In_{0.15}Ga_{0.85}As$ quantum well based active region includes a 30 nm thick $Al_{0.97}Ga_{0.03}As$ layer to be partially oxidized to concentrate light generation to the center of the device. A several hundred nm thick GaAs layer serves as p-region and contributes to lateral optical guiding.

The processing is as follows. After MBE growth a few hundred nm thick pedestal with the outer diameter of the later device is wet etched. A photo resist is deposited and circularly structured with a slightly smaller size. In a reactor with a well defined temperature and organic solvent concentration the photo resist reflows to the edge of the pedestal and assumes a lensed shape due to surface tension [4]. Using

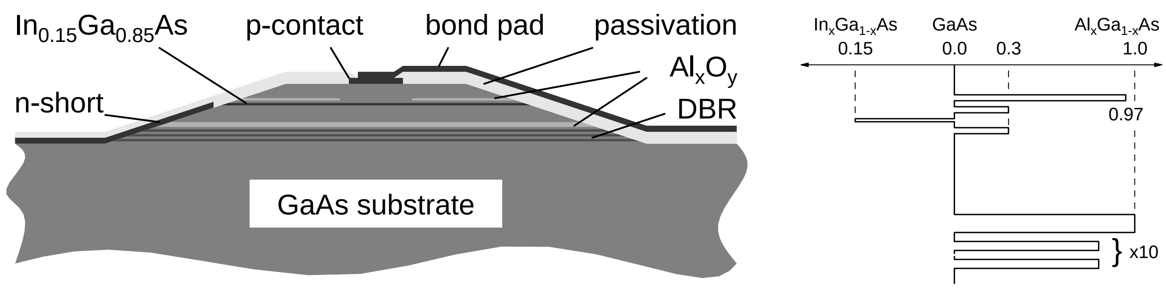

Fig. 1. Schematic cross-section of an top-emitting LED. The right hand part indicates layer composition.

ion beam etching with low selectivity the structure is partially transferred into the semiconductor. After removing the photo resist both AlGaAs layers with 97 and 100 % Al contents are simultaneously wet oxidized. A lower oxidation rate of the thin layer is ensured by adding a few percent Ga. This enables a partial oxidation of the current confining layer while the optical guiding layer is completely converted to $\mathrm{Al}_x\mathrm{O}_y$ despite of its larger diameter. To overcome the resulting electrical isolation a metal contact between the tapered n-region and the substrate is required which is realized as quarter ring shaped contact to limit the shaded area. For the p-contact we use a small circular Ti/Pt/Au metallization on the flat top surface. Finally, a bond pad is deposited on a passivation layer.

3. Characteristics of Top-Emitting Devices

The left and right parts of Fig. 2 show CCD images of a fully processed device under external illumination and in LED operation, respectively. The bright emission ring clearly demonstrates an efficient outcoupling in the tapered area. Output and voltage characteristics of a 100 μm device with an active diameter of about 35 μm and a taper angle of 20 $^\circ$ are displayed in Fig. 3. The optical output power is measured with an integrating sphere. For calibration an average emission wavelength of 930 nm is estimated from the measured spectrum taken at a current of 4 mA as shown in the inset of Fig. 3. The LED is driven up to 4 mA where the output power reaches 460 μW. A maximum quantum efficiency $\eta_q = 12$ % is obtained in the current range between 0.6 and 0.8 mA corresponding to a current density of about 70 A/cm^2. Conversion efficiency η is up to 10 %.

4. Substrateless LED Structure and Processing

Since an effective DBR cannot be easily manufactured in all material systems we have also investigated an alternative processing route which results in a substrateless bottom-emitting device as shown in Fig. 4.

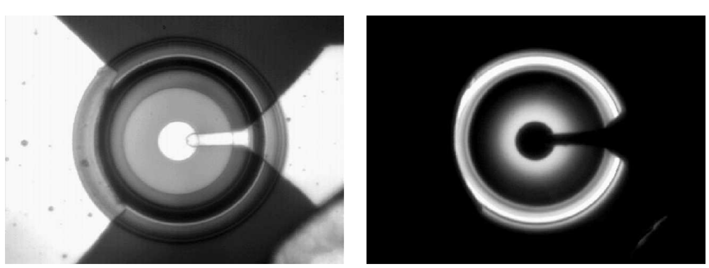

Fig. 2. CCD images of a device of 100 μm diameter. In the top view of the left hand side we can see the quarter ring n-contact and the circular p-contact deposited on the top and connected to a bond pad. The right hand side picture shows the near field emission pattern of the device at a current of 1 mA.

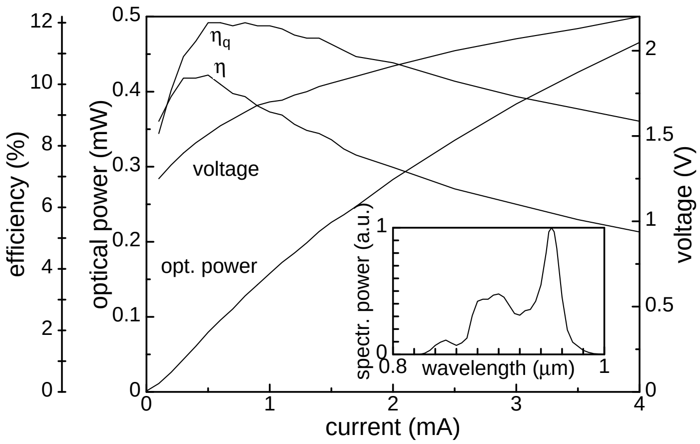

Fig. 3. Power and voltage characteristics of a 100 μm device with an active diameter of about 35 μm and a taper angle of 20 °. Also shown are quantum and conversion efficiencies and the optical spectrum at 4 mA.

The lowermost layer used as an etch stop consists of 200 nm thick AlAs. Active region as well as n- and p-type layers are similar to those in the top-emitting devices. Also, the first processing steps are the same except that no oxidation step is applied. Light generation is restricted to the central region by the relatively high resistance in the p-type material and the small diameter p-contact. The p-bond pad of the top-emitting devices is provided by a homogeneous Au layer which simultaneously serves as a reflector. For substrate removal additional processing steps are required. The Au layer thickness is galvanically increased to about 1 μm. After gluing the wafer upside down on a glass carrier, the substrate is chemo-mechanically thinned down to 50 μm. Finally the substrate is selectively etched with an H_2O_2:NH_4OH solution where the pH is adjusted to 8.1 [5]. In this way the quarter ring n-contact appears at the surface and can be used for independent addressing current supply.

5. Characteristics of Substrateless Devices

Voltage and output characteristics of a device with a 95 μm outer diameter are shown in Fig. 5. An optical power of 1 mW is obtained at a current of 7 mA. Quantum efficiency η_q as well as conversion efficiency η are about 15 % at currents in the 1.5 to 2.5 mA range. The decrease of efficiency at higher currents can be related to heating and current spreading effects. The applied voltage corresponds to the bandgap energy. The series resistance of about 25 to 30 Ω is mainly due to the small area of the n-contact and the high p-layer resistance required for current confinement. Optical characteristics of smaller devices with the same p-contact area are additionally plotted in the diagram and show inferior characteristics. This clearly indicates that we have not yet achieved an optimum device design where gain due to improved outcoupling is in the same range as losses due to absorption.

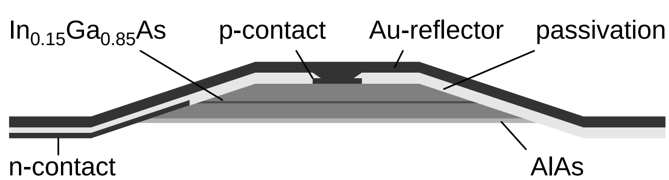

Fig. 4. Schematic cross-section of a substrateless LED with a lateral taper.

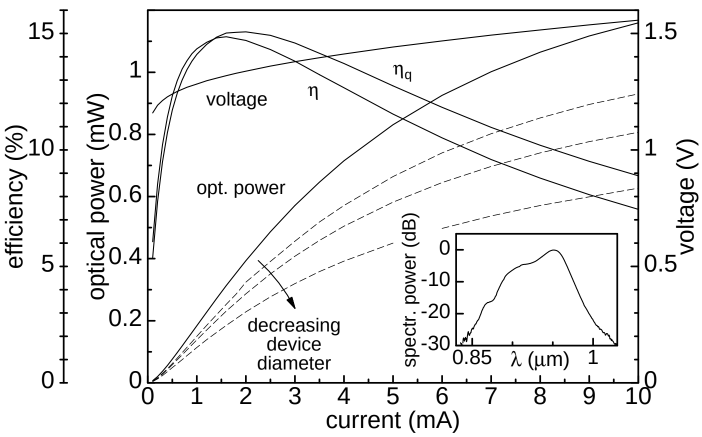

Fig. 5. Voltage and output characteristics of a 95 μm device. For calibration we have used the sensitivity at the 950 nm peak in the inset spectrum.

6. Conclusion

We have presented a new concept for efficient light outcoupling from LEDs applying a radial taper combined with spot-like central light generation. For material systems with efficient DBRs we have developed a processing route resulting in efficient devices without the requirement of epitaxial lift-off. First test structures show a quantum-efficiency of 12 %. Using substrate removal devices with efficiencies of about 15 % have been fabricated which can ease be transferred to material systems where effective DBRs cannot be realized. The results clearly show that LEDs with lateral taper can be extremely attractive for achieving high light outcoupling efficiencies.

References

[1] E.F. Schubert, N.E.J. Hunt, M. Micovic, R.J. Malik, D.L. Sivco, A.Y. Cho, and G.J. Zydzik, "Highly efficient light-emitting diodes with microcavities," *Science* **265**, pp. 943–945, 1994.

[2] I. Schnitzer, C. Caneau, T.J. Gmitter, A. Scherer, and E. Yablonovitch, "30 % external quantum efficiency from surface textured, thin-film light-emitting diodes," *Appl. Phys. Lett.* **63**, pp. 2174–2176, 1993.

[3] D.A. Vanderwater, I.-H. Tan, G.E. Höfler, D.C. Defevere, and F.A. Kish, "High-brightness AlGaInP light emitting diodes," *Proc. IEEE* **85**, pp. 1752–1763, 1997.

[4] L. Erdmann and D. Efferenn, "Technique for monolithic fabrication of silicon microlenses with selectable rim angles," *Opt. Eng.* **36**, pp. 1094–1098, 1997.

[5] J. LePore, "An improved technique for selective etching of GaAs and $Ga_{1-x}Al_xAs$," *J. Appl. Phys.* **51**, pp. 6441–6442, 1980.

High Power 3×3 VCSEL Array

Michael Miller, Martin Grabherr

We have fabricated high power and highly efficient bottom-emitting 3 × 3 VCSEL arrays with an optical output power of 650 mW under cw operation at room temperature. The maximum spatially averaged power density is 370 W/cm^2 for the total chip size of 420×420 μm^2 for the cleaved array. This requires an improved mounting technique for efficient heat sinking of the devices.

1. Introduction:

Vertical cavity surface emitting lasers (VCSELs) have become superior devices for various applications in data transmission, especially parallel optical interconnects. Their output power is limited to a few mW due to the small active diameter of about 10 μm and thermal rollover. To obtain higher optical power one can increase active size of a single laser at the cost of decreasing wallplug efficiencies [1] or switch to two-dimensional arrays which provide high output powers at still high conversion efficiencies [2]. For both conceptions improved heat sinking of the devices is indispensable.

2. Devices:

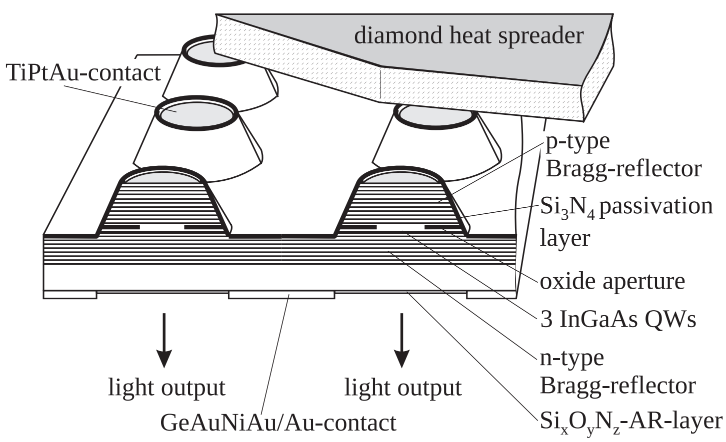

Fig. 1. Schematic drawing of a two-dimensional bottom emitting VCSEL array soldered on diamond heat spreader.

We have designed and fabricated efficient VCSEL arrays consisting of 3 × 3 bottom-emitting devices for a wavelength of 980 nm. The structure shown in Fig. 1 is grown by solid source MBE and consists of 30 p- and 24 n-type Bragg-reflectors surrounding the inner cavity with three 8 nm thick InGaAs quantum wells. 70 μm diameter mesas are wet chemically etched down to the depth of the inner cavity and current apertures of 50 μm in diameter are formed by wet oxidation of a 30 nm thick AlAs-layer just above the p-type cladding layer. The center to center spacing between neighboring elements is 140 μm. Evaporation of the p-type contact is followed by deposition of a passivation layer on the epitaxial side. After thinning of the substrate to a thickness of around 180 μm an anti-reflection coating is sputtered. To structurize the emission-windows a dry etching step with CAIBE is done. The n-type contact is then evaporated and structured by lift-off technique and a 1 μm thick Au-layer is deposited galvanically for bonding. Finally, the cleaved arrays are soldered junction side down on diamond heat spreaders and heatsunk on copper submounts. The characteristics of good soldering are mechanical stability and good thermal and electrical contacts. Therefore an eutectic AuSn-alloy consisting of 80% Au and 20% Sn is used as a hard solder. The array is mounted using a Die Bonder. The thickness of the solder is 5 μm which is quite large. Various tests have shown that it can be reduced below 2 μm. There are many

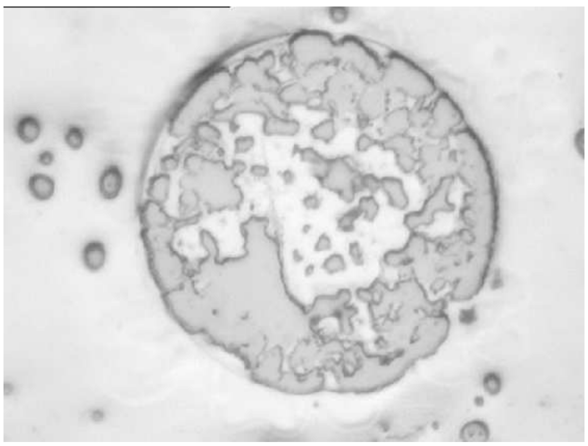

Fig. 2. Impression of a mesa from an array soldered on a heat sink and removed afterwards.

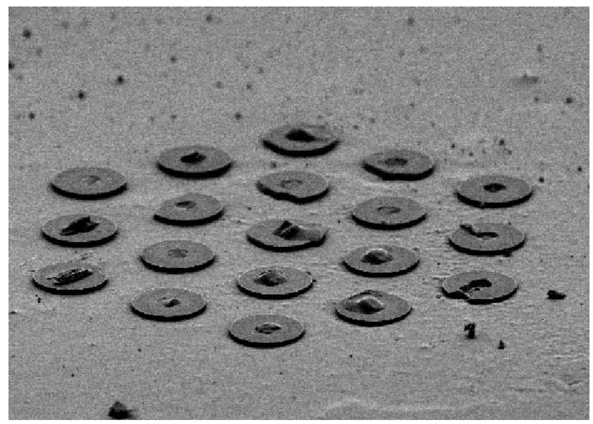

Fig. 3. Torn off mesas at oxide aperture after removing the soldered array from the heat sink.

influences during the soldering process like pressure, atmosphere, temperature and time. Fig. 2 shows the surface of a metallized diamond with solder on it after an array was soldered and removed again. The maximum temperature and the soldering time were not well adjusted so in the impressions from the mesas a lot of airholes can be seen which causes insufficient thermal contact and bad mechanical stability. In spite of these bad conditions an increase in the optical output power can be seen but there is still place for improvements. After several tests it was possible to achieve a good soldering which can be seen in Fig. 3. Again an array was soldered and removed afterwards but now the soldering interface is intact. The mesas were torn off where the current aperture was oxidized and one can see the broken crystal structure.

3. Measurements:

The output characteristics of the individual elements from the 3×3 array are given in Fig. 4. The threshold current is about 17 mA which gives a threshold current density of about 870 A/cm^2. The maximum output power range is between 55 and 65 mW and the maximum conversion efficiency is between 32 and 36% at 3 times threshold. The differential resistance is 8.9 Ω. Due to the common p-contact after mounting the array on the diamond heat spreader all the elements have to be driven parallel. Therefore a good homogeneity of the elements in the array is necessary which can also be

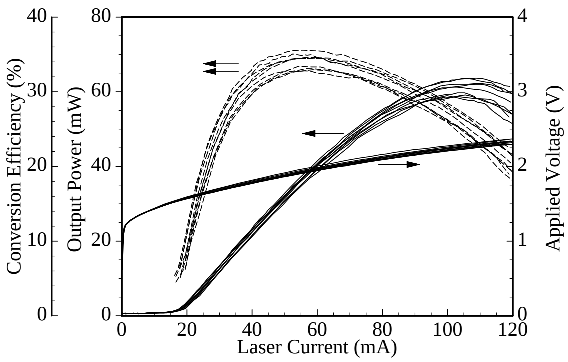

Fig. 4. CW output characteristics of the 9 individual elements with 50 μm active diameter.

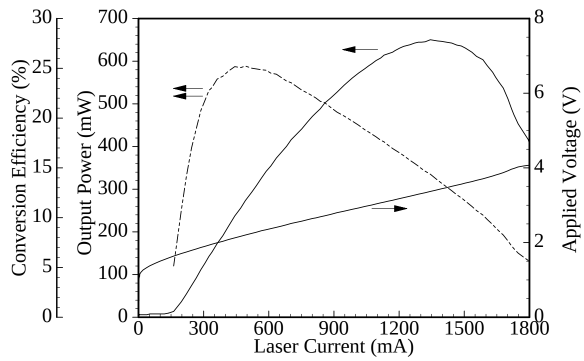

Fig. 5. CW output characteristics of a mounted 3×3 array.

seen in Fig. 4. This results in an overall output power of 650 mW at about 9 times threshold and 15% conversion efficiency under cw operation. The LIV curves in Fig. 5 show a threshold current of 153 mA corresponding to 9 times the threshold of an unmounted individual device. Threshold voltage and differential resistance are 1.8 V and 1.4 Ω, respectively. The slight increase of the differential resistance for the parallel driven devices is due to the not perfect soldering on the diamond. Maximum conversion efficiency reaches 25% at 3.2 times threshold at an output power of 270 mW. The maximum spatially averaged power density is 370 W/cm^2 for the total chip size of 420×420 μm^2 for the cleaved array.

4. Outlook:

Further investigations will be done for larger arrays with more elements and a higher density. Therefore the soldering technique has to be investigated in detail. Very important for densely packed VCSEL arrays is the thermal cross talk between the elements. To get more information about this, independently addressable elements in an array are requested. This can be done by using structured heat sinks.

References

[1] M. Grabherr, R. Jäger, M. Miller, C. Thalmaier, J. Heerlein, R. Michalzik, and K. J. Ebeling, “Bottom-emitting VCSELs for high cw optical output power”, *IEEE Photon. Techn. Lett.*, vol. 10, pp. 1061–1063, 1998.

[2] M. Grabherr, M. Miller, R. Jäger, and K. J. Ebeling, “Efficient bottom emitting VCSEL arrays for high cw optical output power”, *Electron. Lett.*, vol. 34, pp. 1227–1228, 1998.

Biased and Bias-Free Multi-Gb/s Data Links Using GaAs VCSEL's and 1300 nm SM Fiber

Peter Schnitzer and Felix Mederer

Selectively oxidized single-mode GaAs vertical-cavity surface-emitting lasers (VCSEL's) are investigated for biased 3 Gb/s and bias-free 1 Gb/s data links. Bit error rates (BER's) of better than 10^{-11} *for pseudo-random data transmission over 4.3 km of standard 1300 nm single-mode fiber are demonstrated. A simple mode filter is used to suppress intermodal dispersion. The requirements of the Gigabit Ethernet are fulfilled even for bias-free operation.*

1. Introduction

Optical data links are very promising in terms of their capacity to increase the speed of digital networks such as local area networks (LAN's) and wide area networks (WAN's). For continuously decreasing transmission distances high-bit-rate optical fiber links even outperform their copper-based competitors with regard to cost per available bandwidth. Due to their outstanding properties, selectively oxidized VCSEL's have become prospective candidates for transmitters in high-bit-rate fiber links. Threshold currents in the 50 μA regime [1], threshold voltages close to the bandgap voltage in combination with high wall-plug efficiencies [2], polarization control, and modulation bandwidths of 21.5 GHz [3] all show the enormous potential of these laser diodes. Multimode fiber (MMF) links of 500 m length at data rates of up to 10 Gb/s biased [4] and 2.5 Gb/s bias-free [5] have already been demonstrated. All these features in combination with geometrical advantages allowing easy formation of one- and two-dimensional arrays make VCSEL's highly attractive for various kinds of optical data links such as fiber-based [6] and free-space [7] parallel optical interconnects. Aside from few-100-m distance MMF data links, it is highly desirable to employ VCSEL's in standard 1300 nm single-mode fiber (SMF) lines in order to profit from inexpensive devices for high-bit-rate networks such as the Gigabit Ethernet which is designed for data rates of 1 Gb/s and fiber lengths of up to 550 m of 50 μm diameter MMF and $\geq$ 3 km SMF [8].
In this work, we report on laterally oxidized GaAs VCSEL's for biased 3 Gb/s and bias-free 1 Gb/s non-return-to-zero (NRZ) pseudo random bit sequence (PRBS) transmission with $2^{31} - 1$ wordlength. The BER remains below 10^{-11} after transmission over 4.3 km of 1300 nm SMF and mode filtering.

2. Device structure

The laser structure under investigation was grown by solid-source molecular beam epitaxy. The bottom distributed Bragg reflector (DBR) consists of 30.5 n-type Silicon doped AlAs/ $Al_{0.2}Ga_{0.8}As$ layer pairs. The one-wavelength thick central region contains three 8 nm thick GaAs quantum wells embedded in $Al_{0.5}Ga_{0.5}As$ spacer layers to provide efficient carrier confinement. The p-type top DBR consists of 26 Carbon doped $Al_{0.2}Ga_{0.8}As/Al_{0.9}Ga_{0.1}As$ layer pairs. An extra 30 nm AlAs layer inserted in the lowest top mirror pair is selectively oxidized for current confinement after wet chemical mesa etching. In order to obtain single-mode operation the oxidation layer is shifted towards the node of the standing wave pattern yielding weak index guiding [9]. After oxidation a p-Ti/Pt/Au top ring contact is deposited on top of the mesa to achieve good ohmic contacts as well as light emission through the top DBR. Ti/Au conducting tracks and bondpads are deposited on a polyimide insulation layer. Polyimide provides a smooth planar surface, good passivation, and improves high frequency behavior due to the small permittivity. Mechanically polishing the GaAs substrate down to 150 μm and evaporating a Ge/Ni/Au broad area contact are final process steps.

3. Experiment

Fig. 1 summarizes the output characteristics of the 4 μm active diameter VCSEL source employed in the transmission experiments.

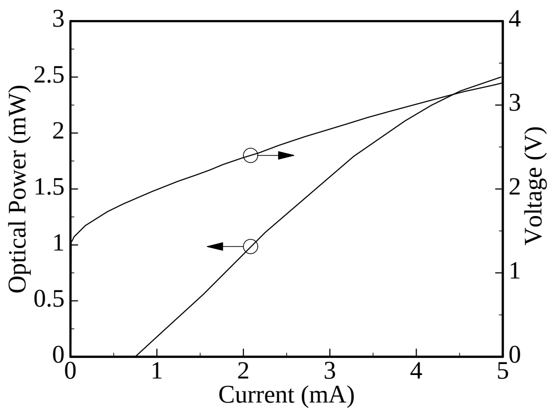

Fig. 1. Output characteristics of laterally oxidized single-mode GaAs VCSEL.

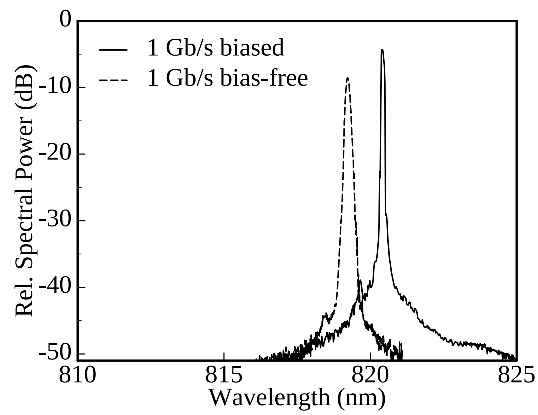

Fig. 2. Optical spectra of single-mode VCSEL with -10 dB widths of 0.15 and 0.3 nm for 2.6 mA biased $V_{pp} = 1.5$ V and bias-free $V_{pp} = 2$ V modulation, respectively.

Threshold current is as low as 750 μA and threshold voltage is 1.8 V. The laser diode shows single-mode operation up to a driving current of 5 mA. For the transmission experiments, the laser is either directly driven by a pattern generator at 1 Gb/s with $V_{pp} = 2$ V without any additional bias, or by a bias current of 2.6 mA and 1 or 3 Gb/s PRBS with $V_{pp} = 1.5$ V which are combined in a bias-tee and fed to the VCSEL source. The laser is wire bonded to an SMA socket to keep feeding lines as short as possible. Output power is launched in a butt-coupled SMF with 8.3 μm core diameter and 4.3 km length. Although butt-coupling effectively changes the output mirror reflectivity, no time-dependent feedback effects are introduced. The transmitted signal is passed through a variable attenuator and detected with a Germanium avalanche photodiode. The preamplified bit sequence is monitored with an electrical sampling oscilloscope and analyzed with a BER detector. The spectra given in Fig. 2 are centered at 819 nm and 820 nm for bias-free $V_{pp} = 2$ V operation and 2.6 mA bias current and $V_{pp} = 1.5$ V modulation, respectively. In both cases the side-mode suppression is larger than 35 dB and the -10 dB spectral width is 0.15 nm for biased and 0.3 nm for bias-free operation. Mode filtering is realized by macro bending of the fiber [10]. For a fiber subjected to small radius bends, the number of modes decreases due to the power leakage caused by radiation of higher order modes [11]. The used 8.3 μm core diameter SMF is a two-mode fiber at $\lambda = 820$ nm since we obtain

$$V = \frac{2\pi}{\lambda} a\mathrm{NA} = 3.5 \tag{1}$$

for the normalized frequency parameter [12], where $a = 4.15$ μm is the core radius and NA $= 0.11$ is the numerical aperture. Step index fibers are single-mode up to $V = 2.405$ and are two-mode up to $V = 3.83$ [12]. Therefore, we observe both the LP_{01} and LP_{11} mode after 4.3 km propagation in the fiber as shown in Fig. 3 b). Simple mode filtering selects the favored LP_{01} mode displayed in Fig. 4 b).

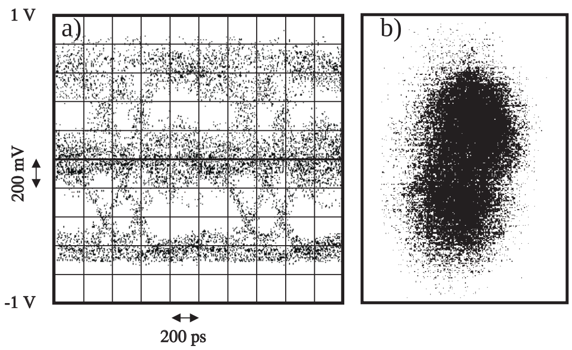

Fig. 3. Eye diagram a) and far field pattern b) of superposed LP_{01} and LP_{11} modes at 1 Gb/s PRBS with $2^{31} - 1$ wordlength recorded after 4.3 km SMF transmission without mode filter.

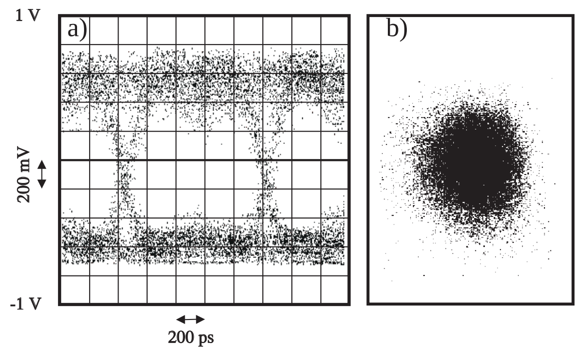

Fig. 4. Eye diagram a) and far field pattern b) of LP_{01} mode at 1 Gb/s PRBS with $2^{31} - 1$ wordlength recorded after 4.3 km SMF transmission with mode filter.

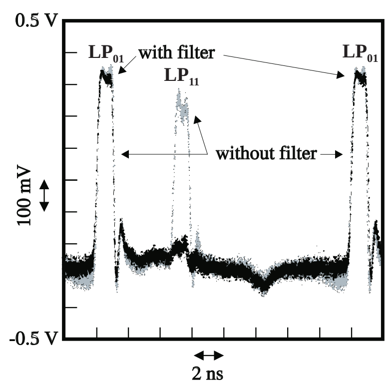

Fig. 5. Signal of LP_{01} mode (solid line) and LP_{11} mode (dashed line) after 4.3 km SMF transmission.

A fiber loop with a diameter of 17 mm and 5 windings is used for mode filtering. This diameter has been chosen to obtain sufficient losses of the LP_{11} mode. The fiber mode filter can be applied either at the fiber input or at the fiber output since no transfer of energy between the two modes is observed. Mode coupling cannot be excluded in general but depends on the micro bending spectrum of the actual fiber. The disadvantage of the coexistence of the LP_{01} and he LP_{11} modes is illustrated in the blurred eye diagram in Fig. 3 a) and the time delayed secondary pulse plotted as dashed line in Fig. 5, where the signal of a logical "one" followed by 15 logical "zeros" at 1 Gb/s after 4.3 km SMF transmission is recorded. The solid line is the information carried by the LP_{01} mode while the dashed line represents the information carried by the LP_{11} mode. Mode filtering removes the dashed line in Fig. 5 and leads to the eye diagram shown in Fig. 4 a). This eye diagram is wide-open and shows neither double lines nor any remarkable relaxation oscillations. Fig. 6 summarizes the results of the BER measurements. Solid and open circles denote 1 Gb/s biased back-to-back (BTB) testing and 4.3 km SMF transmission, solid and open squares denote 1 Gb/s bias-free back-to-back testing and 4.3 km SMF transmission, and solid and open triangles represent 3 Gb/s back-to-back testing and 4.3 km SMF transmission, respectively. The received optical powers for biased and bias-free back-to-back testing for a BER of 10^{-11} are -25.8 dBm and -24.5 dBm while the corresponding power penalties for 4.3 km SMF transmission are 2.8 dB and 2.5 dB, respectively. The on-off ratio for biased operation is about 17 dB. For biased 3 Gb/s modulation the received optical power for back-to-back testing is -22 dBm and the power penalty for 4.3 km SMF transmission is 2.1 dB.

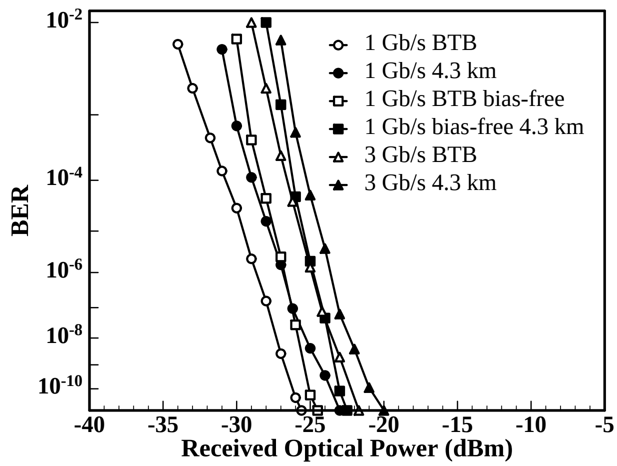

Fig. 6. Bit error rates with $2^{31}-1$ wordlength for various combinations of bit rate and modulation scheme, each for back-to-back (BTB) and 4.3 km SMF transmission.

4. Summary & Conclusion

In summary, we have demonstrated 3 Gb/s biased and 1 Gb/s bias-free $2^{31}-1$ PRBS signal data transmission with 820 nm single-mode VCSEL over an inherently two-moded standard SMF line of 4.3 km length. A BER of better than 10^{-11} has been achieved and the power penalty for 4.3 km transmission is about 2.1 dB for 3 Gb/s biased and 2.5 dB for 1 Gb/s bias-free modulation. The investigated GaAs VCSEL is able to fulfill the requirements for the Gigabit Ethernet using existing 1300 nm SMF even for bias-free operation. The single-mode VCSEL produces negligible chromatic and waveguide dispersion over the given distance due to the extremely narrow emission linewidth. However, fiber transmission produces modal dispersion which is suppressed by applying simple mode filtering and thus does not affect BER characteristics. The results show that the single-mode VCSEL's in combination with mode filtering are well suited for high-bit-rate data transmission over several kilometers distance indicating simple ways for upgrading existing fiber links for extended wavelength or bit rate operation.

References

[1] D.G. Deppe, D.L. Huffaker, T. Oh, H. Deng, Q. Deng, "Low-threshold vertical-cavity surface-emitting lasers based on oxide-confined and high contrast distributed Bragg reflectors", *IEEE J. Sel. Topics Quantum Electron.*, vol. 3, pp. 893–904, 1997.

[2] R. Jäger, M. Grabherr, C. Jung, R. Michalzik, G. Reiner, B. Weigl, and K.J. Ebeling, "57 % wallplug efficiency oxide-confined 850 nm wavelength VCSELs", *Electron. Lett.,* vol. 33, pp. 330–331, 1997.

[3] K.L. Lear, V.M. Hietala, H.Q. Hou, M. Ochiai, J.J. Banas, B.E. Hammons, J.C. Zolper, and S.P. Kilcoyne, "Small and large signal modulation of 850 nm oxide-confined vertical cavity surface emitting lasers", *OSA Trends in Optics and Photonics,* vol. 15, pp. 69–74, 1997.

[4] U. Fiedler, G. Reiner, P. Schnitzer, and K.J. Ebeling, "Top-surface emitting laser diodes for 10 Gb/s data transmission", *IEEE Photon. Technol. Lett.,* vol. 8, pp. 746–748, 1996.

[5] P. Schnitzer, M. Grabherr, R. Jäger, C. Jung, and K.J. Ebeling, "Bias-free 2.5 Gbit/s data transmission using polyimide passivated GaAs VCSELs", *Electron. Lett.,* vol. 34, pp. 573–575, 1998.

[6] Y. Sugimoto, H. Kosaka, T. Yoshikawa, H. Saitoh, K. Kurihara, and K. Kasahara, "High-performance 980 nm vertical-cavity surface emitting lasers and their application to two-dimensional array interconnects", *OSA Trends in Optics and Photonics,* vol. 15, pp. 139–149, 1997.

[7] E.M. Strzelecka, D.A. Louderback, B.J. Thibeault, G.B. Thompson, K. Bertilsson, and L.A. Coldren, "Parallel free-space optical interconnects based on arrays of vertical cavity lasers and detectors with monolithic microlenses", *OSA Trends in Optics and Photonics*, vol. 15, pp. 174–185, 1997.

[8] http://www.gigabit-ethernet.org/technology/whitepapers/gige_97/technology.html

[9] M. Grabherr, R. Jäger, R. Michalzik, B. Weigl, G. Reiner, and K.J. Ebeling, "Efficient single-mode oxide-confined VCSEL's emitting in the 850 nm wavelength regime", *IEEE Photon. Technol. Lett.,* vol. 9, pp. 1304–306, 1997.

[10] H.F. Taylor, "Bending effects in optical fibers", *IEEE J. Lightwave Technol.,* vol. LT-2, pp. 617–628, 1984.

[11] D. Marcuse, "Curvature loss formula for optical fibers", *J. Opt. Soc. Am.,* vol. 66, pp. 216–220, 1976.

[12] A.W. Snyder and J.D. Love, *Optical Waveguide Theory*, Chapman and Hall, New York, 1983, pp. 311–326.

Thermal crosstalk in densely packed high power VCSEL arrays

M. Grabherr, M. Miller, H.J. Unold

We present detailed investigations on the thermal interaction between closely spaced vertical-cavity surface-emitting laser diodes (VCSELs). Applying the results to simple modeling of cw output characteristics, thermally induced power limitations of two-dimensional arrays can be described. Experimentally 0.56 and 0.8 W cw output power at room temperature and -10 °C, respectively, are observed for an array of 23 elements with 40 μm active diameter and 90 μm center spacing.

1. Introduction

In the last few years the optimization of VCSELs for optical data transmission led to highly efficient devices, mainly due to reduced series resistances in the Bragg reflectors [1] and improved current confinement by an oxide aperture [2]. VCSELs are limited in optical output power by thermal rollover, therefore efficient devices which benefit from reduced dissipated power show promising prospects for high optical power generation. Upscaling the active area of well established single top- and bottom emitting VCSELs results in 180 mW and 350 mW cw output power for 150 μm and 200 μm active diameter, respectively [3]. However, both approaches suffer from a disadvantegeous decrease of conversion efficiency, which is understood from modeling the cw output characteristics based on fundamental electro-optical parameters. The two dimensional arrangement of individual VCSELs designed for high efficiency operation is an obvious possibility to achieve high output powers at high efficiencies. The overall output power scales sublinear with the number of individual lasers, depending on the thermal interaction between the array elements. Therefore, the thermal crosstalk is an important parameter to describe the output characteristics of densely packed two-dimensional arrays that provide high output powers at high conversion efficiencies as well as high spatially averaged power densities.

2. Thermal crosstalk in bottom-emitting arrays

For the investigated arrays bottom-emitting devices are preferred because of the better beam quality and the possibility of junction-down mounting for better heat removal [4]. The device structure and the processing are described elsewhere [5]. In order to understand the thermal effects in monolithic arrays we have measured the temperature increase ΔT_A of a VCSEL A as a function of dissipated power $\Delta P_{diss,B}$ in a neighboring VCSEL B. The thermal cross-resistance R_{cross} is defined in analogy to the thermal resistance as

$$R_{cross,AB} = \frac{\Delta T_A}{\Delta P_{diss,B}}. \tag{1}$$

To separate the mutual thermal interaction between the two devices, device A is driven under pulsed condition. Thus the time averaged dissipated power can be neglected. In Fig. 1 the thermal cross-resistance of unmounted lasers versus device spacing d is plotted for distances from 70 up to 370 μm. From the fit function, we obtain a thermal cross-resistance which is inversely proportional to the device spacing plus

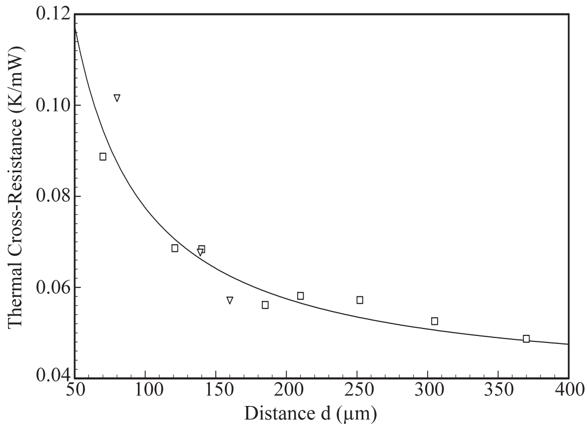

Fig. 1. Thermal cross-resistance R_{cross} versus device spacing.

a certain offset.

In order to study the thermal interaction between parallel driven devices in some detail measurements are performed on a 3$\times$1 VCSEL array mounted on a diamond heat sink. This heat sink provides structured metal pads to allow individual operation of the three devices. Fig. 2 shows an image of this test

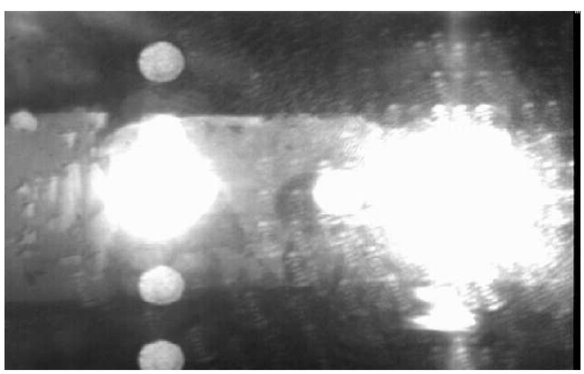

Fig. 2. Image of the separately operated 3x1 array. The left device is driven under pulsed conditions, the center device is off, and the right device runs cw.

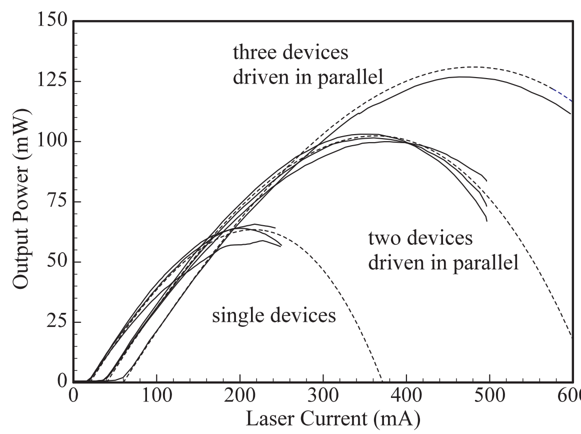

Fig. 3. Measured output characteristics of the individually addressable 3x1 VCSEL array where the devices are driven separately, two in parallel, and all in parallel under cw conditions. Dashed lines correspond to simulations including thermal crosstalk.

structure, where the left device is driven under pulsed conditions, the center device is off, and the right device runs cw. The active diameters are 50 μm and the center spacings between devices are 140 μm. Solid lines in Fig. 3 show the measured LI curves of the three devices driven separately, two in parallel, and all three in parallel, respectively. The threshold current scales perfectly with the number of devices driven in parallel. Also differential quantum efficiency is constant for all cases just above threshold. At higher driving currents the parallel driven devices suffer from additional cross heating resulting in a power penalty compared to the sum of the output powers when driven separately. The total optical power of an array can be calculated by applying the functional behavior of the thermal crosstalk versus device spacing to the simple modeling of output power versus laser current introduced in [4]. The result is

$$P_{opt,array} = \sum_{j=1}^{n} \frac{\hbar\omega}{q}(i_j - i_{th})\eta_d \cdot (1 - \frac{\sum_{m=1}^{n} R_{th,jm}((u_k + i_m \cdot R_d)i_m - P_{opt,m})}{\Delta T_{off}}). \quad (2)$$

The first factor in the sum describes the optical output power of an undisturbed individual VCSEL of constant injection efficiency, whereas the second part accounts for the thermally induced decreasing differential efficiency due to superposition of self- and cross-heating. Mounted test structures show the same measured improvements for both the thermal resistance and the thermal cross-resistance. The simulated dashed LI curves in Fig. 3 for the individually operated elements of the test structure and the resulting simulated output characteristics for the devices driven in parallel show excellent agreement with the measured solid curves. This confirms that the presented model can be used as a powerful tool for estimating the output characteristics of densely packed arrays as a function of device size, device spacing, and number of elements.

3. Two-dimensional densely packed bottom-emitting array

We have fabricated two-dimensional arrays with 23 individual elements arranged in a honeycomb structure as shown in Fig. 4 in order to achieve the highest packing density and a highly symmetrical thermal interaction. The mesa diameters are 40 μm and the center spacings amount to 90 μm. Fig. 5 depicts the

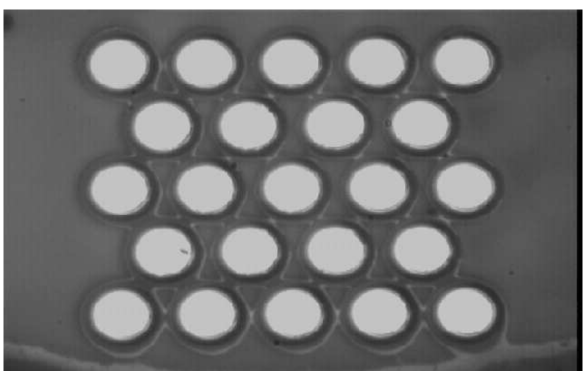

Fig. 4. Honeycomb arrangement of a 23 element VCSEL array. The device spacing is 90 μm. View of epitaxial side.

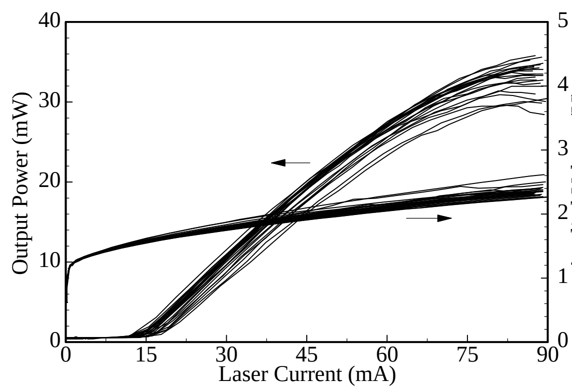

Fig. 5. Light-current and voltage-current characteristics of the 23 individual lasing array elements before mounting.

output characteristics of the unmounted individually driven elements. The 23 LI curves show good homogeneity in threshold currents of about 15 mA, threshold voltages of 1.6 V, and about 50 % differential quantum efficiency. The differential resistance is 10 Ω. The maximum conversion efficiency of 22 % is reached at three times threshold current. Thermal rollover occurs at six times threshold current at a maximum output power of about 30 mW per element.

Soldering the array junction-side down onto the heat sink, all 23 elements are electrically connected in parallel. The solid lines in Fig. 6 correspond to the experimentally obtained output characteristics of the mounted array. The threshold current of 340 mA is exactly 23 times the threshold current of an individual device. The differential quantum efficiency is slightly reduced to 43 %. Due to additional series resistances by non-optimized solder and mounting techniques, the differential resistance is 1.15 Ω. Therefore

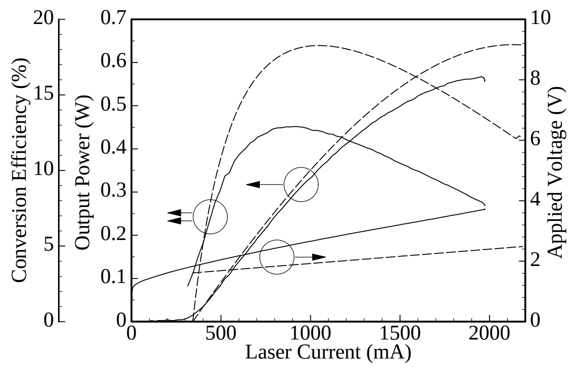

Fig. 6. Comparison of measured (solid) and simulated (dashed) total output characteristics of the mounted two-dimensional VCSEL array where all 23 lasing elements are driven in parallel.

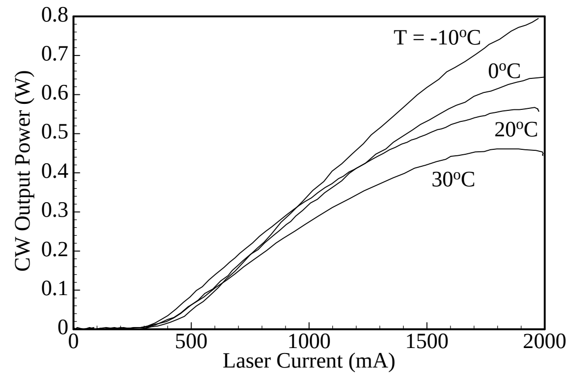

Fig. 7. Temperature dependent output characteristics of the mounted array.

threshold voltage is slightly increased to 1.8 V and conversion efficiency is limited to 13 % at almost three times the threshold current. The maximum output power at thermal rollover is 0.56 W at an array current of 2 A. The dashed lines in Fig. 6 represent the results from simulations using equation (2) and the extracted parameters from the individual unmounted VCSELs. The simulated LI curve fits the measured one quite well, although the quantum efficiency is slightly smaller in the experiment. Since the increase in series resistance due to mounting is neglected the differential resistance of 1.15 Ω is underestimated in the model giving 0.44 Ω. Therefore the maximum conversion efficiency is overestimated to about 18 %, which, however, can be taken as guideline for optimum mounting.
Temperature dependent LI characteristics of the array are presented in Fig. 7. For heatsink temperatures between -10°C and 30°C the threshold current only varies slightly, the minimum threshold current is obtained at room temperature. For lower heat sink temperature heat removal is more efficient resulting in a maximum output power of 0.8 W for a laser current of 2 A and a heat sink temperature of -10°C where no thermal rollover is observed yet. The corresponding spatially averaged power density is 0.47 kW/cm^2.

4. Summary

Densely packed two-dimensional bottom-emitting VCSEL arrays have been fabricated and mounted. Detailed investigations of the thermal interplay between individual elements considered in a simplified simulation of output characteristics show quantitatively the output power limitation by both thermal effects, self and cross heating. In experiments 0.56 W and 0.8 W optical output power at room temperature and -10°C, respectively, are observed. The maximum spatially averaged power density of 0.47 W/cm^2 is promising for of high power applications.

References

[1] G. Reiner, E. Zeeb, B. Möller, M. Ries, and K.J. Ebeling, “Optimization of planar Be-doped InGaAs VCSELs with two sided output”, *IEEE PTL*, vol. 7, pp. 730-732, 1995.

[2] K. Choquette, “Fabrication technologies of vertical cavity lasers”, *TOPS Vol. XV, Advances in VCSELs*, pp. 200–216, 1997.

[3] R. Michalzik, M. Grabherr, and K.J. Ebeling, “High-power VCSELs: Modeling and experimental characterization (invited)”, in *Proc. Optoelectronics ’98 - Vertical-Cavity Surface-Emitting Lasers II*, vol. 3286, pp. 206–219, San Jose, California, USA, Jan., 1998.

[4] M. Grabherr, M. Miller, R. Jäger, R. Michalzik, U. Martin, H. Unold, and K. J. Ebeling, “High power VCSELs - single devices and densely packed arrays”, *submitted to IEEE J. Selected Topics Quantum Electron.*, 1998.

[5] M. Grabherr, R. Jäger, M. Miller, C. Thalmaier, J. Heerlein, R. Michalzik, and K. J. Ebeling, “Bottom-emitting VCSELs for high cw optical output power”, *IEEE Photon. Techn. Lett.*, vol. 10, pp. 1061–1063, 1998.

CAIBE etching for high-quality GaN Homoepitaxy

Markus Schauler and Christoph Kirchner

Chemically-assisted ion-beam etching (CAIBE) was used to remove sub-surface damage from polished GaN bulk substrates prior to growth. Subsequently, GaN layers were deposited by metal organic vapor phase epitaxy (MOVPE). Only the CAIBE-treated areas reveal a mirror-like surface without trenches, scratches, or holes. A dramatic increase of crystal quality is determined by low-temperature cathodoluminescence (CL). Compared to not CAIBE-treated material, the CL intensity is improved by a factor of 1000 and the linewidth is ten times narrower.

1. Introduction

Due to its excellent optical and electrical properties, GaN attracts attention of numerous research groups worldwide. The wide direct bandgap, the thermal, mechanical, and chemical robustness, and the high luminescence efficiency make group III-nitride semiconductors the superior material system for optoelectronic devices in the ultra-violet to visible range. Despite the advantages of group III-nitrides, the technology still suffers from mismatched heteroepitaxial growth. Mismatch in lattice constants and thermal expansion coefficients between substrate (mostly sapphire or SiC) and epitaxial layer inhibit perfect crystal formation, resulting in 10^9 to 10^{10} dislocations per cm^2. Additionally, the low thermal conductivity of sapphire limits heat dissipation. Further limitations for devices derive from different crystal orientations between sapphire and GaN layer, which complicate cleaving of laser facets. Since those problems do not exist with GaN substrates, by definition, this promising approach is currently under investigation for devices. First light-emitting diodes grown on GaN bulk substrates where twice as bright as their counterparts on sapphire, which is attributed to the lower dislocation density and a higher hole concentration [1].

2. Experimental

The single crystal GaN substrates used in the present work have been produced from gallium melts under high nitrogen pressure and high temperatures by the High Pressure Research Center (Unipress) in Warsaw [2]. This process yields flat GaN platelets with a size of approx. 100 mm^2. The [0001] axis is perpendicular to the substrate surface. Top and bottom side have a different chemical behavior [3]. The N-side can be mechano-chemically polished whereas the inert Ga-terminated side can be mechanically polished only. Despite its inertness, the Ga-terminated side is favorable for device fabrication, since the N-side incorporates easier donors, but less acceptors. All following process steps are done on the Ga-terminated (0001) side of the crystals.

First, the Ga-terminated side was mechanically polished. This process is known to create sub-surface damage, that interferes with the later epitaxial growth. In conventional III-V-technology, this damage is chemically removed, a method not possible for nitrides, as there is no suitable etchant known. We investigated the suitability of CAIBE to remove sub-surface damage. Only one half of a sample is CAIBE treated, whereas the other is left unetched for comparison. Therefore, the sample surface is partially coated with photoresist, acting as an etch mask. Then, the etching is done at a substrate temperature of 25 °C using 6 sccm argon and 4 sccm chlorine, for 10 minutes process time, resulting in an etch depth of approx. 300 nm. Despite the use of chlorine, the etch process is dominated by the physical component, since the etch rate depends only weakly on the chlorine flux. Sputtering induced crystal defects are minimized by decreasing the ion energy from initial 400 eV to 100 eV at the process end. Nevertheless, the process is supposed to create ion damage up to 8 Å deep.

After stripping the photoresist, GaN films are deposited in a horizontal, radio-frequency heated, water cooled quartz MOVPE reactor (AIXTRON AIX 200 RF), operated at low pressure. Trimethylgallium (TMGa) and ammonia are used as group III- and group V-precursors, respectively. Following an initial 10 minute annealing step at 1030 °C, under a steady flow of ammonia, the undoped GaN is grown to a nominal thickness of 1.5 μm. During the growth, the V/III-ratio is kept at 4000 and the temperature is 1030 °C.

The low-temperature (5 K) cathodoluminescence measurements were performed at the Institut für experimentelle Physik at Otto-Gericke University in Magdeburg. With the equipment available there, a resolution of about 1 μm is achieved.

Figure 1a shows a SEM micrograph of an epitaxial GaN layer. The upper part of the image is the epitaxial layer grown on the previously dry-etched region, whereas the lower part is grown on the formerly masked, not CAIBE-treated area. The CAIBE-etched part of the sample reveals an improved surface topology with almost no visible scratches, trenches, or holes. Figure 1b shows the CL intensity distribution of the same region of the sample. On the etched part, the intensity variation is almost negligible. In contrast, the area being not etched yields only weak CL signals (1000 times less intensity) which also fluctuate locally.

The comparison of local CL spectra of epitaxial GaN layers grown on etched and unetched GaN substrates in figure 2 reveals large differences. The measured linewidth of the spectrum obtained on top of the pretreated region (fig. 1a, area A) is about ten times narrower then that of the non-etched region(fig. 1a, area B). However, the CL measurements are known to be still resolution limited by the spectrometer employed. This is confirmed by photoluminescence (PL) measurements which yielded a linewidth below 1 meV, however, being still resolution limited [4].

3. Summary

In conclusion, the developed dry-etching CAIBE process is a well-suited treatment to eliminate polishing-induced sub-surface damage. The crystal quality achieved is significantly better than that of the best heteroepitaxial material. This defect-free etching process has proven to be an excellent tool for fabrication of device structures that need an overgrowth process during fabrication e.g. DFB laser diodes.

References

[1] A. Pelzmann, C. Kirchner, M. Mayer, V. Schwegler, M. Schauler, M. Kamp, K. J. Ebeling, I. Grzegory, M. Leszczynski, G. Nowak, and S. Porowski, "Blue light emitting diodes on GaN substrates, growth and characterization", *J. of Crystal Growth*, pp. 167–171, 1998.

[2] H. Teisseyre, P. Perlin, T. Suski, I. Grzegory, S. Porowski, J. Jun, A. Pietraszko, and T. D. Moustakas, J. Apply. Phys. **76** 2429 (1994) .

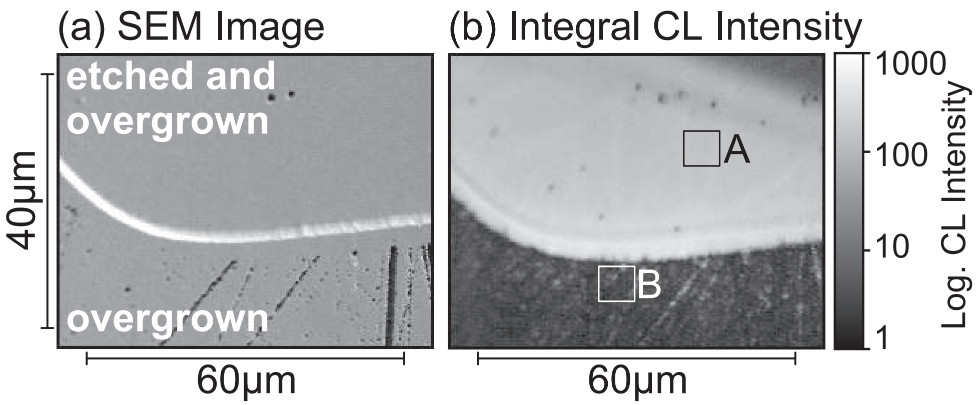

Fig. 1. SEM-Image (a) and CL intensity image (b) of an epitaxial GaN layer, grown on a (0001) oriented GaN substrate. The upper part of the image is the previously dry-etched region, whereas the lower part is the formerly masked, not CAIBE-treated area. The regions marked A and B in (b) refer to the local spectra depicted in Fig. 2.

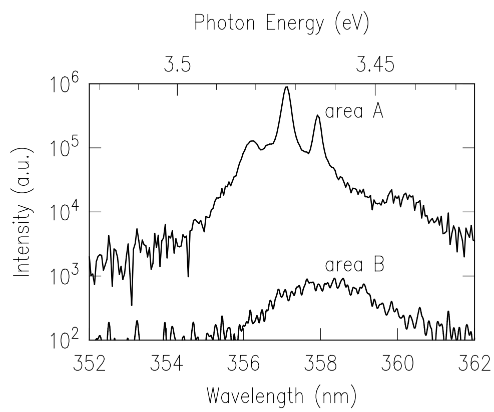

Fig. 2. Local CL-spectra (4K) of the epitaxial GaN-layer with (curve A) and without pre-growth CAIBE-etching (curve B). Curve A has about 1000 times the intensity of curve B.

[3] E. S. Hellman, D. N. E. Buchanan, D. Wiesmann, I. Brener, MRS Internet J. Nitride Semicond. Res. 1, 16(1996).

[4] C. Kirchner, “Homoepitaxial growth of GaN by MOVPE: A new benchmark for GaN technology”, Annual report 1998, Department of Optoelectronics, University of Ulm.

Etching Behavior of GaN Using Chemically-Assisted Ion-Beam Etching

F. Eberhard, M. Schauler, E. Deichsel, C. Kirchner

The characteristics of Cl_2-Ar chemically-assisted ion-beam etching processes for GaN is reported. The etch rate and anisotropy have been investigated varying ion energy, tilt angle, substrate temperature, and Cl_2 flow. Vertical and smooth sidewalls, which fulfill the requirements on laser facets, have been demonstrated in GaN.

1. INTRODUCTION

The fabrication of laser mirrors with a dry-etching process allows the monolithic integration of optoelectronic devices and a cost reduction by processing the lasers on a full-wafer basis [1]. Especially for GaN lasers, an etching process for the mirror facets is highly desirable since reproducible cleaving of GaN crystals grown on c-face sapphire is rather sophisticated and the quality of the cleaved surfaces is unsatisfying [2]. In chemically-assisted ion-beam etching (CAIBE), the physical component of the etching process (sputtering) can be separated from the chemical reaction on the substrate surface. This allows accurate control of the etched profile and an improved understanding of the etching mechanism. In this experimental study, we investigate the etching behavior of GaN.

2. EXPERIMENTAL

For the experiments we have used undoped GaN with good surface morphology grown by metal-organic vapor-phase epitaxy (MOVPE) on c-plane sapphire substrates. The samples have been dry-etched in a CAIBE system equipped with an electron-cyclotron-resonance (ECR) ion-beam source and a load lock. The substrate is located on a rotatable stage, that can be temperature controlled in the range of $-25\,^{\circ}\mathrm{C}$ to $125\,^{\circ}\mathrm{C}$. Additionally, the stage can be tilted relative to the ion beam, offering an extra possibility to control the profile of the etched structures. The chemically-reactive chlorine is introduced through a ring nozzle onto the substrate surface, whereas Ar is used as feed gas for the ion source. Detailed examinations have been performed by varying the ion-beam acceleration voltage U_{B}, the incidence angle of the ion beam α, the flow of the chemically-reactive gas ϕ_{Cl_2}, and the temperature of the substrate T.

For the fabrication of vertical and smooth dry etched mirrors, there are strict requirements regarding the etch mask. Characteristics of a good etch mask are high mechanical and chemical resistance, vertical profile in order to avoid facet roughing by edge erosion, and smooth facets [3, 4]. A trilevel-resist system has been utilized as etch mask. A hard-baked photoresist is used as bottom layer, covered with a 50-nm-thick Ge intermediate layer. The imaging layer is formed by a positive photoresist, which is structured by contact printing. The pattern transfer into the intermediate layer and the bottom layer is done by CHF_3/O_2 plasma etching (PE) and O_2 reactive ion etching (RIE), respectively. During the oxygen RIE, the top resist is also removed.

The sidewalls of the $2.4\,\mu$m high remaining hard-baked bottom layer are nearly vertical with a roughness of approximately 15 nm. In contrast to standard photoresist, this trilevel resist can withstand high

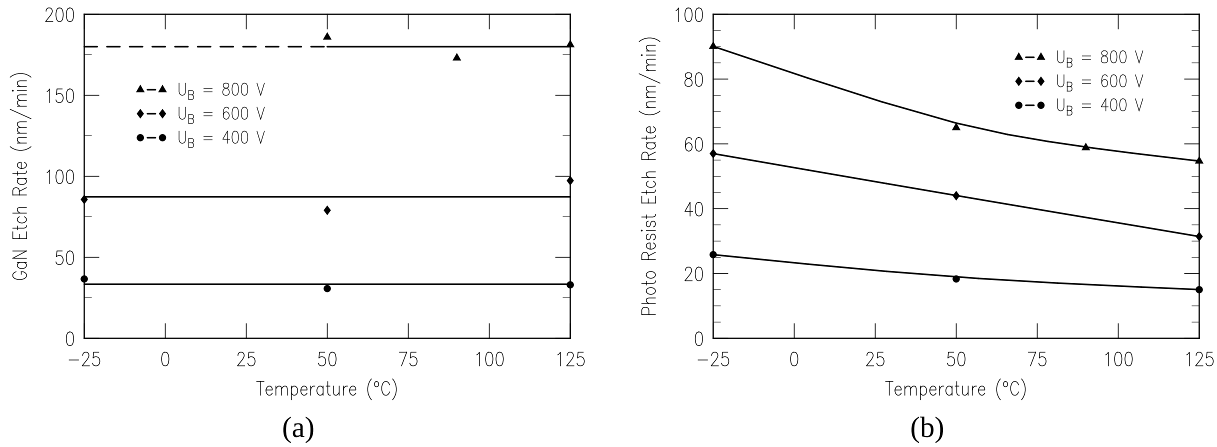

Fig. 1. Etch rate dependence of (a) GaN and (b) hard-baked resist on substrate temperature at various ion beam energies (ϕ_{Cl_2} = 4 sccm).

temperatures and high ion energies without undergoing severe degradation. After etching, the mask can be removed in an organic solvent.

3. RESULTS

The control of etch rate and anisotropy in CAIBE etching can be done by adjusting the physical and chemical component. The physical part is given by energy, current density and angle of incidence of Ar ions bombarding the substrate whereas the chemical contribution is determined by reactive gas flow and substrate temperature.

The etch rate data of GaN as a function of substrate temperatures are shown in Fig. 1a for ion energies of 400 eV, 600 eV, and 800 eV. The chlorine flow is maintained at 4 sccm, the argon flow is kept constant at 6 sccm. We observe a linear increase in etch rate with beam energy and beam current, as can be seen in Fig. 3a. For temperatures in the range of $-25\,°C$ to $125\,°C$ there is no significant change in the etch rate for all three ion energies. This indicates that etching of GaN is dominated by the physical etching component. It should be mentioned that at ion energies of 800 eV and temperatures lower than $50\,°C$ the

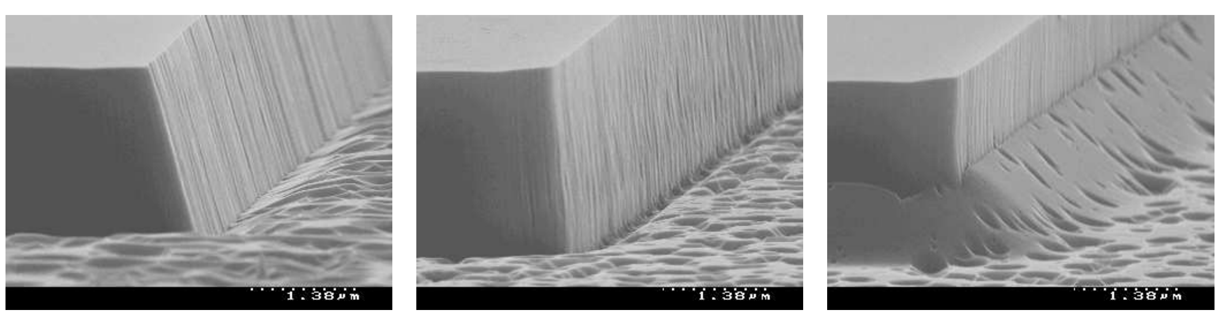

Fig. 2. GaN profiles etched at substrate temperatures and tilt angles of (a) $T = -25\,°C$, $\alpha = 0°$, (b) $T = 125\,°C$, $\alpha = 0°$, and (c) $T = 125\,°C$, $\alpha = 20°$. The ion-beam acceleration voltage is $U_B = 600$ V, the chlorine gas flow through the CAIBE ring nozzle is ϕ_{Cl_2} = 4 sccm.

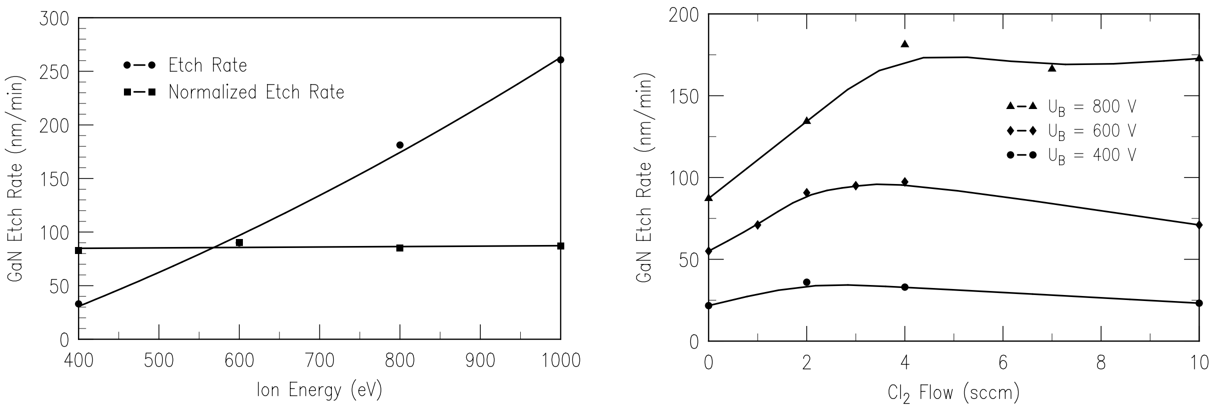

Fig. 3. Viewgraph (a) gives the dependence of etch rate on ion energy for a chlorine flow $\phi_{\mathrm{Cl_2}}$ of 4 sccm. The etch rate is normalized to $U_\mathrm{B} \cdot I_\mathrm{B}$. (b) Etch rate dependence of GaN on chlorine gas flow. The substrate temperature T is 125 °C.

bottom surface is very rough.

In contrast to the etch rate, the sidewall angle can be influenced by the ion energy and substrate temperature. For low temperatures, intense overcut profiles are achieved, as depicted in Fig. 2a. This sample has been etched at a substrate temperature of $T = -25\,^\circ\mathrm{C}$ and an ion energy of 600 eV resulting in a sidewall angle of about 15 °. By increasing the temperature to 125 °C, the sidewall angle can be reduced to 5 °, which is shown in Fig. 2b. Even steeper sidewalls can be achieved by raising the beam energy. At an ion energy of 1000 eV and $T = 125\,^\circ\mathrm{C}$ we observe a facet angle of 3 °.

A comparison between the etch rate of GaN and resist, both depicted in Fig. 1, shows that for high temperature and increasing ion energies the ratio of GaN etch rate to resist etch rate (selectivity) rises, leading to reduced mask erosion and therefore to reduced sidewall angles. The etch rate dependence of the hard-baked photoresist on temperature is not well understood, one possible reason is an increased reaction rate of photoresist and chlorine forming non-volatile chlorinated reaction products.

Another possibility to control the slope of the sidewall is to tilt the substrate relative to the ion beam. Fig. 2c shows GaN sample etched with a tilt angle α of 20 °. During the etching process, the sample has been rotated. Using this technique, we achieve vertical and smooth sidewalls which meet the requirements on laser facets. The lower sloped part of the facet, caused by shadowing of the ion beam by the etch mask, is not critical for laser facet applications. Increasing the tilt angle further leads to undercut profiles. The roughness of the etched sidewalls, which is mainly determined by the roughness of the etch mask, is approximately 15 nm and thereby well below 50 nm as reported for reactive ion etching (RIE) by Nakamura [2]. A possible drawback of tilting the sample is ion damage due to direct impingement of ions onto the facet surface.

The low chemical component in dry etching of GaN can be seen in Fig. 3b, showing the etch rate as a function of chlorine flow for ion energies of 400 eV, 600 eV, and 800 eV. Altering the chlorine flow from 0 sccm (sputter etching) to 2 sccm at an ion-beam voltage of $U_\mathrm{B} = 400\,\mathrm{V}$ increases the etch rate of GaN by 66 %. A further enlargement of chlorine flow brings about a decrease in etch rate, caused by energy loses of the Ar ions due to an increased number of collisions with chlorine molecules [3]. The enhancement in etch rate caused by chlorine increases to 107 % when the beam energy of 800 eV is used. At this energy, the maximum etch rate of 181 nm/min is reached at an chlorine flow of 4 sccm, resulting from increased consumption of chlorine atoms during etching.

4. CONCLUSION

In this paper we studied the dependence of etch rate and etch profile of GaN on reactive gas flow, substrate temperature, ion energy, and tilt angle. Our main motivation is to get vertical and smooth dry etched sidewalls for laser mirror application. Due to the low chemical etch part in GaN, it is not possible to achieve vertical profiles under vertical incidence of the Ar ions by choosing a balanced ratio of physical and chemical etching component as for GaAs [5]. Tilting the sample is therefore essential to achieve the desired profiles.

References

[1] P. Vettiger, M. K. Benedict, G.-L. Bona, P. Buchmann, E. C. Cahoon, K. Dätwyler, H.-P. Dietrich, A. Moser, H. K. Seitz, O. Voegeli, D. J. Webb, and P. Wolf, “Full-wafer technology–A new approach to large-scale laser fabrication and integration”, *IEEE J. Quantum Electron.*, vol. 27, pp. 1319–1331, 1991.

[2] S. Nakamura and G. Fasol, “The blue laser diode”, *Springer-Verlag*, Berlin, 1997.

[3] M. Hagberg, B. Jonsson, and A. G. Larsson, “Investigation of chemically assisted ion beam etching for the fabrication of vertical, ultrahigh quality facets in GaAs”, *J. Vac. Sci. Technol. B.*, vol. 12, no. 2, pp. 555–566, 1994.

[4] P. Buchmann, H. P. Dietrich, G. Sasso, and P. Vettiger, “Chemically assisted ion beam etching process for high quality laser mirrors”, *Microelectron. Eng.*, vol. 9, pp. 485-489, 1989.

[5] F. Eberhard, M. Schauler, E. Deichsel, C. Kirchner, and P. Unger, “Comparison of the etching behavior of GaAs and GaN in a chemically-assisted ion-beam etching system”, *accepted for publication in Microelectron. Eng.*, 1999.

RCE Photodetectors based on VCSEL Structures

Thomas Knödl

We have fabricated vertical-cavity surface-emitting lasers (VCSELs) based top illuminating resonant cavity enhanced (RCE) detectors simply by partially removing top mirror pairs of a VCSEL structure by wet-chemical or dry etching. The observed maximum quantum efficiency is 73 % with a spectral full width half maximum (FWHM) of about 1.7 nm. This particular RCE detector was fabricated by etching away eight top mirror pairs of a VCSEL structure, with 15.5 top mirror pairs remaining. The widest measured FWHM is 6.5 nm with a peak efficiency of 36 % in the case of 4.5 top mirror pairs remaining. An increase in the 3 dB detector bandwidth up to 2.8 GHz could be observed by reducing the active device diameter from 90 μm to 20 μm.

1. Introduction

An important figure of merit for photodetectors used in optical communications is the bandwidth-efficiency product. In conventional detectors thick active regions are required for high quantum efficiencies. Thick active regions, however, reduce device speeds because of the long transit times required. As a result, to optimize the gain-bandwidth product it is desirable to enhance quantum efficiency without increasing the active layer thickness. RCE photodetectors use thin active regions placed inside a Fabry-Perot resonant microcavity such as RCE Schottky [1], RCE PIN [2], and VCSEL based RCE detectors [3][4] to combine high efficiency and high-speed response. Therefore RCE photodetectors working at 850 nm and 950 nm offer the possibility to complement the high-performance VCSELs for short-distance optical communications.

A major advantage of using VCSEL sources together with VCSEL based RCE detectors on chip is, that they can share the same epitaxial layer structures and the same processing steps which makes this combination highly attractive for low cost integrated applications such as two-dimensional bidirectional optical interconnects [5].

2. Device Structure and Fabrication

The investigated top illuminating VCSEL sample grown by solid source molecular beam epitaxy (MBE) contains a half-wavelength thick inner cavity with three active GaAs quantum wells (QWs) of 8 nm thickness each. The top and bottom mirror consist of 23.5 carbon doped p-type $Al_{0.9}Ga_{0.1}As/Al_{0.2}Ga_{0.8}As$ and 32 silicon doped n-type $AlAs/Al_{0.2}Ga_{0.8}As$ Bragg reflectors, respectively. In order to achieve lateral current and optical confinement for VCSEL structures by oxidation, a 30 nm thick $Al_{0.96}Ga_{0.04}As/AlAs/Al_{0.96}Ga_{0.04}As$ layer is placed in the first quarter wavelength layer above the cavity.

To form the lateral patterning of the devices a standard VCSEL fabrication process is employed including wet-chemical mesa etching and selective wet oxidation, Ti/Pt/Au ring contact deposition, polyimide passivation and bondpad deposition. An additional photolithography step is required for reducing the reflectivity of the p-type top mirror of the RCE devices by etching. The removal of the mirror layers is achieved wet-chemical or dry etching, Fig. 1.

3. Experimental Setup

The problem of measuring RCE photodetectors is the narrow spectral bandwidth in the range of 1 nm to 7 nm due to the Fabry-Perot resonator. Therefore, fabricated single-mode VCSELs with an FWHM below 0.2 nm in continuous wave operation were chosen as a light source where the emission wavelength could be shifted of about 1 nm by varying the driving current. Fig. 2 shows the general measurement setup used in order to determine the quantum efficiency of the fabricated RCE devices. The quantum efficiency was calculated by measuring the photocurrent and the incident light power where it is assumed that the photocurrent is proportional to the absorbed power in the quantum wells. For this purpose,

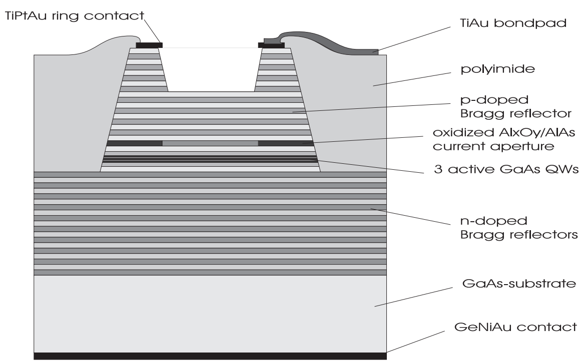

Fig. 1. Schematic of a VCSEL based top illuminating RCE detector including top mirror etching.

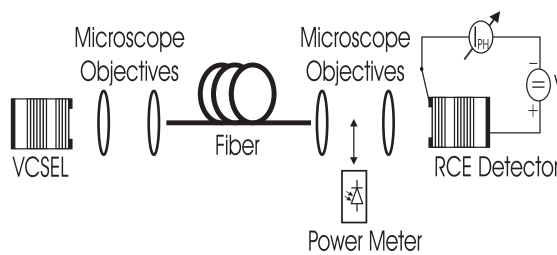

Fig. 2. General setup used for measuring the photocurrent as a function of the incident light power.

the laser emission was coupled into a 50 μm multi-mode fiber, transmitted to the detector setup and focused on the RCE detector where the photocurrent was measured at different applied voltages. The emission wavelength of the VCSEL was obtained by connecting the fiber to an optical spectrum analyzer (Anritsu) of 0.1 nm wavelength resolution. The power on the RCE detector side of the fiber was measured (Advantest, optical power meter) between the two lenses. In order to obtain the actual incident power on the detector surface, we multiplied the measured power by a correction factor which considered the loss of the microscope objective between the RCE detector and the power meter. The correction factor was set to 1.3 after comparing the power on both sides of the objective.

4. RCE Detector Measurement Results

The quantum efficiency spectrum of RCE devices allows one to obtain important information about the sensitivity and the wavelength selectivity of the detector. The left-hand side of Fig. 3 shows the influence of a reduced top mirror reflectivity on the quantum efficiency spectrum to the RCE detector. The insert shows an SEM picture of the device with 8 top mirror Bragg pairs removed by wet-chemical etching. The active device diameter is 100 μm. It is seen that the removal of eight top mirror pairs leads to a significant

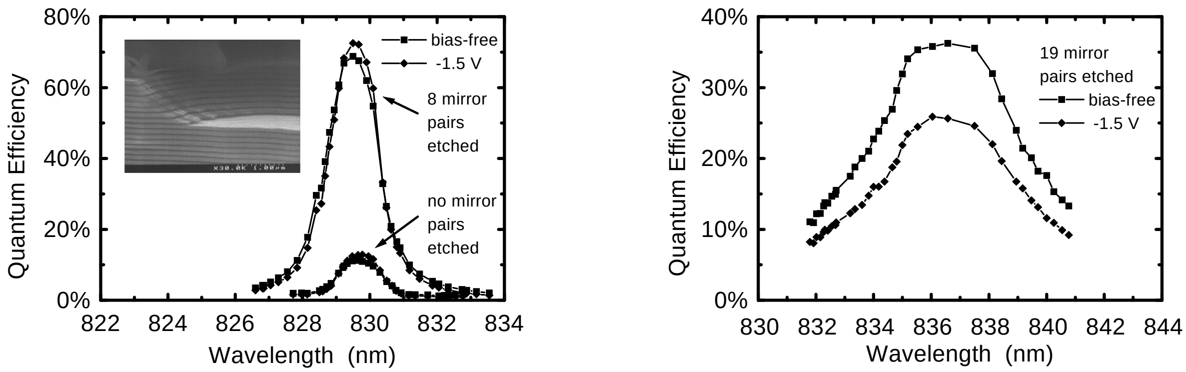

Fig. 3. Measured spectral quantum efficiency before and after etching of eight top mirror pairs (left-hand side) and after etching of 19 top mirror pairs (right-hand side) with respect to the applied reverse bias. The insert shows an SEM picture of a section with 8 top mirror pairs removed by wet-chemical etching.

improvement in the quantum efficiency and to a slight increase in the FWHM of about 0.2 nm. The peak quantum efficiency increases from 13 % for the non top mirror etched device up to about 73 % for the etched one with a related FWHM of 1.7 nm at a reverse bias of -1.5 V. The measured values in the bias-free case are 69 % and 1.8 nm for the peak efficiency and the FWHM of the eight mirror pairs etched device, respectively. An increase in the FWHM up to 6.5 nm is observed in the spectrum on the right-hand side of Fig. 3 where 19 top mirror pairs are etched away. The peak quantum efficiency of about 36 % is observed in the bias-free case. For an applied reverse bias of -1.5 V, however, the quantum efficiency is 26 % and thus resulting in an inverse voltage dependence compared to the previous devices. The influence of the top mirror reflectivity and the applied voltage on the maximum quantum efficiency and the related FWHM is summarized in Fig. 4. The voltage dependence of the quantum efficiency can be matched in transmission matrix simulations assuming a reduced QW absorption coefficient due to a reduced overlap of the electron and hole wave function with reverse bias [6][7]. The measurement results in Fig. 4 suggest that the boundary of increasing and decreasing peak efficiency with reverse bias locates between 12.5 and 15.5 top mirror pairs matching the theoretical obtained value of 13.5.

Figure 5 shows the modulation response of a 90 μm and 20 μm diameter RCE detector. The 3 dB bandwidths of the 90 μm and 20 μm diameter detector of 335 MHz and 2.5 GHz, respectively, are limited by parasitic oxide and space charge capacitances. This is also indicated by an increase of the 3 dB bandwidth up to 390 MHz and 2.8 GHz of the 90 μm and 20 μm diameter detector, respectively, due to an applied reverse bias.

5. Conclusion

In conclusion, we have fabricated RCE photodetectors adjacent to single-mode VCSELs by using the same epitaxial layer structure and lithography process. The significant change in the detector performance due to top mirror etching was demonstrated where we obtained 50 % quantum efficiency combined with 5 nm spectral half-width for a number of 8 top mirror pairs. A 3 dB bandwidth of 2.8 GHz was achieved for a 20 μm diameter detector. Thus, the characteristics of RCE photodetectors sharing similar epitaxial layer structures and the same processing steps as VCSELs are encouraging for densely integrated bidirectional optoelectronic chip interconnects.

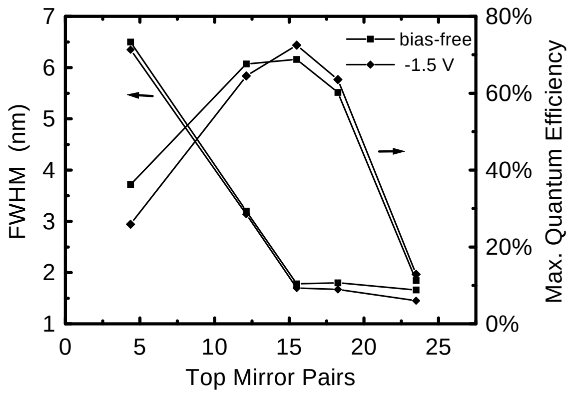

Fig. 4. Measured maximum quantum efficiency and the related FWHM as a function of top mirror pairs and applied reverse bias.

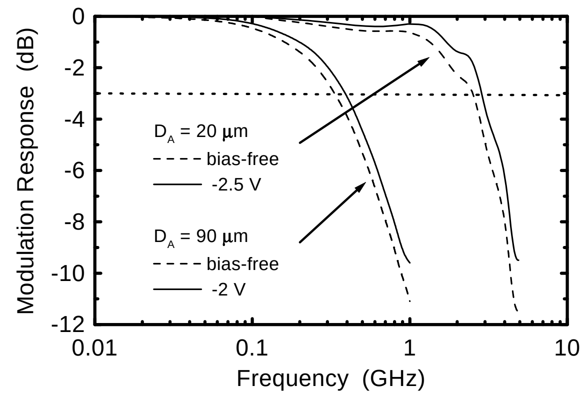

Fig. 5. Measured modulation response curves of detectors with 20 μm and 90 μm diameter for different applied voltages.

6. Acknowledgement

The author gratefully acknowledge the group of Prof. Clifton G. Fonstad at the Massachusetts Institute of Technology, in particular Henry Choy, for the valuable discussions about the RCE devices.

References

[1] B.M. Onat, M. Gökkavas, E. Özbay, E.P. Ata, E. Towe, and M.S. Ünlü, "100-GHz resonant cavity enhanced Schottky photodiodes", *IEEE Photon. Technol. Lett.*, vol. 10, pp. 707–709, 1998.

[2] C.C. Barron, C.J. Mahon, B.J. Thibeault, G. Wang, W. Jiang, L.A. Coldren, and J.E. Bowers, "Resonant-cavity enhanced p-i-n photodetector with 17 GHz bandwidth-efficiency product", *Electron. Lett.*, vol. 30, pp. 1796-1797, 1994

[3] H. Kosaka, K. Kurihara, M. Sugimoto and K. Kasahara, "Detector characteristics of a vertical-cavity surface-emitting laser", *Jap. J. Appl. Phys.*, vol. 30, pp. L 1172-L 1174, 1991

[4] M.S. Ünlü, S. Strite, "Resonant cavity enhanced photonic devices", *J. Appl. Phys.*, vol. 78, pp. 607-639, 1995

[5] R. King, R. Michalzik, D. Wiedenmann, R. Jäger, P. Schnitzer, T. Knödl and K.J. Ebeling, "2-D VCSEL arrays for chip-level optical interconnects", *to be published in Proc. of SPIE on Optoelectronic Interconnects VI*, vol. 3632, San Jose, CA, Jan. 1999.

[6] G. Bastard, E.E. Nendez, L.L. Chang and L. Esaki, "Variational calculations on a quantum well in an electric field", *Physical Review B*, vol. 28, pp. 3241-3245, 1983

[7] T. Knödl, *Resonant cavity enhanced photodetectors based on VCSEL structures*, Diploma Thesis, Dept. of Optoelectronics, University of Ulm, 1998

Mode analysis of Oxide-Confined VCSELs using near-far field approaches

Safwat William Zaki Mahmoud

We analyze the transverse mode structure of selectively oxidized vertical cavity surface emitting lasers (VCSELs) in the 850 nm spectral region using both near and far field approaches. The relatively strong index guiding devices show a noticeable reduction of the spot size whereas weak index guiding devices show large spot size. Also, we report a study on the butt-coupling efficiency of these devices using flat-cut uncoated single mode fibers (SMF) with different core diameters. The large core SMF diameter $D_F = 8.3\,\mu m$ *for standard 1300 nm wavelength data transmission require a simple filter to reduce the contribution of the excited higher order fiber modes.*

1. Introduction

In recent years the performance of vertical-cavity surface-emitting semiconductor lasers (VCSELs) has advanced. Using Al_2O_3 layers for fabrication, low threshold currents [1] and high efficiencies have been achieved [2]. The high index semiconductor surrounding the low index dielectric oxide material forms a lens-like element. This lens can partially compensate for the diffraction of the mode in the spacer regions and DBR's. In this paper, we present the Near Field (NF) and Far Field (FF) approaches that study the fundamental mode confinement of 850 nm VCSELs in which the oxide layer has different positions from the active layer and the node of the standing wave pattern.

2. Device Structure and Output Characteristics

The lasers studied are designed for emission near 850 nm wavelength, where the one wavelength thick inner cavity contains three active quantum wells, each has 8 nm thick GaAs separated by 10 nm $Al_{0.2}Ga_{0.8}As$ barriers, surrounded by carbon doped p-type $Al_{0.9}Ga_{0.1}As$-$Al_{0.2}Ga_{0.8}As$ and silicon doped n-type AlAs-$Al_{0.2}Ga_{0.8}As$ quarter wavelength Bragg reflector stacks. Lateral current confinement is achieved by selective wet oxidation of a single 30 nm thick AlAs layer embedded in a quarter wavelength layer, three mirror periods from the active region for sample A, and directly above the active region for sample B. Evaporation of TiPtAu ring contacts on the top side and GeNiAu on the bottom side is the final process of fabrication. Using the one-dimensional transfer matrix method [3] in such VCSEL structure we could determine the electric field amplitude and the wavelength detuning $\Delta\lambda_{ox}$ due to presence of oxide layer. Also, we used the formula $\Delta n_{eff} = n_{eff} \cdot \Delta\lambda_{ox}/\lambda_0$ to determine the effective cavity index Δn_{eff} in relation to the wavelength detuning $\Delta\lambda_{ox}$, the effective cavity index n_{eff} and the wavelength in the absence of the oxide layer λ_0. The position of the oxide layer is adjusted to be a small step far away from the node of the electric field for sample A, see Fig. 1 and for sample B to lie exactly in the node as shown in Fig. 2. The results indicate that the effective cavity index of sample A is five times larger than that of sample B and the latter has $\Delta n_{eff} = 1 \cdot 10^{-3}$. This indicates that the more the oxide layer approaches the node of electric field amplitude, the less the built-in effective index guiding. Fig. 3 depicts the continuous wave (cw) output characteristics of two different active diameter devices

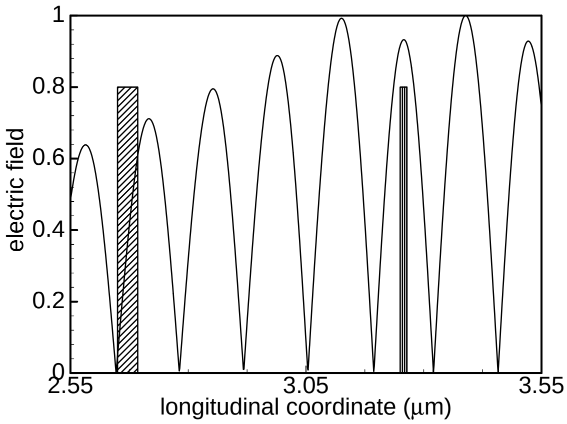

Fig. 1. The standing wave pattern of sample A.

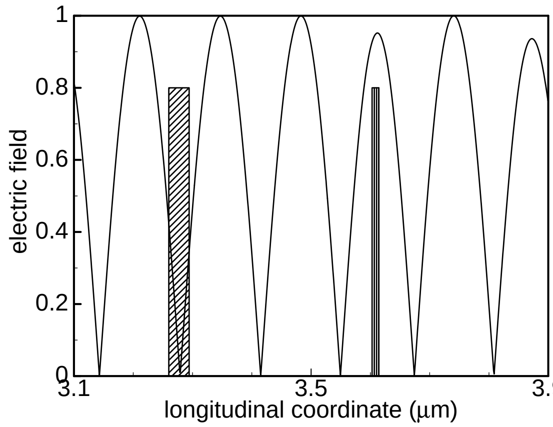

Fig. 2. The same as Fig. 1 but for sample B.

from sample A. The inset illustrates the oscillation of the two different VCSELs on the fundamental mode ($\lambda = 815\,nm$) at 2.5 mA current. Fig. 4 depicts also the characteristics of the different devices from sample B in cw operation, where the inset illustrates the spectra of the fundamental mode for these devices ($\lambda = 844.5\,nm$) at 2 mA current.

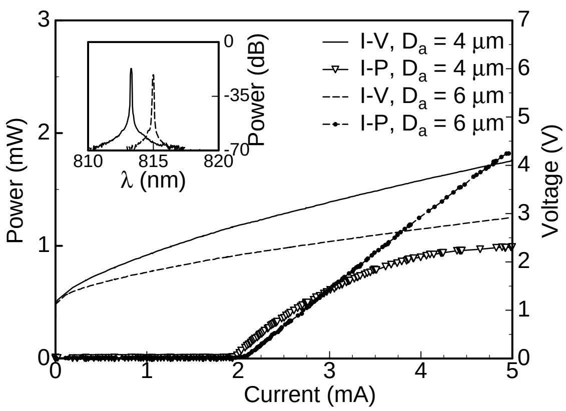

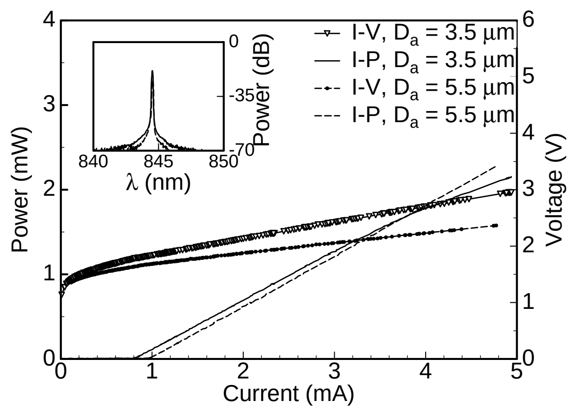

Fig. 3. The operation characteristic of two different VCSELs from sample A. The inset shows the spectra at 2.5 mA current.

Fig. 4. The same as Fig. 3 but for sample B and the inset shows the spectra at 2 mA current.

3. Experiment and Analysis

A) Experimental Setup

The setup for the NF experiment shown in Fig. 5 consists of a high precision 3-dimensional piezoelectric driven stage and the digital control electronics. High resolution sensors are installed as a feedback for positioning all three axes. Within the operating range of 100 μm for the three directions the resolution is better than 50 nm. Optical output power from the VCSEL is launched into the tapered tip of a single mode optical fiber with 10 μm core diameter and 2 m length. These fibers were fabricated specifically for these purposes where the tip is a semispherical lens with curvature radius $R = 6\,\mu$m. The tip collects

Tab. 1. The measured spot sizes w_L and the corresponding active diameters a for samples A and B.

Sample A		Sample B	
a (μm)	w_L (μm)	a (μm)	w_L (μm)
4.0	2.1	3.5	2.5
6.0	2.6	5.5	3.0

the light and couples it to the core of the fiber during scanning process. The transmitted signal is detected with a Germanium pin photodiode and converted into an analog signal through the optical power meter (OPM), which is connected with one of the general purpose analog inputs of the control electronics. The control electronics can thus read simultaneously the positioning through the three sensors and the analog input. Finally these data can be collected with the help of a simple PC program.

B) Comparison between Measurements and Calculations

The theoretical procedure outlined in [4] is used to calculate the NF and FF intensities of the Gaussian beam of full $1/e^2$ width $2 \cdot w_L$. The results of NF scanning for the smallest device from sample A at a single mode operating current are shown in Fig. 6 where the solid line represents the calculations and the triangle symbols represent the measurements. The measured FF intensity of this device is compared with the calculations and shown in Fig. 7. For sample B the results of NF scanning for the smallest device at a single mode operating current are shown in Fig. 8. Fig. 9 depicts the measured FF intensity of this device in comparison with the calculations. From these figures we can see the calculations fit well the experimental data. Table 1 summarizes the values of spot size corresponding to the different devices of the two samples. As one can see, the spot size of the devices belonging to sample A are less than that of sample B although the active diameter of these devices are larger than that of sample B. This indicates the presence of strong optical confinement in sample A which is due to the large effective index step.

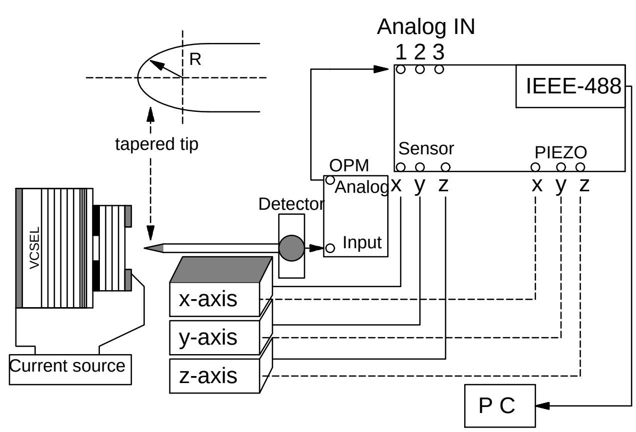

Fig. 5. Experimental setup for measurement of NF pattern from VCSEL.

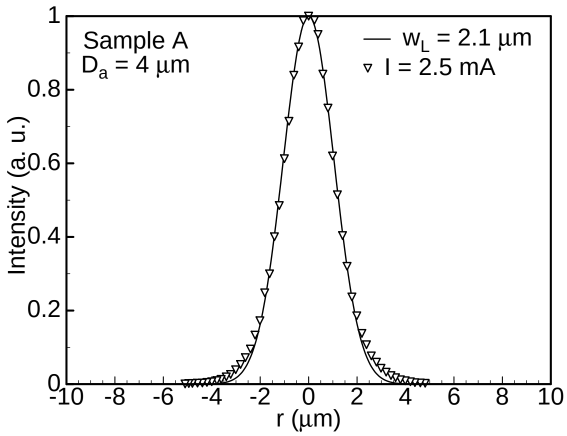

Fig. 6. Spatial distribution of light output from the smallest device of sample A in NF approach.

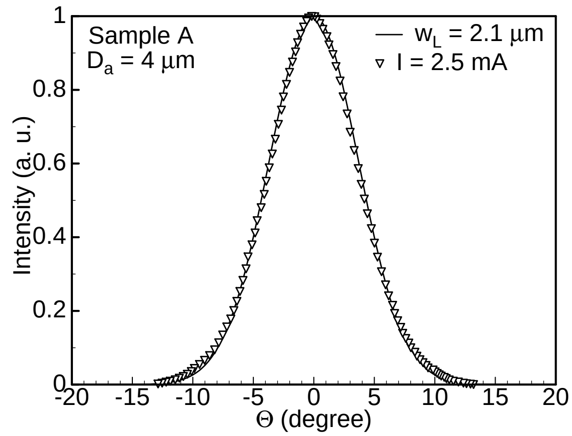

Fig. 7. Angular distribution of light output from the smallest device of sample A in FF approach.

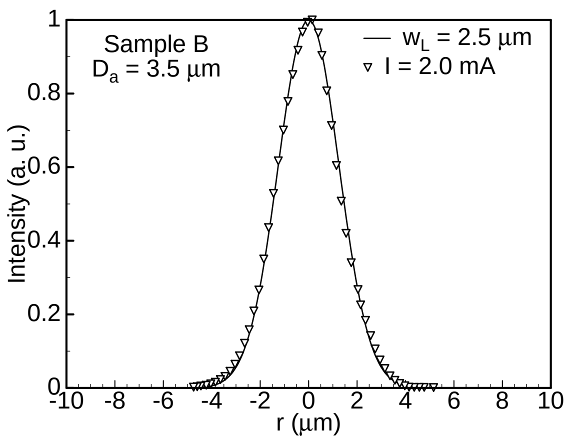

Fig. 8. The same as Fig. 6 but for sample B.

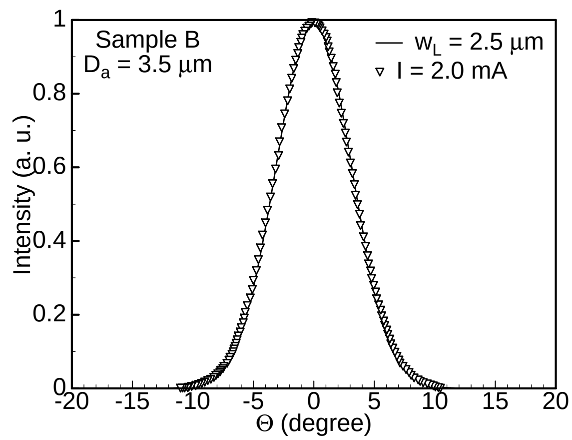

Fig. 9. The same as Fig. 7 but for sample B.

C) Coupling Efficiency

The butt-coupling efficiency η_c of VCSEL into flat cut single mode optical fiber (SMF) is measured using the NF scanning system with two different fibers of core diameters $D_F = 5\,\mu$m and $8.3\,\mu$m, respectively. Calculations using an overlap integral between Gaussian functions along with the parameters of the spot sizes given in Table 1 fit the experimental data well, as shown in Fig. 10 for the $5\,\mu$m core diameter SMF. In the case of $8.3\,\mu$m core diameter standard telecommunication SMF for 1300 nm, the given 850 nm range operating wavelengths results in a frequency parameter above the higher order mode cutoff value so that the fiber supports two modes. The contribution of the second mode is reduced by using a fiber loop with 12 mm diameter and 7 windings as shown in Fig. 11 where the solid line represents the calculations, the triangle symbols represent the measured data without filter and the plus symbols represent the measured data using the simple filter.

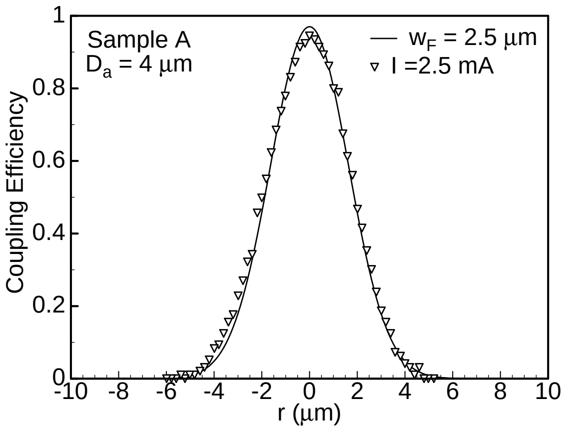

Fig. 10. The coupling efficiency of VCSEL from sample A into $5\,\mu$m flat cut SMF.

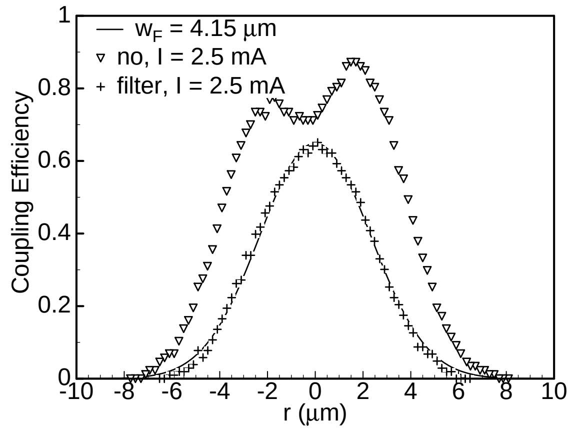

Fig. 11. The same as Fig. 10 but for $8.3\,\mu$m SMF.

4. Concluding Remarks

- The simple theoretical procedure predicts well the measured data which indicate that a stable positioning is achieved using the NF scanning system.
- The calculated butt-coupling efficiency of VCSELs into flat cut fiber using the measured parameters of beam half width yields good agreement with the measured data, i.e. the tapered tip optical fiber is suitable in NF scanning system.
- The inclusion of the simple filter in the case of large core diameter SMF leads to sufficient losses of the high order modes.

References

[1] D. L. Huffaker and D. G. Deppe, "Improved performance of oxide-confined vertical-cavity surface-emitting lasers using a tunnel injection active region", Appl. Phys. Lett., vol. 71,no. 11, pp. 1449–1451, 1997.

[2] R. Jäger, M. Grabherr, C. Jung, R. Michalzik, G. Reiner, B. Weigl, and K. J. Ebeling, "57% Wallplug efficiency oxide-confined 850 nm wavelength GaAs VCSEL's," Electron. Lett., vol. 33, pp. 330–331, 1997.

[3] P. Yeh, Optical Waves in Layered Media. J. Wiley & Sons, New York, 1988.

[4] D. Marcuse, Light Transmission Optics. Van Nostrand Reinhold Company, New York 1972.

Gas Source Molecular Beam Epitaxy of GaNAs and GaInNAs

Irene Ecker and Susanne Menzel

We report on the growth of GaNAs and GaInNAs layers with Gas Source Molecular Beam Epitaxy (GSMBE) using the alternative nitrogen precursors NH_3 and DMHy. Emission wavelengths up to 1260 nm in the quaternary alloy semiconductor GaInNAs are demonstrated.

1. Introduction

For fiber communication laser diodes with emission wavelengths of 1.3 and 1.55 μm are of great interest. The material system InGaAsP on InP substrate is suited for this wavelength range. Preferable would be a system which is compatible to the well-known GaAs technology. Combining GaInNAs with wide gap materials such as AlGaAs that can be formed on GaAs substrate provides better electron confinement so that the characteristic temperature (T_0) of long wavelength laser diodes can be improved in comparison to devices based on InGaAsP/InP [1].

This becomes more evident if one considers the relationship between lattice constant and bandgap energy in III-V semiconductors (Fig. 1). Adding of In to GaAs increases the lattice constant while incorporation of N decreases it. By appropriate choice of In to N content GaInNAs can be grown lattice-matched to GaAs. The observed reduction of bandgap energy through adding In and N is an untypical behaviour for quarternary III-V alloy semiconductors.

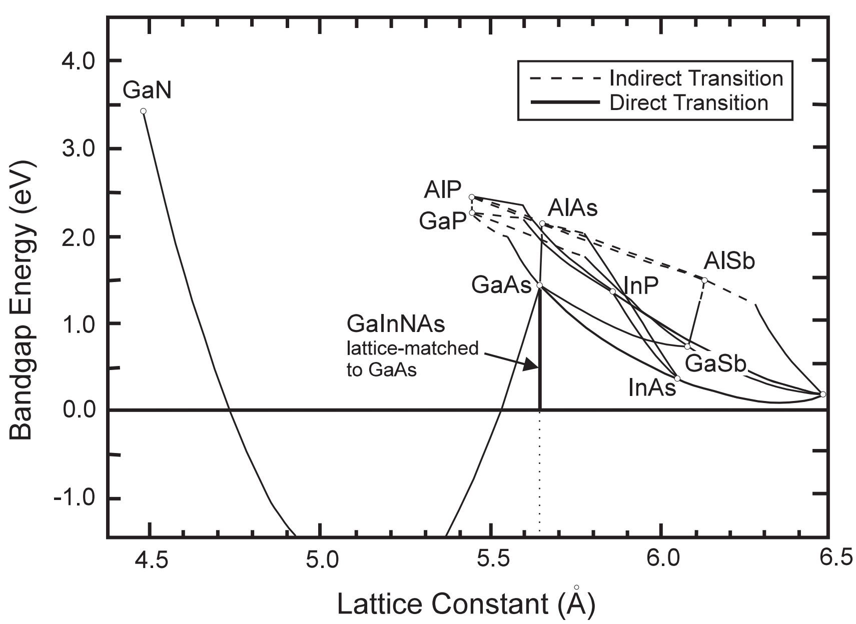

Fig. 1. Relationship between lattice constant and bandgap energy [1].

2. Nitrogen Sources

The growth of N containing layers requires efficient sources of reactive nitrogen. Usually plasma-assisted nitrogen sources are used [1]. The generation of reactive nitrogen is done by RF, ECR or DC discharge. However, the creation of high energetic ions can lead to damages of the crystal during growth. This results in a degradation of optical quality.

Therefore, we investigate the alternative nitrogen precursors NH_3 and DMHy. DMHy is a particularly attractive source because it decomposes at relative low temperatures on GaAs substrate [2].

3. Epitaxial Growth

Epitaxial growth is carried out in a modified Riber 32 P GSMBE. The injection of DMHy is made through a Low (LTI) and the injection of NH_3 through a High Temperature Injector (HTI). The Group-III-Elements In and Ga are provided as elements in effusion cells. The hydride arsine (AsH_3) serves as Group-V-precursor. As substrate semi-insulating (100) GaAs of epi-ready quality is used.

4. Material Characterization

Detection of nitrogen incorporation and its consequences on material quality and emission wavelength is measured by X-ray diffraction (XRD) and photoluminescence (PL).

A) Nitrogen Incorporation in GaNAs

The investigated samples are all of the same structure. After a 230 nm thick GaAs buffer follows a GaNAs layer of 100 nm.

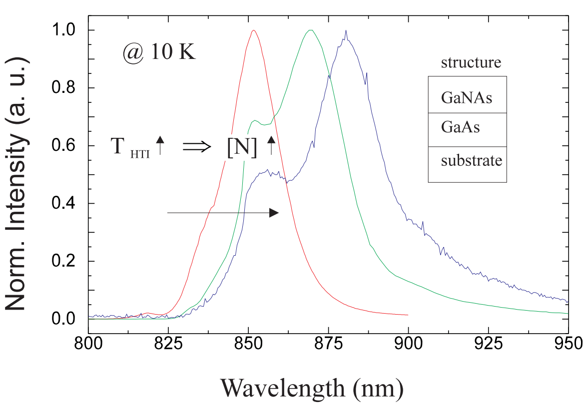

Fig. 2. PL spectra of samples grown with NH_3.

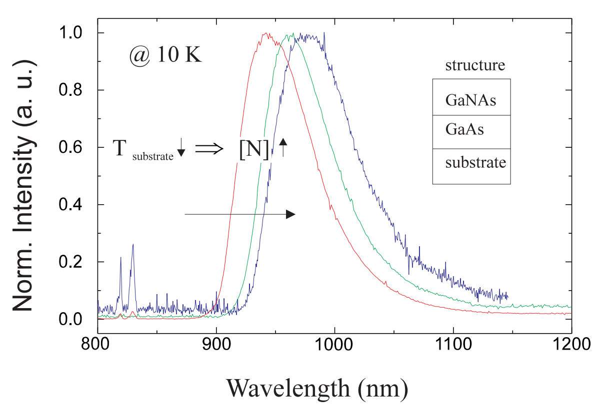

Fig. 3. PL spectra of samples grown with DMHy.

With ammonia as nitrogen precursor one can recognize from the PL spectra that an increasing injector temperature leads to higher wavelengths (Fig. 2). For DMHy a reduction of substrate temperature results in longer emission wavelengths (Fig. 3).

From the corresponding X-ray measurements it is difficult to see a clear link between nitrogen incorporation and injector temperature for ammonia because of the relatively low nitrogen content (Fig. 4).

However, for DMHy as nitrogen precursor the relationship between substrate temperature and nitrogen incorporation is confirmed (Fig. 5). The redshift of the PL peaks from the bandgap of GaAs is consistent with the nitrogen concentration determined by XRD. Moreover the appearance of thickness fringes is an indicator for good interface quality.

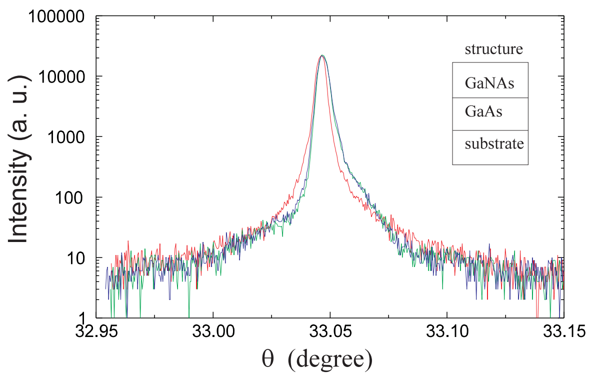

Fig. 4. XRD rocking curves of GaNAs/GaAs layers grown with NH_3.

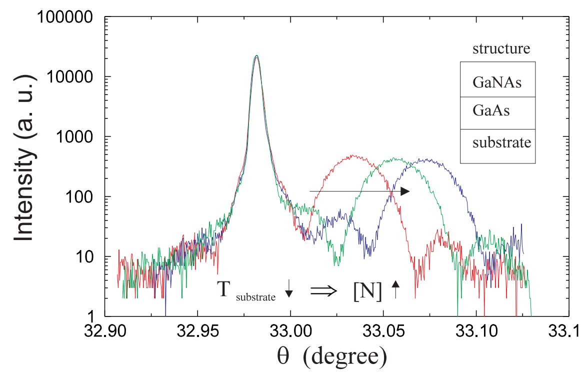

Fig. 5. XRD rocking curves of GaNAs/GaAs layers grown with DMHy.

Table 2 shows the comparison between the calculated nitrogen contents by PL and XRD measurements. The values obtained from photoluminescence were estimated using the following empiric equation [3]

$$E_g(x) = 1.42 - 20x + 280x^2 \qquad eV \qquad ([N] < 3\%) \tag{1}$$

Tab. 2. Comparison of nitrogen content as determined by XRD and PL for different nitrogen precursors.

NH_3			DMHy		
Sample	[N]		Sample	[N]	
$T_{HTI} \uparrow$	PL	XRD	$T_{substrate} \downarrow$	PL	XRD
X450	0.40		X563	1.16	0.71
X477	0.54		X535	1.38	0.99
X470	0.64	0.2	X533	1.49	1.23

With DMHy as nitrogen source a higher nitrogen incorporation in GaNAs is achieved. Latest results show an emission wavelength shift of 200 nm which corresponds to a nitrogen content of about 2 %.

B) Nitrogen Incorporation in GaInNAs

To verify nitrogen incorporation in the quaternary semiconductor GaInNAs samples containing two quantum wells are grown. The first pure InGaAs quantum well in the layer structure, shown as inset in Fig. 6, serves as a built-in reference for the second GaInNAs quantum well grown under identical conditions. Fig. 6 and 7 show the low- and room-temperature PL spectrum of a sample with the second quantum well grown under NH_3 injection. A peak wavelength shift of 40 nm of the GaInNAs quantum well compared to the reference InGaAs quantum well is observed.

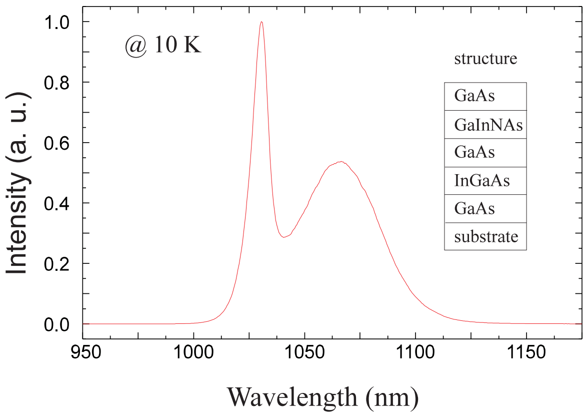

Fig. 6. Low-temperature PL spectrum.

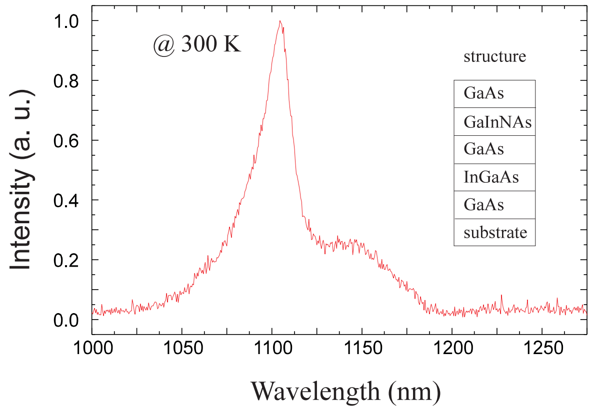

Fig. 7. Room-temperature PL spectrum.

Up to now wavelengths close to 1200 nm are demonstrated with NH_3. Employing DMHy emission wavelengths up to 1260 nm are obtained at room-temperature (Fig. 8).

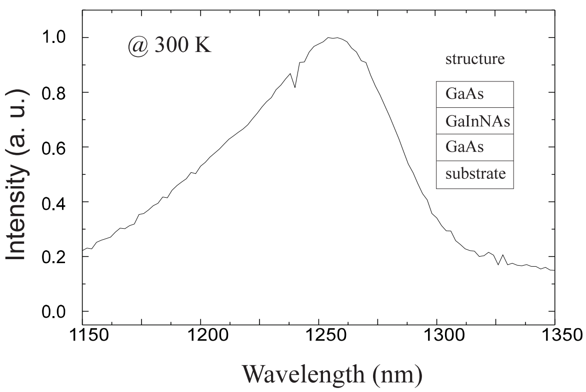

Fig. 8. Room-temperature PL spectrum of the depicted structure grown with DMHy.

5. Summary

GaNAs is successfully grown by GSMBE using alternative nitrogen precursors. With DMHy a maximum wavelength shift of about 200 nm, being equivalent to a nitrogen content of about 2 %, is achieved. In the material system GaInNAs wavelengths up to 1260 nm are reached. Further investigations will focus on device structures.

References

[1] M. Kondow, K. Uomi, A. Niwa, T. Kitatani, S. Watahiki and Y. Yazawa, “GaInNAs: A Novel Material for Long-Wavelength-Range Laser Diodes with Excellent High-Temperature Performance”, *Jap. J. Appl. Phys.*, vol. 35, no. 2B, pp. 1273–1275, 1996.

[2] Y. Qiu, C. Jin, S. Francoeur, S. A. Nikishin and H. Temkin, “Metalorganic molecular beam epitaxy of GaAsN with dimethylhydrazine”, *Appl. Phys. Lett.*, vol. 72, no. 16, pp. 1999–2001, 1998.

[3] K. Takeuchi, T. Miyamoto, T. Kageyama, F. Koyama, and K. Iga, “Chemical Beam Epitaxy Growth and Characterization of GaNAs/GaAs”, *Jap. J. Appl. Phys.*, vol. 37, no. 3B, pp. 1603–1607, 1998.

2D VCSEL Arrays for Chip-Level Optical Interconnects

R. King

Oxide-confined vertical cavity surface-emitting laser diodes (VCSELs) are fabricated for applications in chip-level optical interconnects. 980 nm wavelength devices in arrays with 4×8 elements are investigated. Threshold voltages of 1.5 V and operation voltages below 2 V of submilliamp threshold current lasers are fully compatible to 3.3 V CMOS technology. Modulation bandwidths of 9.5 GHz at 1.8 mA laser current with a modulation current efficiency factor (MCEF) of 10 GHz/$\sqrt{\mathrm{mA}}$ is demonstrated for 3 μm diameter VCSELs. No error floors are observed down to bit error rates (BERs) of 10^{-11} at 12.5 Gb/s data transmission.

1. Introduction

Parallel optical links will penetrate more and more into areas such as inter-cabinet and inter-board down to intra-board data communication, nowadays mostly dominated by electrical interconnect solutions. In recent years, one-dimensional parallel datacom links have accelerated progress in optical interconnect technology [1] but the hardware is too bulky and the aggregate bit-rate is far too low for chip-level interconnects. In order to satisfy the increased need for data throughput per area in chip-level links two-dimensional (2D) interconnects and integrated wiring-technologies such as flip-chip bonding are necessary. The left-hand side of Fig. 1 shows a schematic of a parallel optoelectronic interconnect on chip-level. Source and detector chips are directly bonded onto Si CMOS chips and the optical datastream is transferred from one chip to another chip using free-space optics or 2D waveguide arrays.

The right-hand side of Fig. 1 shows a photograph of a fabricated transmitter chip where a bottom-emitting VCSEL array with 4×8 elements is flip-chip mounted on a 0.8 μm CMOS driver chip [2]. Due to their high efficiency at low driving currents, high-speed data transmission capabilities and the possibility of 2D array fabrication as well as the intrinsic compatibility with fiber and free space optics VCSELs are regarded as a key enabling technology for low-cost chip-level optical interconnects.

2. Chip Fabrication and VCSEL Characteristics

The left-hand side of Fig. 2 shows a photograph of a 150 μm thick bottom emitting VCSEL array. The active region of an individual laser is formed by three 8 nm thick compressively strained $In_{0.2}Ga_{0.8}As$ quantum wells embedded in GaAs barriers for 980 nm emission wavelength. The inner cavity is sandwiched between an upper p-doped and a lower n-doped Bragg reflector, consisting of 20.5 and 30 quarter-wavelength $GaAs/Al_{0.88}Ga_{0.12}As$ layer pairs, respectively. Graded interfaces and δ-doping reduce series resistance significantly. Current is injected through the upper Bragg reflector by a full size p-contact. Current confinement is achieved by selective lateral oxidation of a 30 nm thick AlAs layer after mesa etching and stable single-mode emission is enforced by small oxide aperture and weak optical confinement. Polarization can be controlled using off-angled substrate or elliptical current apertures [3]. Mounting the array junction-side down is done straightforward since all electrical contacts are on the top-side

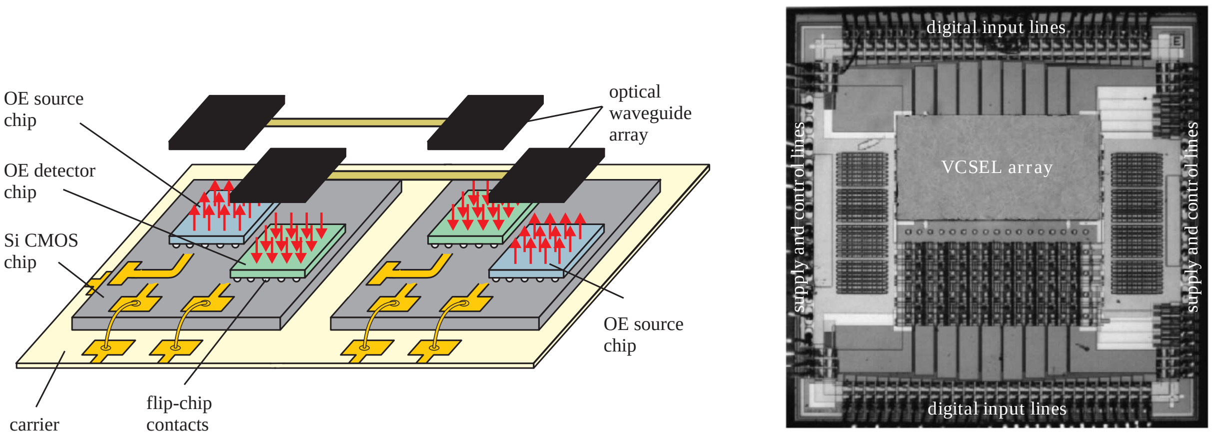

Fig. 1. Schematic of parallel optoelectronic interconnect on chip-level (left-hand side) and 4×8 VCSEL array flip-chip mounted on Si CMOS driver circuits (right-hand side).

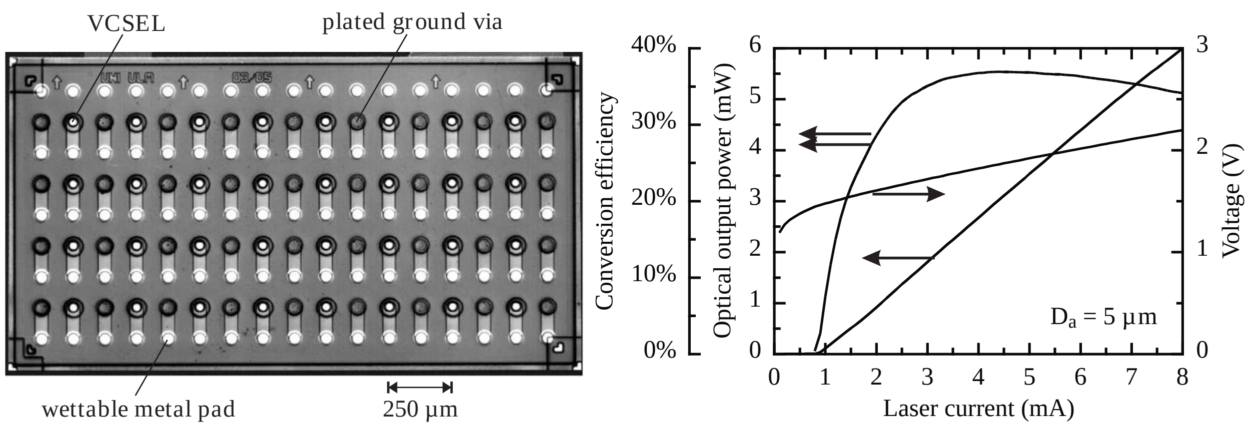

Fig. 2. Photograph of a bottom emitting 4×8 element VCSEL array with 250 μm pitch and two individual contacts per device (left-hand side) and operation characteristics of a 5 μm oxide diameter device within an array (right-hand side).

and laser emission occurs through the substrate at 980 nm wavelength. The layout concept can be carried forward to the optical interconnect standard 850 nm wavelength regime by employing, e.g., GaAs substrate removal after mounting [4]. The VCSELs are arranged at 250 μm pitch and have two contacts per device for individual high bit rate modulation. The VCSELs as well as the plated vias, which connect the n-contact to the top-side metallization, are connected by tracks to remote wettable metal pads.

The right-hand side of Fig. 2 presents driving and output characteristics of an array device with 5 μm active diameter. The threshold current is 0.9 mA and the threshold voltage is 1.45 V. At an optical output of 1 mW the voltage drop across the device is only 1.6 V. The operation characteristics of VCSELs designed to achieve low series resistances and high conversion efficiencies at low output power (e.g. 1 mW) are listed in Tab. 3

As the VCSEL source chips are to be mounted on Si CMOS chips which can get very hot it is important to know about the temperature dependence of the operation characteristics. Fig. 3 shows the variations of threshold currents and laser currents at 1 mW optical output as a function of heatsink temperature of

$D_a = 3\,\mu$m		$D_a = 5\,\mu$m		$D_a = 8.5\,\mu$m	
threshold	P_{opt}=1 mW	threshold	P_{opt}=1 mW	threshold	P_{opt}=1 mW
I=0.6 mA	I=1.8 mA	I=0.9 mA	I=2.1 mA	I=1.8 mA	I=3.1 mA
U=1.5 V	U=1.7 V	U=1.45 V	U=1.6 V	U=1.48 V	U=1.58 V
η_d=65 %	η=33 %	η_d=64 %	η=30 %	η_d=62 %	η=21 %
	R_d=155 Ω		R_d=107 Ω		R_d=71 Ω
P_{ds}=0.9 mW	P_{ds}=2.1 mW	P_{ds}=1.3 mW	P_{ds}=2.4 mW	P_{ds}=2.7 mW	P_{ds}=3.9 mW

Tab. 3. Operation characteristics of VCSELs with different active diameters.

three VCSELs with 5 μm active diameter. The In content of the QWs is chosen to obtain a gain peak wavelength of 955 nm at room temperature. At room temperature the cavity mode which determines the emission wavelength and the spectral gain peak of the VCSEL emitting at λ_{rt}=954 nm is aligned. The VCSELs emitting at λ_{rt}=967 nm and λ_{rt}=984 nm have a relative mode-gain misalignment of $+12$ nm and $+29$ nm at room temperature, respectively. The VCSEL with room temperature mode-gain detuning of $+29$ nm (triangles) operates as a temperature insensitive laser as the detuning at room temperature results in mode-gain alignment at a higher temperature. The wavelengths and the differential quantum efficiencies of the VCSELs shift at a rate of 0.07 nm/K and -0.2 %/K, respectively.

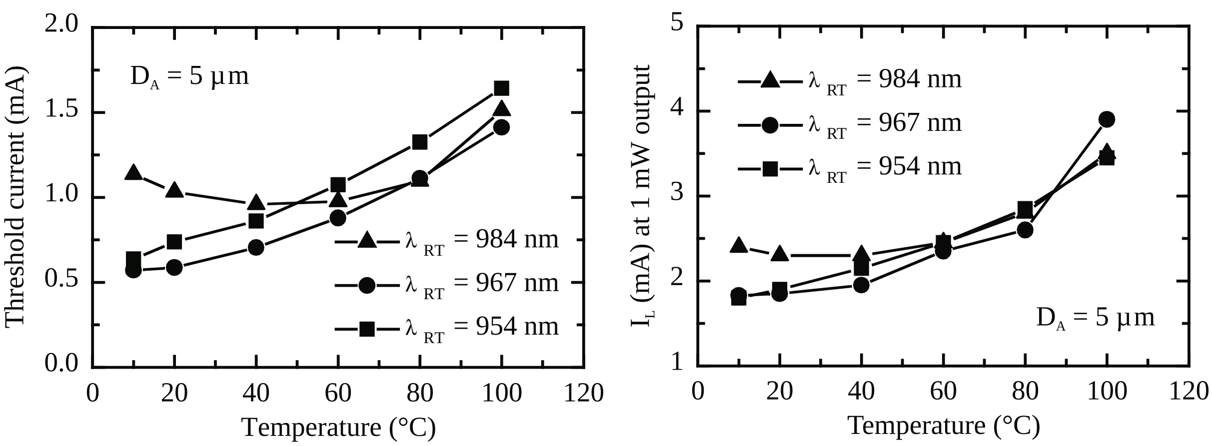

Fig. 3. Variations of threshold currents (left-hand side) and laser currents at 1 mW output power (right-hand side) as functions of heatsink temperature for the three VCSELs with different mode-gain offsets. The active diameter of the VCSELs is about 5 μm and the gain peak wavelength at room temperature is about 955 nm.

3. Small Signal and Large Signal Modulation Properties

The left-hand side of Fig. 4 shows the physical origin of an equivalent-circuit model for the VCSEL impedance behavior. The equivalent-circuit model takes into account bond pad capacitance C_{pad}, series resistance R_s, oxide aperture capacitance C_{ox}, and active layer series resistance R_a. Quantities of the various elements are obtained by fitting the model to the measured RF S11 parameters. For the vector high frequency impedance measurements individual lasers from a polyimide planarized $4{\times}8$ array are contacted with a coplanar probe tip. The model well describes the measured data up to frequencies of about 20 GHz. Tab. 4 gives determined parameters for three VCSELs of differing active and mesa diameters. Only R_a depends significantly on the bias current, the value listed here is for a bias current of 3 mA. The parameters scale with the dimensions of the VCSEL and therefore the physical origin proposed above seems reasonable. The solid lines in the right-hand side of Fig. 4 depict the bias

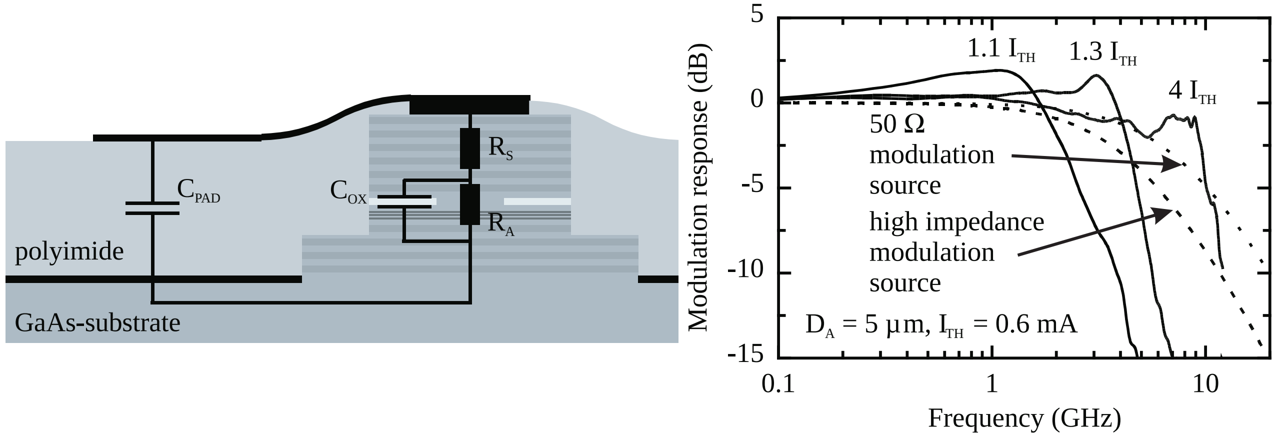

Fig. 4. An equivalent-circuit model for VCSELs (left-hand side) and measured (solid) small-signal modulation response curves of a VCSEL and calculated (dashed) low-pass filter curves for 50 Ω and high impedance modulation source (right-hand side).

D_a (μm)	D_m (μm)	R_s (Ω)	R_a (Ω)	C_{ox} (pF)	C_{pad} (pF)
3.5	32	55	100	0.56	0.13
5	34	46	61	0.68	0.13
8.5	38	36	35	1.0	0.13

Tab. 4. Equivalent-circuit parameters obtained by fitting the vector impedance of VCSELs with different active diameters (D_a) and mesa diameters (D_m).

dependent small-signal modulation response curves of a 5 μm VCSEL measured with a 50 Ω network analyzer. The fitted parameters from the equivalent-circuit model allow the calculation of the parasitic roll-off in the modulation response, also shown as dashed lines in the right-hand side of Fig. 4 for both a high impedance and a 50 Ω modulation source. The VCSEL modulation bandwidth is seen to be limited by the electrical parasitics.

The left-hand side of Fig. 5 illustrates the high speed characteristics at low bias currents obtainable from the VCSEL devices of various sizes. The 3 μm single-mode device exhibits a modulation current efficiency factor (MCEF) of 10 GHz/$\sqrt{\text{mA}}$ which decreases for larger diameter devices. We have employed a 3 μm VCSEL as transmitter in optical data links. The right-hand side of Fig. 5 shows the eye diagram at 12.5 Gb/s PRBS modulation and the bit error rate (BER) curves for back-to-back transmission and transmission over fibers. The VCSEL is biased at three times threshold and modulated with 1 V_{PP}. We used 100 m graded index multi-mode fiber (MMF) or 1.9 km of 9 μm core diameter standard single-mode fiber (SMF). In back-to-back transmission the minimum required power at the pin-InGaAs photodiode is -11 dBm to achieve a bit error rate of 10^{-11} at 12.5 Gb/s. This relatively high power is due to the low sensitivity of the 50 Ω pin-receiver used.

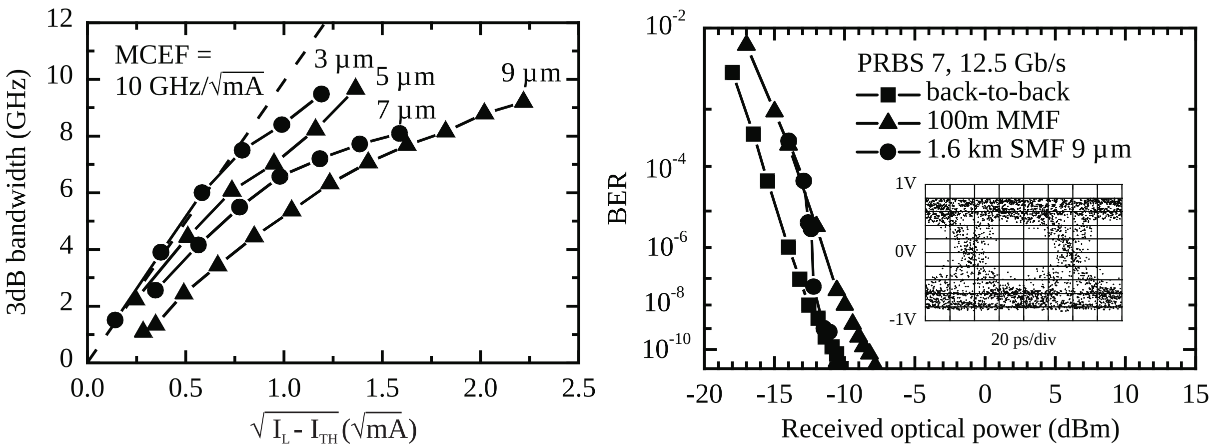

Fig. 5. Bias dependent modulation bandwidths of VCSELs of various sizes (left) and BER curves for different transmission channels using a 980 nm VCSEL with 3 μm active diameter (right).

4. Conclusion

We have designed, fabricated, and characterized selectively oxidized single-mode and multi-mode emitting VCSEL arrays ideally suited as transmitters in chip-level optical interconnects, both in terms of packaging and performance. Single-mode and multi-mode 4×8 VCSEL arrays are flip-chip mounted on Si CMOS driver chips in order to demonstrate VCSEL based optoelectronic transmitters on chip-level. The low-capacitance design of the arrays enables high-speed data transmission up to 12.5 Gb/s per element, far beyond the envisaged Gb/s CMOS speeds.

References

[1] H. Karstensen et al., in *Proc. 48th ECTC*, pp. 747–754, Seattle, WA, USA, May 1998.

[2] “http://www.intec.rug.ac.be/oiic.”

[3] T. Mukaihara et al., *IEEE J. Sel. Top. Quantum Electron.* **1**, pp. 667–673, 1995.

[4] K. D. Choquette et al., *Electron. Lett.* **34**, pp. 1404–1405, 1998.

Mirror Coatings for Edge-Emitting Lasers

Ulrich Martin

1. Introduction

Edge-emitting semiconductor lasers are used in a wide range of applications. This type of laser can be used as pump source for a solid state laser, as light emitter in a laser printer and as pump source for fiber optic data transmission. Especially the increasing requirements for data storage applications like CD-RAM, CD-ROM and Digital Versatile Disc (DVD) expands the spreading of semiconductor laser diodes in our daily work. In these applications, the laser devices have to work reliable without sudden failures and degradation. It is necessary to protect the facets of semiconductor laser diodes from environmental influences. Lasers with an antireflection coating on each laser facet can be used as optical laser amplifiers if the reflectivity is reduced to 10^{-4} [1]. Laser devices with a antireflection coating on one facet can be used for spectroscopy when combined with a grating as external reflector, since they are continuously tunable over a wavelength range of more than 25 nm [2]. Coatings for semiconductor lasers need different reflectivities at each facet. Figure 1 illustrates the schematic structure of a semiconductor laser device. The front side of the laser is covered with an antireflection coating to increase the light output of this facet. The desired reflectivity is determined by the length of the device and its application. On the backside of the laser is a high reflection coating to couple the laser light back to the device and reduce the output power at this facet. The coatings also have to exhibit a number of properties, e.g. chemical and mechanical stability, good adhesion to the facet surface, low mechanical stress, high transparency at the emission wavelength, and an excellent behavior with respect to lifetime and catastrophic optical mirror damage (COMD). For optical communication systems it is also necessary that the beam characteristics of the laser devices do not change.

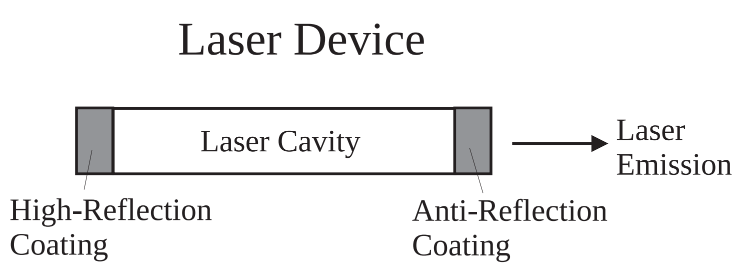

Fig. 1. Schematic illustration of a semiconductor laser with mirror coatings for optical emission on one mirror facet.

2. Antireflection Coatings

According to the Fresnel equation

$$R = \frac{(1-n_s)^2}{(1+n_s)^2} \quad , \tag{1}$$

an uncoated laser mirror has a natural reflectivity of $R = 0.3$. For this calculation, a refractive index of $n = 3.43$ is assumed, which is a good agreement to bandgap modeling theory and measurement of the group velocity of the laser light. To reduce the reflectivity at the facet, a single or a multi layer coating is needed. The reflectivity R of a single layer antireflection film with the thickness d and the refractive index n at a vacuum wavelength λ on a substrate with the refractive index n_s is given by the formula

$$R = \frac{(1-n_\mathrm{s})^2\cos^2(\delta) + (\frac{n_\mathrm{s}}{n} - n)^2\sin^2(\delta)}{(1+n_\mathrm{s})^2\cos^2(\delta) + (\frac{n_\mathrm{s}}{n} + n)^2\sin^2(\delta)} \quad , \tag{2}$$

$$\delta = 2\pi\frac{nd}{\lambda} \tag{3}$$

[3]. By changing the film material, the minimum of the reflectivity can be adjusted in a wide range. In our sputter deposition system we can vary the composition of the deposited material by changing the oxygen flux into the process chamber. So we can deposit nearly every material composition from silicon oxide to silicon nitride. By choosing another sputter target it is also possible to deposit aluminum oxide. Using these materials it is not possible to achieve the desired value of 5% to 10% for the front mirror reflectivity together with a minimum at the reflectivity versus wavelength curve. In this case the reflectivity depends on the emission wavelength as illustrated in Fig. 2. If we consider the tolerances of the film thickness

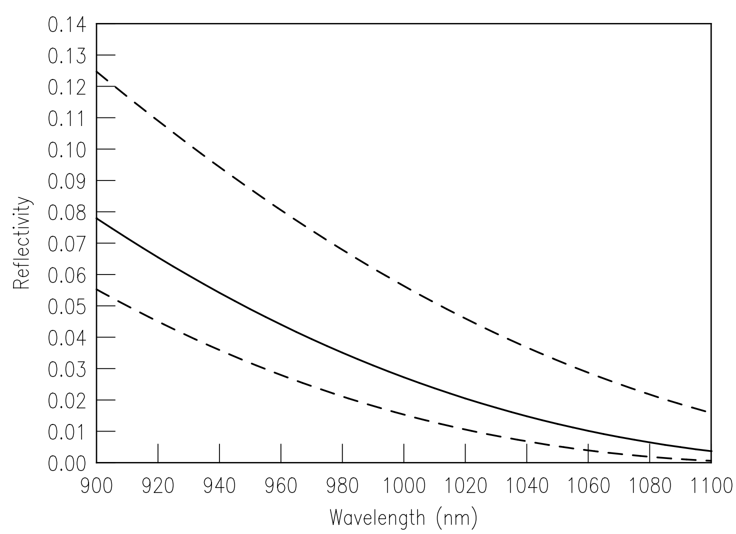

Fig. 2. Single layer design for a reflectivity of 5% at a wavelength of 950 nm.

after the depositioning process, the practical reflectivity value is in the range between the dashed lines in Fig. 2. So the practical reflectivity can vary between $R = 3\%$ and $R = 9\%$. Better deposition tolerance can only be achieved by an enormous effort. Another possibility is to use a multi layer coating to reduce the reflectivity at the laser facet. These coatings also have other advantages for semiconductor laser devices. On one hand, the spectral bandwidth is increased for the desired reflectivity value, which can be adjusted in a wide range. On the other hand, materials can be chosen with respect to lifetime and critical mirror damaging behavior. For the first tests, we designed a simple two layer antireflection coating to get information about processing and depositioning parameters. Figure 3 illustrates the simulation (line) and measurement result (circles) of such a coating. This type of coating can be realized with a higher reproducibility than a single layer coating in our deposition system.

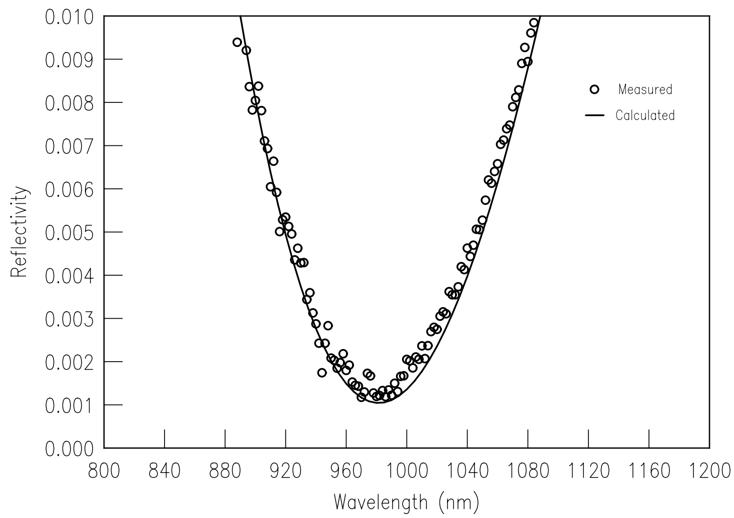

Fig. 3. Example of a two layer antireflection coating

3. High Reflection Coating

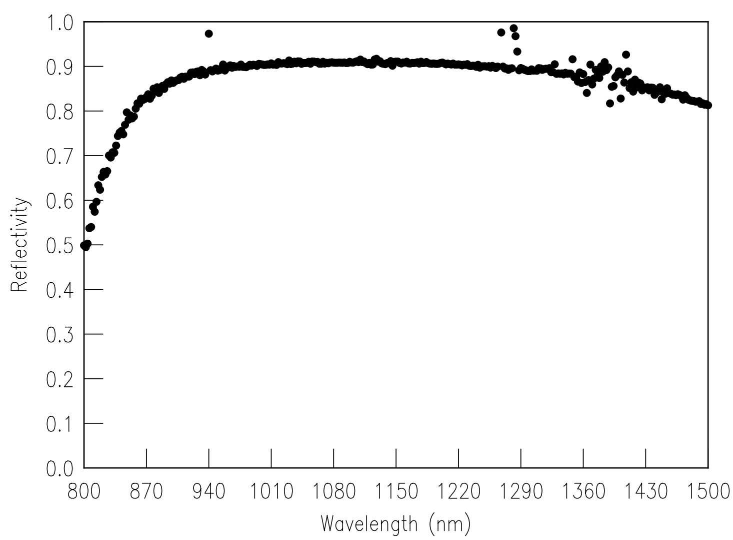

Fig. 4. Example for a high-reflection coating.

To increase the reflectivity of a laser facet it is necessary to use more than one dielectric coating layer. So a high reflection coating is composed of a number of layers with different refractive indices. Using a stack of quarter wavelength dielectric layers, the beams reflected from all interfaces in the assembly are of equal phase, they interfere constructively. By using material indices n_s,n_H,n_L of the substrate, the high-, and low- index material and p for the number of the layers, the reflectivity in air or free space is given by the formula

$$R = \left(\frac{(1 - (\frac{n_\mathrm{H}}{n_\mathrm{L}}))^{(2\cdot p)} \cdot \frac{n_\mathrm{H}^2}{n_\mathrm{s}}}{(1 + (\frac{n_\mathrm{H}}{n_\mathrm{L}}))^{(2\cdot p)} \cdot \frac{n_\mathrm{H}^2}{n_\mathrm{s}}} \right)^2 \tag{4}$$

[3]. The reflectivity increases with the number of layer pairs. To reduce mechanical stress and increasing the stability of the coating it is necessary to choose a layer material for good adhesion and reduce the number of layers to the lowest possible number which is necessary to reach the desired reflectivity. It is also a good idea to put some chemically inert material to the top of the layer stack to protect the coating and the laser facet from environmental influences. The same materials can be used to build a high reflection and an antireflection coating. So both coatings should have nearly the same mechanical and chemical properties. The reflectivity curve for a high reflection coating is shown in Fig. 4.

References

[1] G. Jost and U. Martin, *High-Quality Single-Layer Antireflection Coating,* Annual report 1997, Dept. of Optoelectronics, University of Ulm, pp. 20-23, 1997.

[2] Y. Yamamoto, *Coherence, Amplification and Quantum Effects in Semiconductor Lasers,* New York: John Wiley & Sons, 1990.

[3] H.A. Macleod, *Thin-Film Optical Filters, 2nd Edition.* Bristol: Adam Hilger, 1986.

850 nm transparent-substrate wafer-fused bottom-emitting VCSELs

Jürgen Joos

This report deals with the fabrication and characterization of bottom emitting VCSELs at an emission wavelength of 850 nm. The devices were realized by exchanging the absorbing GaAs substrate for a transparent GaP substrate using the wafer-fusion technique.

1. Introduction

Although vertical-cavity surface-emitting lasers (VCSELs) with emission through the substrate (bottom emitting device) are less prevalent than their counterparts emitting through the epitaxial surface (top emitting device) they offer several advantages. Bottom emitting VCSELs can easily be mounted upside down by a flip-chip technique onto high-speed CMOS chips in optical transceiver modules. They might be efficiently cooled by placing a heatsink near the active zone instead of on the opposite side of the considerably thick substrate, and finally, it is not necessary to leave an emission window in the top contact which leads to a less homogeneous carrier injection compared to full area contact devices.

Due to the fundamental absorption of GaAs at wavelengths shorter than 870 nm bottom emitting VCSELs at 850 nm need their GaAs substrate to be exchanged for a transparent material. GaP is an attractive solution because of its transparency and its conductivity although its lattice constant (0.5451 nm) is severely differing from the one of GaAs (0.5653 nm). Wafer-fusion in contrast to epitaxial techniques offers the possibility of combining semiconductor materials with significantly different lattice constants. This has been demonstrated by the fusion of InP and GaAs in long-wavelength VCSELs [1] as well as GaP and InAlGaP in high-brightness $(Al_xGa_{1-x})_{0.5}In_{0.5}$/GaP LEDs [2]. The conception of the wafer-fused transparent-substrate 850 nm VCSEL is sketched in Fig. 1.

2. Technological Details

The fabrication of the devices starts by etching grooves using chemically assisted ion beam etching (CAIBE) into the GaP material that prevent residual gases and liquids from being captured at the fused interface during the fusing process. A subsequent thorough cleaning of both of the samples – the GaAs-based VCSEL structure as well as the GaP substrate – ensures that no native oxide or organic contamination affects the electrical or optical quality of the interface. The wafer-fusion is carried out at Temperatures of 675 °C or higher under elevated mechanical pressure for 30 minutes. After removing the GaAs substrate by polishing and selective wet-chemical etching the devices are fabricated by standard VCSEL processing techniques including mesa etching, oxidation for current confinement, and contact metal evaporation.

This concept is similar to the one published by Sandia National Laboratories in [3]. In contrast to our structure they use n-type GaP and, according to this, an n-type top DBR in order to get an n-n-junction at the fused interface.

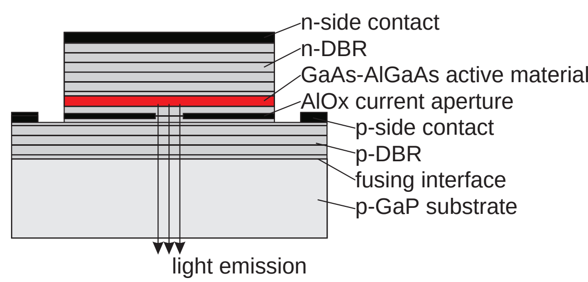

Fig. 1. Cross section of a wafer-fused transparent-substrate 850 nm VCSEL.

As depicted in Fig. 1 the p-side contacts are evaporated on the p-type GaAs layers rather than on the p-GaP substrate although this would allow more homogeneous carrier injection. Investigations of different metallizations on GaP have shown that it is hardly possible to achieve ohmic contacts with low resistances on GaP at $p = 1 \cdot 10^{18}\,\mathrm{cm}^{-3}$ using Zn doping.

3. Performance

Fig. 2 shows the output characteristics of a wafer-fused 850 nm-VCSEL in CW operation at room temperature. A threshold current of 20 mA, a threshold voltage of 2 V and a maximum wall-plug efficiency of 12 % is observed at an active diameter of 28 μm. These results are superior to those published in [3] with respect to the threshold current density as well as to the threshold voltage.

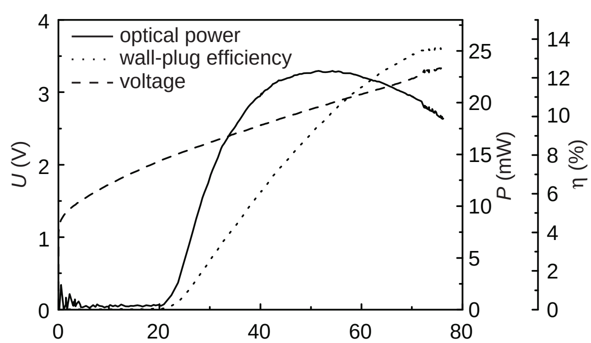

Fig. 2. Room temperature CW characteristics of a wafer-fused transparent-substrate 850 nm VCSEL with 28 μm active diameter.

The threshold current of the fused devices rises by a factor of 3 compared to unfused VCSELs made out of the same epitaxial material. Apart from thermal and mechanical stress that may lead to suffering optical properties of the material the changing mirror reflectivities due to different refractive indices have to be considered. The p-DBR of the unfused VCSEL terminates with a GaAs-air interface which gives an additional benefit in mirror reflectivity. By fusing the topmost p-GaAs layer to the GaP substrate this benefit is eliminated resulting in rising threshold current. This drawback has been counterbalanced by adding a few mirror pairs to the p-DBR.

4. Conclusion

Very successful transparent-substrate bottom emitting VCSELs with an emission wavelength of 850 nm have been demonstrated by using wafer-fusion to add transparent GaP substrate to conventional GaAs vertical cavity lasers. A slight rise of the threshold current is mainly caused by a decrease in the p-DBR reflectivity due to adding the GaP material. The considerably large devices having an active diameter of 28 μm operate under room temperature CW conditions at reasonable threshold currents and voltages of 20 mA and 2 V, respectively.

References

[1] N.M. Margalit, J. Piprek, S. Zhang, D.I. Babic, K. Streubel, R.P. Mirin, J.R. Wesselmann, and J.E Bowers, "64 °C continuous-wave operation of 1.5 μm vertical-cavity laser", *IEEE J. Sel. Top. Quant. El.*, vol. 3, pp. 359–365, 1997.

[2] F.A. Kish, D.A. Vanderwater, D.C. DeFevere, D.A. Steigerwald, G.E. Hofler, K.G. Park, and F.M. Steranka, "Highly reliable and efficient semiconductor wafer-bonded AlGaInP/GaP light-emitting diodes", *El. Lett.*, vol. 32, pp. 132–134, 1996.

[3] K.D. Choquette, K.M. Geib, B. Roberds, H.Q. Hou, R.D. Twesten, and B.E. Hammons, "Short wavelength bottom-emitting vertical cavity lasers fabricated using wafer-bonding", *El. Lett.*, vol. 34, pp. 1404–1405, 1998.

High-Power Semiconductor Laser Amplifier for Free-Space Communication Systems

G. Jost

High-power semiconductor laser amplifiers are interesting devices for new key technologies. They promise high optical output power up to several watts and good beam quality in combination with different master oscillators. A new free-space data transmission system shows the excellent properties of our tapered semiconductor amplifiers with a VCSEL master oscillator for an optical output power up to 380 mW at 2.5 Gb/s with BER below 10^{-11}.

1. Introduction

Traveling-wave semiconductor amplifiers are compact devices with high wall-plug efficiency and a large spectral amplification range. In view of these points, they are of growing importance in future key technologies as fundamental elements for optical free-space communication systems. Especially, the development of tapered amplifier with high signal gain and an optical output power of several watts, preserving the optical beam quality of a single-mode masteroscillator with a few mW optical power, has raised a lot of interest due to the emergence of various applications like optical intersatellite communication or indoor optical wireless IR LAN systems. In section 2. we demonstrate the fundamental properties of a linear tapered semiconductor laser amplifier like optical output power, signal gain and wall-plug efficiency. Chapter 3. shows a new application and interesting combination of a vertical-cavity surface emitting laser (VCSEL) as master oscillator and an edge-emitting power amplifier (VCSEL-MOPA). Now a days, VCSEL are very promising devices for short distance, high-speed optical data link applications. They are low cost devices with some excellent electrical and optical properties like low threshold current allowing bias-free modulation [1] and a modulation bandwidth up to 21.5 GHz [2], but they are limited in their optical output power to a few mW. With our new data transmission system consisting of a VCSEL master oscillator and an edge-emitting power amplifier we are able to combine a high-speed, low cost and easy-to-modulate semiconductor device with a high power, high efficiency amplifier. This system allows data transmission experiments at 2.5 Gb/s with bit error rates below 10^{-11} and an optical power up to 380 mW.

2. Tapered Amplifier Structure and fundamental Characteristics

The layer sequence of the tapered semiconductor amplifier has been grown by molecular beam epitaxy (MBE). The active region consists of a 8 nm compressively strained InGaAs quantum well, sandwiched between graded-index AlGaAs layers (GRINSCH). With this structure we achieve an internal efficiency of 92 % and an intrinsic loss of 1.9 cm^{-1}. The length of our devices is 2040 μm with an input aperture of 7 μm for taper angles of 4° and 5°. For taper angles of 7° and 10° we prefer a width of 5 μm as input aperture to overlap the assuming profile of a free-space intrasystem propagating gaussian beam . The principle layer structure of such a device is depicted in Fig. 1. The device is mounted junction-side

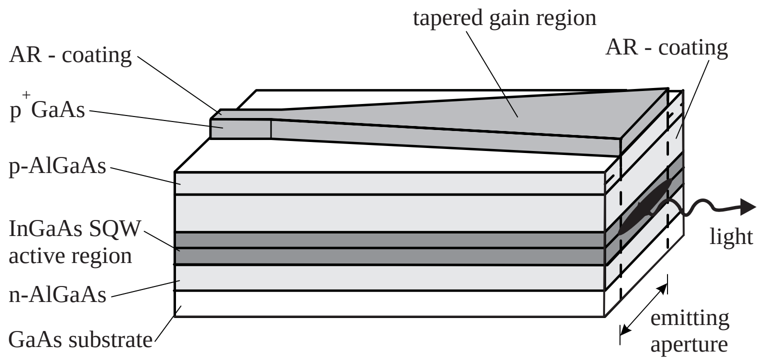

Fig. 1. Schematic drawing of a tapered semiconductor amplifier with a length of 2040 mum and a taper angle of 5°.

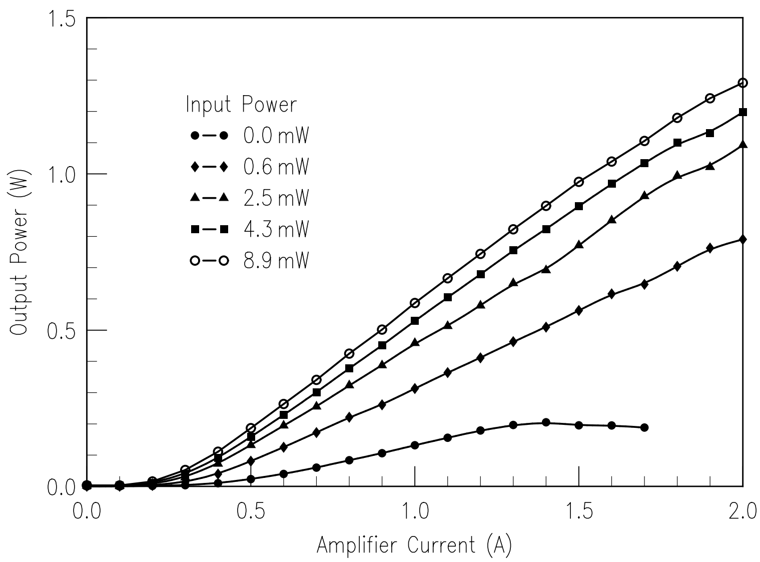

Fig. 2. Output characteristic of a tapered amplifier for different input powers up to a amplifier current of 2 A. The maximum output power is 1.3 W at 8.9 mW input power. The maximum slope efficiency is 0.83 W/A.

down on a diamond heat spreader with AuSn solder to obtain a low thermal resistance, good adhesion low thermal stress. Necessarily conditions for high power devices to achieve maximum optical output powers without thermal roll-over. Another important supposition for laser amplifiers is the suppression of self oscillation due to reflections at the cleaved laser facets. Therefore both facets are coated with an high-quality multi-layer antireflection coating. The reflectivity of the coating is less than 10^{-4} over a bandwidth of 70 nm. With such laminated facets we obtain an increase of the original laser threshold and only spontaneous emission or amplified spontaneous emission for currents up to 2 A. The high undulation-free gain of such an amplifier allows a variation of the masteroscillator wavelength of 16.5 nm FWHM. To characterize the high power, tapered amplifier we use a single-mode edge-emitting laser diode. The maximum input power available from this single-mode device is 9 mW at 936 nm which is adjusted to the maximum signal gain of the amplifier by variation of the master oscillator heat sink temperature. Fig. 2 shows the output power for a device with a taper angle of 5° and a current up to 2.0 A versus the amplifier current. With an input power of 8.9 mW we obtain an output power of about

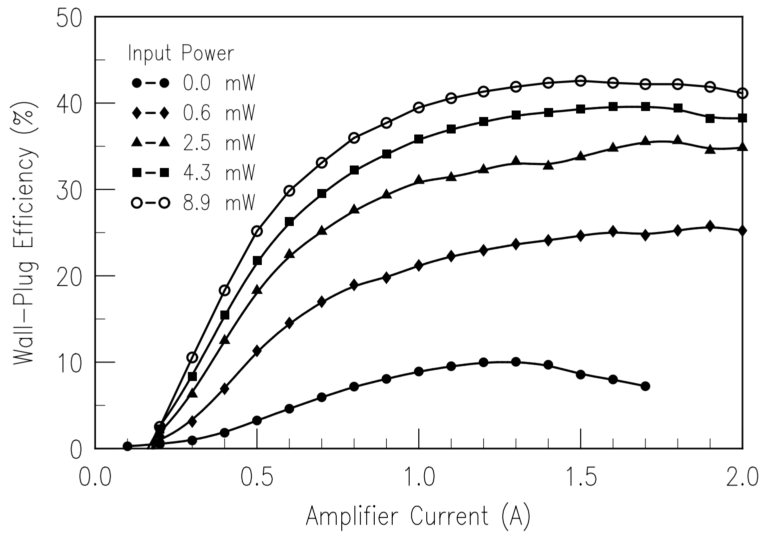

Fig. 3. Wall-plug efficiency versus the amplifier current for different input power. The maximum wall-plug efficiency is 43 % at a current of 1.5 A. Also for an optical output power of 1.3 W at a current of 2 A and an input power of 8.9 mW, the wall-plug efficiency is about 39 %

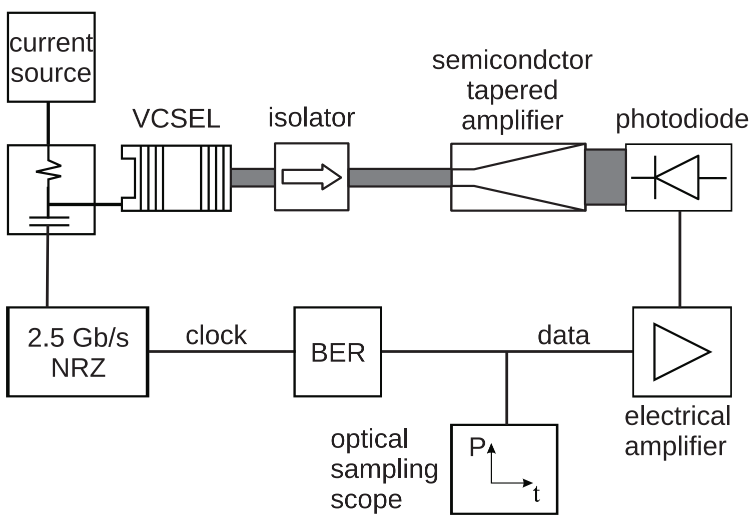

Fig. 4. Setup of the data transmission experiment.

1.3 W which corresponds to a signal gain of 21.6 dB. The almost linearly output characteristic promises a further increase of the optical output power, if we increase the amplifier current. Fig. 2 demonstrates also that an increase of the input power up to 8.9 mW results in an increase of the slope efficiency up to 0.83 W/A for a totally saturated amplifier. With this tapered semiconductor amplifier and an input power of 8.9 mW from a single-mode edge-emitting laser diode we obtain a wall-plug efficiency of 43% at an current of 1.5 A as shown in Fig. 3. Almost at the maximum output power of 1.3 W the wall-plug efficiency is more than 39 %. With decreasing input power the wall-plug efficiency also decreases but still at an input power of 2.5 mW we achieve a wall-plug efficiency of 35 % and an optical output power of 1 W. corresponding to a signal gain of 26 dB. Without optical input power the laser amplifier emits only spontaneous emission and the wall-plug efficiency is limited at about 10 %. The high signal gain

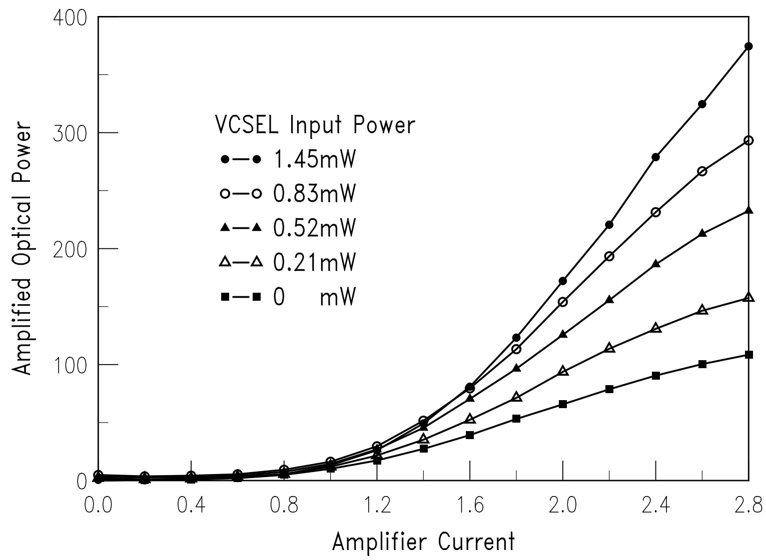

Fig. 5. Output characteristic of the VCSEL-MOPA. The maximum output power is 380 mW at an amplifier current of 2.8 A and a optical VCSEL input power of 1.45 mW.

and also small dimension of tapered semiconductor amplifiers as well as the high wall-plug efficiency at low optical input powers are properties which allows the combination with low power devices like VCSEL. Such a system makes clear that hybrid integrated devices which separately optimized devices for each application offers a lot of new prospects in future key technologies.

3. Tapered amplifier with VCSEL as masteroscillator for high-power high-speed data transmission

For the data transmission experiment, we use an amplifier with an taper angle of 10° and an input aperture of 5 μm. The length of the device is 2040 μm. In contrast to other transmission systems, we replaced the edge-emitting single-mode laser diode by a low cost, bottom emitting VCSEL as shown in Fig 4. Such a device has the potential to be mounted on silicon integrated circuits using flip-chip technology [3]. The optical output power of the VCSEL with an aperture of 5 μm is 5 mW at a current of 9 mA. The VCSEL is exhibiting single-mode emission at 943 nm up to a current of 3.4 mA and an optical output power of 0.95 mW. The optical output of the VCSEL is directly coupled into a tapered InGaAs/AlGaAs semiconductor amplifier separated by a 30 dB optical isolator. Fig. 5 shows the output characteristic of the VCSEL-MOPA for amplifier currents up to 2.8 A and an optical VCSEL power up to 1.45 mW. The maximum output power of the system is 380 mW corresponding to an amplifier gain of 24 dB. Modulation experiments with the combined system at various VCSEL and amplifier currents show no significant influence of the optical amplifier on the small-signal modulation response up to 10 GHz. Data transmission experiments have been performed at a VCSEL bias current of 3.4 mA and a data rate of 2.5 Gb/s. With a semiconductor amplifier current of 2.0 A we achieve an optical output power of 165 mW. The amplified signal is passed through an attenuator with an attenuation of about 45 dB to avoid a destruction of the photodiode. The transmitted bit sequence is monitored with an electrical sampling oscilloscope and analyzed with a bit error detector. Fig. 6 shows the eye diagram for 2.5 Gb/s PRBS transmission with a word length of $2^7 - 1$ at a BER of 10^{-11}. The eye opening is about 0.4 V having

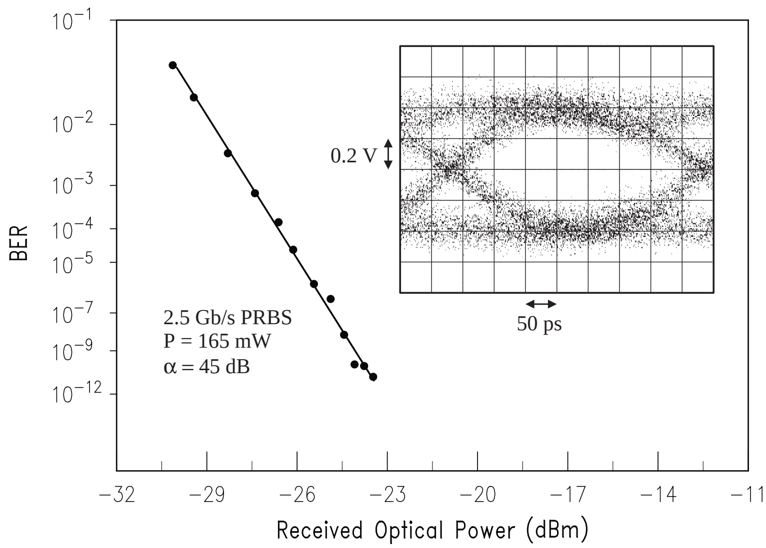

Fig. 6. BER at 2.5 Gb/s versus received optical power after 45 dB attenuation and eye diagram corresponding to a BER of 10^{-11} at a received optical power of -23 dBm.

a symmetric shape and without relaxation oscillation. Data transmission with a BER below 10^{-11} is possible down to a received optical power of -23 dBm. Also for a VCSEL current of 5 mA and an optical output power of the amplifier of 380 mW, BERs of less than 10^{-11} are possible.

References

[1] P. Schnitzer, R. Jäger, C. Jung, R. Michalzik, D. Wiedenmann, F. Mederer, K.J. Ebeling, IEEE Photon. Technol. Lett., in press, Dec. 1998

[2] K.L Lear, V.M. Hietala, H.Q. Hou, M. Ochiai, J.J. Banas, B.E. Hammons, J.C. Zolper, S.P. Kiloyne, OSA Trends in Optics and Photonics **15**, 69-74 (1997).

[3] R. King, R. Michalzik, C. Jung, M. Grabherr, F. Eberhard, R. Jäger, P. Schnitzer, K.J. Ebeling, in Vertical-Cavity Surface-Emitting Lasers II, SPIE Proc. **3286**, 64-71 (1998).

64 Channel Flip-Chip Mounted Selectively Oxidized GaAs VCSEL Array

Roland Jäger and Christian Jung

We have designed and fabricated a 64 channel optical module using a self-alignment flip-chip packaging technique for two-dimensional (2D) GaAs epitaxial-side emitting vertical-cavity surface-emitting laser (VCSEL) array mounting without substrate removal on Si subcarrier. Light emission is obtained through a wet-chemically etched window in the Si subcarrier. The 2D independently addressable selectively oxidized GaAs laser array is arranged in an 8×8 matrix with a device pitch of 250 μm and each laser is supplied with two individual top contacts. This metallization scheme allows flip-chip mounting junction-side down on Si subcarrier. The VCSEL array chip is placed above the window in the Si subcarrier and is assembled using a self-aligned bonding technique with PbSn solder bumps. Arrays with 4 μm active diameter exhibiting threshold currents of less than 1.1 mA and single-mode output powers of 2 mW. Driving characteristics of the lasers in the array are fully compatible to advanced 3.3 V CMOS technology.

1. Introduction

VCSELs are promising devices for use in optical data links for parallel transmission and network computing. The inherent possibility for realizing 2D arrays as well as high-speed modulation and data generation make VCSELs the transmitters of choice for parallel optical interconnects. Due to high wall-plug efficiency operation at low driving currents, VCSELs can reduce thermal heating when using optical interconnections combined with high speed ICs in optical transceiver modules. Optical transmitter and receiver modules require reliable packaging technologies for interfacing CMOS chips and optical fibers. Shorter assembly times and simpler schemes for automatic manufacturing can be obtained using self-alignment techniques, especially for parallel interconnects with their high number of coupled elements. The wavelength of existing modules with two-dimensional bottom-emitting VCSEL arrays is due to the absorption of GaAs Substrate usually 980 nm. However, 850 nm is the preferred emission wavelength owing to inexpensive Si or GaAs photodetectors. Up to now, there are not too many approaches for the fabrication of low cost GaAs top-emitting VCSEL transmitters using flip-chip packaging and direct coupling into a two-dimensional fiber matrix. In this paper we report on the fabrication of 8×8 element 850 nm wavelength VCSEL array modules mounted directly on Si subcarrier, offering 64 independently addressable channels for short-distance data transmission.

2. VCSEL array design and fabrication

Fig. 1 shows a schematic of an individual selectively oxidized top-emitting GaAs VCSEL of the array. The layers are grown by solid source molecular beam epitaxy. The active region consists of three 8 nm thick GaAs quantum wells embedded in $Al_{0.2}Ga_{0.8}As$ barriers for 850 nm emission wavelength. The lower n-type Si-doped and the upper p-type C-doped Bragg reflectors consist of 38 and 27 $Al_{0.2}Ga_{0.8}As$-$Al_{0.9}Ga_{0.1}As$ quarter wavelength layer pairs, respectively. Lateral current confinement is achieved by

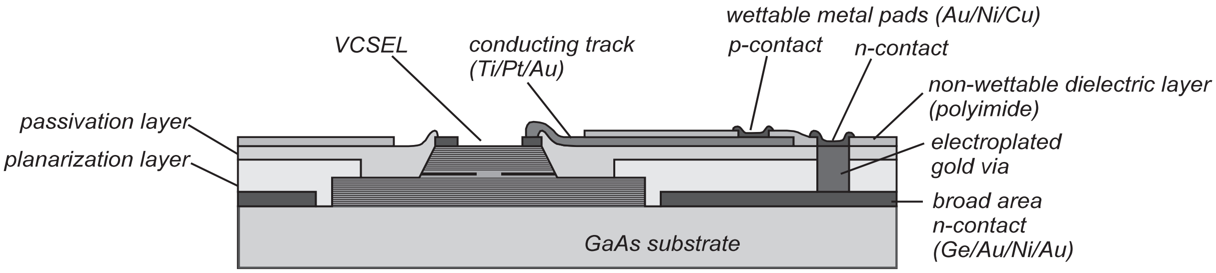

Fig. 1. Cross-sectional view of an individual top-emitting GaAs VCSEL of an array with corresponding contact scheme. All electrical contacts are located on the top-side of the array. A non-wettable dielectric layer and the wettable metal pads are necessary for the flip-chip bonding process.

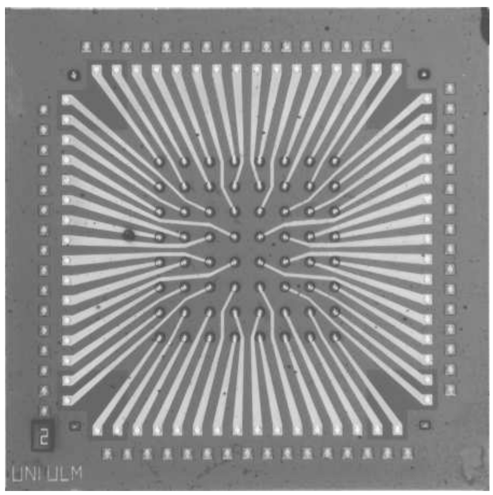

Fig. 2. Photograph of a top-emitting 8×8 independently addressable VCSEL array with 250 μm device pitch and two individual contacts per device.

selective wet oxidation of a 30 nm thick AlAs layer after wet-chemical mesa etching. A Ti/Pt/Au ring contact is deposited on the top of the mesa to form the n-contact. On the top-side of the wafer chemically assisted ion-beam etching is used to define a second larger mesa that provides access to the n-doped GaAs substrate. A Ge/Au/Ni/Au broad area common n-contact is evaporated and both contacts are annealed at 410 °C. After planarization and passivation of the mesa with two different types of photosensitive polyimides, the n-contact is brought to the surface by an electroplated gold via in the polyimide, as shown in Fig. 1. A non-wettable dielectric layer using polyimide in combination with a wettable metal pad serves to restrict the solder flow during the subsequent flip-chip bonding process. Mechanically polishing the GaAs substrate down to 150 μm and cleaving the sample into individual laser arrays of 5×5 mm^2 size are the final processing steps.

Fig. 2 shows a photograph of the top-emitting 8×8 GaAs VCSEL array with two individual contacts per lasing element. In the center the laser matrix with 250 μm device pitch is seen. The p-contact is taken to the outside by long conducting tracks. The bond pads for the common n-contact are located next to the p-contact bond pads. As the wettable metal pads define the position of the opto chip with respect to the silicon carrier, proper alignment is necessary. The Si subcarrier is fabricated from two-side polished 300 μm thick Boron doped (100)-oriented Si substrates. A square shaped window is etched by selective chemical anisotropic etching in KOH:H_2O solution at 70 °C. A 300 nm thick Si_3N_4 layer deposited by plasma enhanced chemical vapor deposition serves as an etch mask. The etch rate of (100) Si in the KOH solution is typically about 33 μm/h. The layout of the feeding lines on the Si subcarrier is designed for flip-chip packaging of the VCSEL array and has been worked out based on the geometrical dimensions and positions of the alignment marks and emission window in the Si subcarrier. The surface of the Si subcarrier is passivated with a thin polyimide layer to prevent leakage currents into the subcarrier. The conducting Ti/Pt/Au tracks are arranged around the opening. A non-wettable dielectric layer (polyimide) is deposited to prevent the solder from flowing along the tracks during reflow and flip-chip bonding processes. For the wettable metal pads a Au/Ni/Cu metallurgy is used, where Ni serves as diffusion barrier for Sn used in the flip-chip bonding process. The diffusion barrier must be robust enough to be utilized with the high Sn content of the eutectic 63Sn/37Pb solder. The final Cu metallization deposited by electroplating is wettable by the solder. The VCSEL array needs to be arranged accurately relative to the emission window in the Si subcarrier which is achieved by self-aligned flip-chip bonding. As solder material we use eutectic Sn/Pb which is electroplated on the Si subcarrier. This material allows reflow temperatures of less than 250 °C and a precise alignment is obtained by exploiting the surface tension of the solder bumps. The reflow and bond processes take place in an atmosphere of nitrogen and formic acid vapor (HCOOH) to protect the Cu metallization and the solder material (Sn/Pb) from oxidation and to promote solder wetting. For the flip-chip process we have developed and built a self-alignment mounting machine which allows active adjustment of VCSEL array and Si subcarrier. The laser array is placed between the four alignment marks on the Si subcarrier using a stereo microscope. To increase the alignment accuracy and ensure that the laser array is positioned properly to the Si subcarrier transmission monitoring is used. When the VCSEL array is adjusted to the subcarrier with tolerances of better than 20 μm the bond process is started. The temperature in the solder chamber is slowly raised to 180 °C and after a few seconds abruptly increased to 250 °C. The molten solder starts wetting the metal pads and thereby adjusts the position of the laser chip in effort to minimize the surface area to reaching the lowest total energy of the assembly. In the process, nitrogen and formic acid vapor are used as flux to support efficient wetting and self-alignment. At the final position the chip is stably fixed by rapidly cooling the solder joint with nitrogen gas. The alignment accuracy is about ±10 μm.

3. Continuous Wave Emission Characteristics of the Module

The performance of VCSEL arrays after packaging on the Si subcarrier has been investigated in detail. Output characteristics of an individual laser of the array are depicted in Fig. 3. Threshold current and voltage are 0.7 mA and 2.2 V, respectively. Threshold current remains rather unchanged after the bonding process but a considerable increase of the voltage is observed which might be caused by a series Schottky diode in the not yet optimized solder contact. The maximum optical output power is 2.7 mW and the wallplug efficiency of 20 % is limited by the high voltage drop at the solder contacts. Fig. 4 shows the emission spectra of the individual VCSEL for different driving currents. The laser oscillates on the fundamental transverse mode with a side mode suppression ratio of 30 dB up to a current of 2.5 mA. Threshold current and emission wavelength distributions of the 8×8 VCSEL array after flip-chip mounting on Si subcarrier are depicted in Fig. 5 and 6, respectively. The threshold currents of the lasers within the array remain nearly unchanged varying between 0.7 and 1.1 mA. The emission wavelengths measured at $1.5\cdot I_{th}$ show a shift of 17 nm across the array in accordance with the unmounted array. Basically, we observe no substantial change in the optical emission characteristics before and after

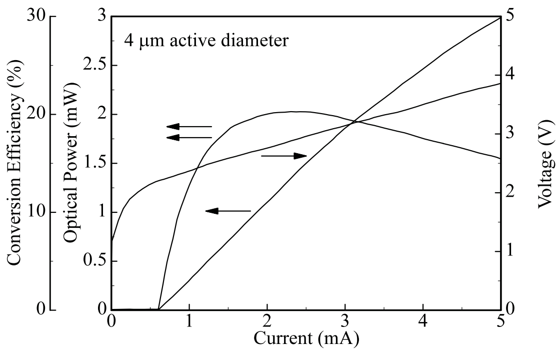

Fig. 3. Optical and electrical characteristics of a typical VCSEL with 4 μm diameter oxide aperture of the flip-chip bonded 8×8 array. Threshold current and maximum conversion efficiency are 0.7 mA and 20 %, respectively.

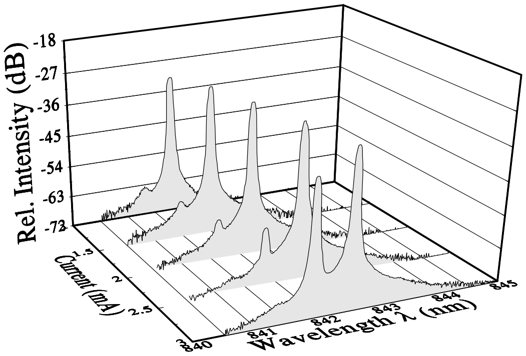

Fig. 4. Emission spectrum of a mounted VCSEL with a current aperture of 4 μm. The laser oscillates at a wavelength of 842 nm on the fundamental transverse mode showing single-mode operation up to a current of 2.5 mA.

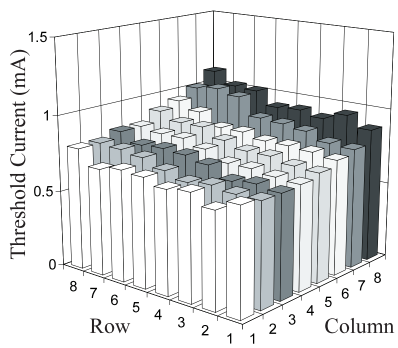

Fig. 5. Threshold current distribution of a mounted 8×8 VCSEL array. All threshold currents remain below 1.1 mA.

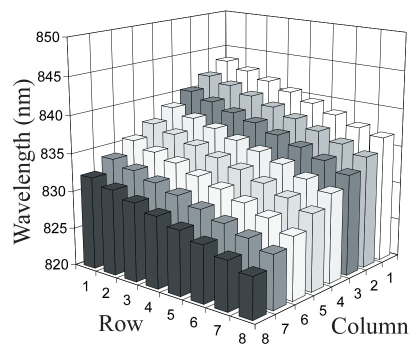

Fig. 6. Two-dimensional wavelength distribution of a mounted 8×8 VCSEL array at a driving current of 1.5$\cdot$ I_{th}. The total wavelength shift across the array is 17 nm.

packaging of the VCSEL array. The higher voltage drop at threshold can be explained by non-ohmic behavior of the not optimized n-type solder contact pad.

4. Conclusion

In summary, we have fabricated 850 nm wavelength 2D VCSEL arrays flip-chip bonded on Si subcarriers which are ideally suited for transmitters in optical fiber modules or free-space indoor communications. Self-alignment techniques are used to realize flexible independent addressing of 8×8 arrays. Measurements of top-surface contacted, top-surface emitting vertical cavity lasers in the module show single-mode output powers as high as 2 mW, threshold currents below 1.1 mA, and 20 % conversion efficiencies after mounting resulting in more than 100 mW total array output power. All devices within the array are fully compatible with advanced 3.3 V CMOS technology.

$SiBr_4$ doped GaInP/AlInGaP Quantum Wells: Influence of structure and growth conditions.

Matthias Golling, Georgi Stareev, Hin Yiu A. Chung and Jürgen Mähnß

The quantum well structure of red emitting InGaP/AlInGaP laser diodes is investigated by photoluminescence spectroscopy. Growth parameters are optimized for high photoluminescence yield. Different doping schemes are tested for electrical property improvement. It is shown that $SiBr_4$ doping of conventional laser structures gives similar results compared to solid source Silicon doping.

1. Introduction

Laser diodes emitting in the red visible range are of great interest for many applications like data storage (DVD), data transmission on short distances or laser printers. For the improvement of laser characteristics, the effect of different structures o n the optical properties are evaluated. To avoid influences of electrical effects, samples are measured with photoluminescence spectroscopy (PL) on undoped samples.

Electroluminescence is obtained in Beryllium and Silicontetrabromide doped samples. For comparison, conventional InGaAs/GaAs edge emitting laser diodes doped with $SiBr_4$ are processed.

2. Structure of samples

The basic structure of the MQW samples is shown in Fig. 1. On exact cut GaAs substrate, the quan-

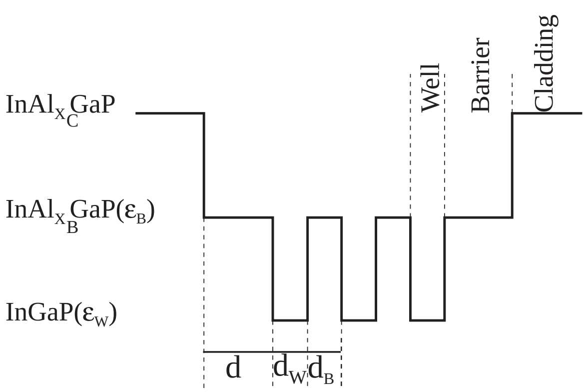

Fig. 1. Basic structure of MQW samples

tum well structure is embedded between cladding layers of (AlGa)InP with various Aluminum content X_C. The quantum well structure itself consists of three compressively strained GaInP quantum wells, separated by lattice matched GaInP barriers. The Indium content of the quantum wells X_B is a valuable indicator for the quantum well strain.

3. Characterization

The influence of quantum well thickness on PL properties is investigated with GaInP cladding layers. For clarification, the active region of the device structure is depicted in the inset of Fig. 2. As expected, the intensity of the PL signal is strongly increasing with thicker quantum wells. For a quantum well thickness of 6 nm, a high intensity of the PL signal is achieved. Another important parameter is the quantum well material composition. In Fig. 3, the influence of the Indium content on PL intensity in 6 nm quantum wells is shown. In the case of bulk GaInP, where strain of the material and depth of the wells equal zero, (the indium content X_B is 49 %), the PL intensity is found to be weak. With an increase of indium content to 67 % the intensity rises by a factor of 50. This effect is accompanied by a red shift of the emission wavelength from 660 nm to 738 nm. Both effects are expected from the band diagram. The increased Indium content enlarges band offsets resulting into higher levels of excited states and better carrier confinement.

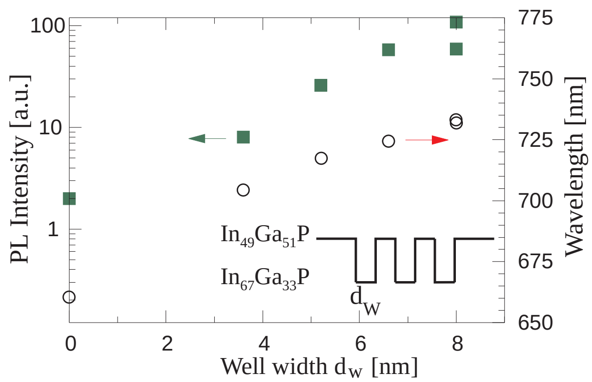

Fig. 2. Influence of quantum well thickness on PL intensity

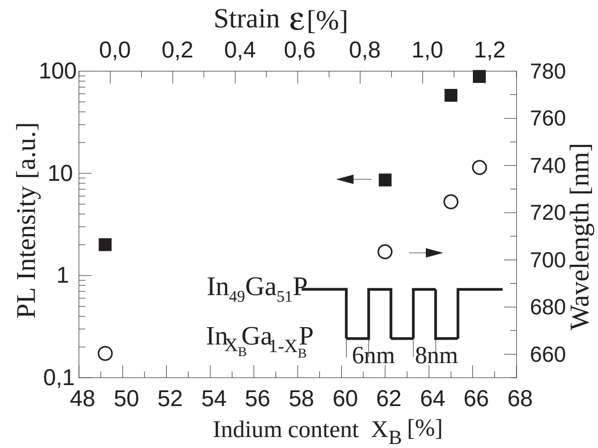

Fig. 3. Influence of quantum well depth on PL intensity

Further increase of carrier confinement is achieved by embedding the active zone into high bandgap $Al_{X_C}Ga_{0.51-X_C}In_{0.49}P$ cladding layers. The influence of aluminum content on photoluminescence intensity is shown in Fig. 4. Compared to the quantum well structure without aluminum containing

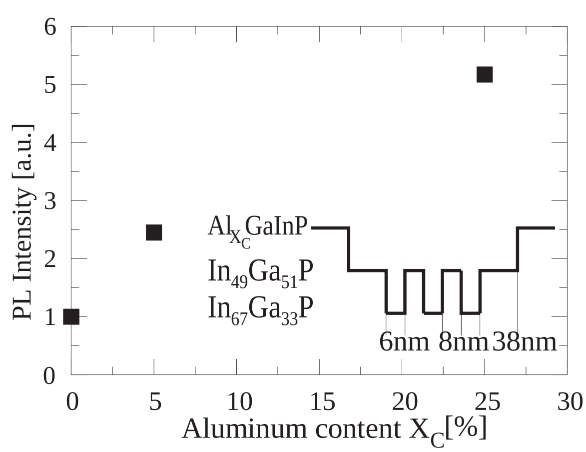

Fig. 4. Dependence of Aluminum content X_C in cladding layers. Carrier confinement is improved with increased Aluminum content resulting into higher PL levels.

cladding layers, an aluminum content of 5 % gives an increase of intensity by a factor of 2.5. With an aluminum content X_C of 25 %, a further increase by a factor of two can be observed. Higher aluminum contents are expected to have little effect to PL intensity due to switching to indirect bandgap. Indirect $Al_{X_C}Ga_{0.51-X_C}In_{0.49}P$ exhibits a decrease of carrier mobility and carrier dynamics [1], resulting into poor electrical characteristics.

4. Doping of $Al_XGa_{0.51-X}In_{0.49}P$

Carrier transport to the active zone must be optimized to achieve sufficient conductivity for electroluminescence. If the concentration of free carriers is too low, the resistance of the device is high, resulting in high thermal stress, whereas a high do ping concentration leads to reabsorption of photons.

For p and n doping, solid source Beryllium (Be) and Silicon (Si) are used, respectively. Both are well-established dopants for III/V-MBE. Carbontetrabromide (CBr_4) has proven to be a reliable p doping source in the AlGaAs System. One big advantage of Carbon is the small diffusion coefficient, allowing sharper doping profiles than Be. For n doping of III/V-Semiconductors, solid silicon is known to be a reliable source causing no trouble in general. However, temperature of the Silicon cell is relatively high. For GaAs and, a temperature around 1000 $^\circ C$ is necessary to achieve a carrier concentration of 1×10^{18} cm^{-3}. In AlGaInP, Silicon cell temperature has to be chosen approximately 100 $^\circ C$ higher for the same doping level. At this high temperature molecules reevaporate from the surrounding of the cell, possibly leading to nega tive effects. A solution to this problem might be the gaseous silicon precursor Silicontetrabromide ($SiBr_4$). At 315 K, $SiBr_4$ is a solid with vapor pressure of 23.3 mbar. It is chemically similar to the p doping source CBr_4 already used for the AlGaAs system. Usage of the gaseous Si doping source is found to be not critical. In GaAs, doping concentration of $4 \times 10^{18}cm^{-3}$ could be easily achieved, as shown in Fig. 5. The equivalent beam pressure is measured to control the dopant flux. At a carrier concentration of $1.6 \times 10^{18}cm^{-3}$, a mobility of 2000 cm^2/Vs is obtained,

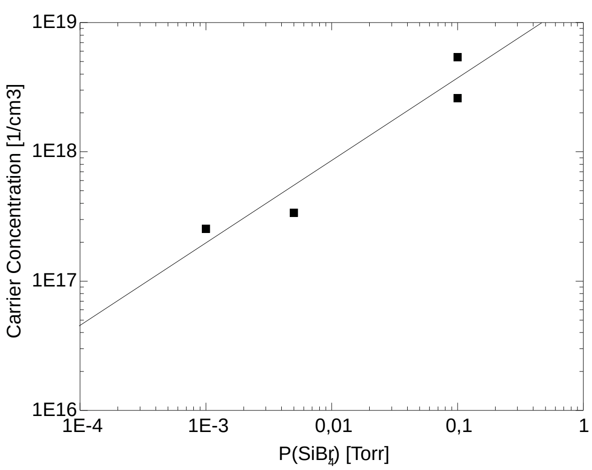

Fig. 5. $SiBr_4$ as n doping source for GaAs

indicating a good material quality. It is known that n doping creates deep levels in AlGaInP [2], but even in this case $SiBr_4$ can be used successfully. To prove the ability of both gaseous dopants, conventional InGaAs/GaAs edge emitting lasers have been grown with a non optimized layer structure. The threshold current density of the broad area laser diodes was slightly above 1 kA/cm^2, which clearly proves that both p an n dopant are working quite well.

5. Summary

Quantum well structures in the AlGaP/AlInGaP material system have been characterized using photoluminescence spectroscopy. Optical parameters were improved by variation of dimensions of the quantum well structure. A new dopant precursor, Silicontetrabromide, is installed and characterized to improve the electrical properties. The doping ability is shown by the growth of conventional InGaAs/GaAs laser diodes.

References

[1] C.S. Menoni, O. Buccafusca, M.C. Marconi, D. Patel, J.J. Rocca, G.Y. Robinson, and S.M. Goodnick, Effect of indirect $\Gamma - L$ and $\Gamma - X$ transfer on the carrier dynamics of InGaP/InAlP multiple quantum wells, *Appl. Phys. Lett.*, vol. 70, pp. 102–104, 1997.

[2] S. Nojima, H. Tanaka, and H. Asahi, Deep electron trapping center in Si-doped InGaAlP grown by molecular-beam epitaxy, *J. Appl. Phys.*, vol. 59, pp. 3489–3494, 1986.

[3] D.J. Friedmann, A.E. Kibbler, and R. Reedy, Selection of substrate orientation and phosphorus flux to achieve p-type carbon doping of $Ga_{0.5}In_{0.5}P$ by molecular beam epitaxy, *Appl. Phys. Lett.*, vol. 71, pp. 1095–1097, 1997.

Homoepitaxial growth of GaN by MOVPE: A new benchmark for GaN technology

Christoph Kirchner

Using low pressure Metal Organic Vapor Phase Epitaxy (MOVPE) for homoepitaxy, GaN layers were grown on GaN bulk single crystal substrates. The layers show world record optical properties with photoluminescence (PL) linewidths as narrow as 0.11 meV at 4.2 K for the (D^0,X) transition. The free excitonic transitions FE_A, FE_B, their excited states and the FE_C transition could be clearly resolved at 4.2 K.

1. Introduction

The III-V Nitride semiconductor alloys (InAlGaN) have attracted a great deal of interest due to their potential for fabrication of light-emitting devices (LEDs) operating in a wide emission wavelength range, from the red to ultraviolet. Intensive research on III-V Nitrides has paved the way to commercially available high-power blue and green LEDs [1]. These LEDs are key components for the fabrication of full colour displays with high luminous intensities. Blue emitting laser diodes with InGaN multi quantum-well structures as active layers are steadily improved and now have lifetimes above 10000 hours at room temperature under continuous wave (cw) operation using laterally epitaxially overgrown (ELOG) substrates [2], [3]. Despite this progress, the GaN technology still suffers from mismatched heteroepitaxial growth on sapphire or SiC substrates. Heteroepitaxy results in 14 % and 3.5 % lattice mismatch for GaN growth on sapphire and 6H SiC, respectively, causing high dislocation densities of 10^9 to 10^{10} per cm^2. This can only be avoided by substrates having closely matched lattice constants and thermal expansion coefficients to the layers. Under ideal circumstances, i. e. homoepitaxy, high quality layers can be grown 2 - dimensionally without formation of dislocations. Of the available alternative substrate materials, only LiGaO reveals good lattice matching to GaN, but thermal stability is crucial at high temperatures required for GaN growth [4]. All heteroepitaxial growth processes require nucleation layers deposited at low temperatures prior to growth of the main layers to increase crystal quality of the epitaxial layers. These two-step processes are complex and difficult to optimize. Reproducibility remains a problem due to the fact that small variations in parameters during deposition of the nucleation layers cause large changes in main epitaxial GaN layer quality. Thus, direct growth on GaN substrates is clearly the first choice: no lattice mismatch, identical thermal expansion coefficients, resulting in excellent optical and crystal quality of the GaN layers. However, GaN cannot be pulled from a melt like GaAs or InP due to the extremely high temperature and pressure required. The GaN bulk single crystal substrates used for these experiments have been produced from atomic nitrogen dissolved in gallium melts under high nitrogen pressure and high temperatures at the High Pressure Research Center of the Polish Academy of Sciences (Unipress, Warsaw, Poland) [5]. This process leads to GaN platelets with areas of around 100 mm^2 with [0001] orientation. Alternatively, GaN quasi substrates can be fabricated by a HVPE process (hydride vapor phase epitaxy). The high growth rates up to 80 μm/hr on sapphire substrates using ammonia and GaCl enable the growth of very thick layers which can be used as substrates. The epitaxial layer quality achieved with this type of substrates is not as high as with the above mentioned single crystal substrates, because HVPE GaN is deposited on sapphire, too. Due to the large thickness of a few hundred microns, dislocation density is reduced, but still in the range of 10^7 per cm^2. Using ELOG technologies, dislocation density can be further reduced. One major advantage of the HVPE process is the possibility to fabricate 2 inch GaN wafers, enabling commercial production of GaN based devices. The GaN bulk single crystals cannot be fabricated in such sizes at the moment, but provide the highest quality substrates available.

2. Experimental

Epitaxial growth of GaN is performed in a horizontal, radio-frequency heated, water cooled quartz MOVPE reactor (AIXTRON AIX 200 RF), operated at low pressure. Substrate material are GaN crystals with sizes of about 8x8 mm^2. Trimethylgallium (TMGa) and ammonia (6.0 purity with additional purifier) are used as group III and group V precursors, respectively. Hydrogen is used as carrier gas. Prior to growth, one half of the substrate is covered with photoresist and then etched with CAIBE using a Cl_2 - Ar process, resulting in an etch depth of around 300 nm. More details about the CAIBE treatment are described in [6]. This partial etching allows direct comparison of the epitaxial layer quality grown on etched and non-etched parts of the same substrate. After stripping the photoresist, the substrates are cleaned in organic solvents and deionized water. To improve thermal coupling of the substrates to the susceptor, the backside of the substrates is metallized. Simultaneous growth on up to three GaN bulk single crystal pieces in one run allows to compare growth behaviour, morphologies and crystal quality of epitaxial layers.

Due to the different shape and size of each substrate piece, thermal coupling of each substrate to the susceptor is different, causing problems in composition reproducibility of InGaN and AlGaN layers. The high gas flow through the reactor during growth tends to lift and remove the lightweight substrate pieces from the susceptor, therefore they have to be fixed with small sapphire pieces. Indium-bonding, a method widely used in MBE technology, could not be applied successfully. Most of the Indium is evaporated due to the high growth temperature, and the rest is partially converted to Indium nitride, which made it impossible to remove the substrates from the susceptor. After loading into the reactor, substrates are heated up to 1030 °C under a steady flow of an ammonia / hydrogen mixture for 10 minutes. Following this annealing step, undoped GaN is grown to a thickness of 1.5 μm. During growth, the reactor temperature is kept at 1030 °C, while reactor pressure is 250 mbar. The ammonia and the TMGa flow are 2.5 standard liters per minute and 27 μmol/min, respectively.

3. Results and Discussion

Regarding the surfaces of the overgrown GaN crystals, there are strong differences in morphologies between the previously dry-etched region and the not CAIBE-treated area. The CAIBE-etched area of the sample reveals an improved surface morphology with almost no visible scratches, trenches, or holes. With a high resolution photoluminescence-setup (PL), low temperature (4.2 K) PL measurements were performed at the Department of Semiconductor Physics at University of Ulm (K. Kornitzer, K. Thonke and R. Sauer). A HeCd laser (λ=325 nm) was used as the excitation source with a density of 20 mW/mm^2. Low temperature (4.2 K) PL spectra of the CAIBE-treated area show excellent optical properties of the homoepitaxially grown GaN (see Fig. 1). The dominant transitions at 3.4655 eV, and 3.4708 eV can be identified as the bound excitons (A^0,X) and (D^0,X). The linewidths are 0.1 meV and 0.11 meV,

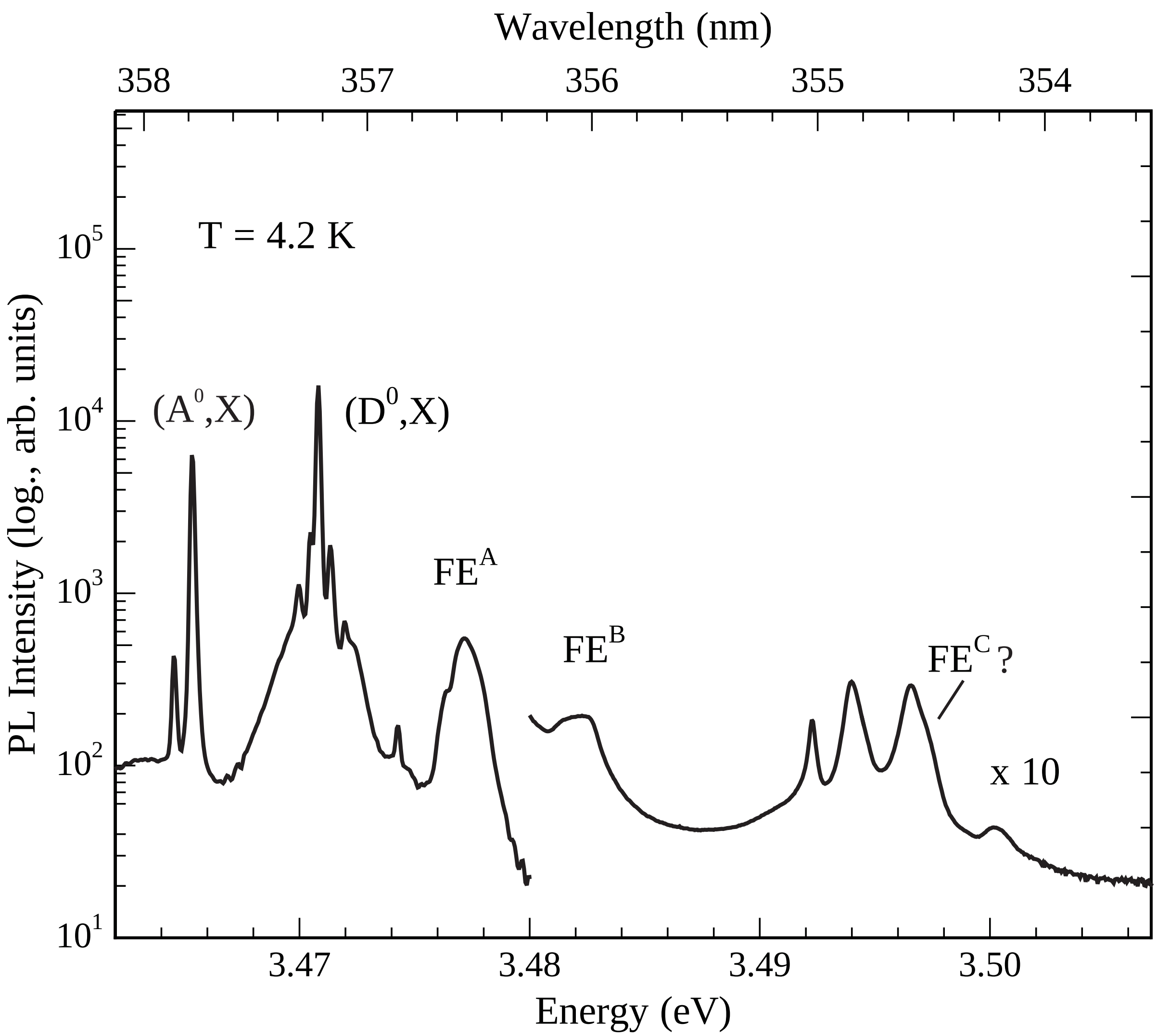

Fig. 1. Photoluminescence of 1.5 μm undoped GaN at 4.2 K, grown homoepitaxially on GaN substrate. Excitation source was a 325 nm HeCd laser with an excitation density of 20 mW/mm^2. The linewidth is as narrow as 0.11 meV for the bound exciton (D^0,X).

respectively. This compares favorably to the best value reported in the literature for MOVPE grown GaN on a sapphire substrate using ELOG with a linewidth of 0.8 meV (T = 1.8K) for the (D^0,X) transition which is broader by a factor of 7 [7]. Furthermore, as shown in Fig. 1, the free excitonic transitions FE_A, FE_B and their excited states are clearly resolved. The location of FE_C is still subject of more detailed examinations. This means, that the GaN quality achieved by homoepitaxy is significantly better than the best heteroepitaxial material reported yet.

4. Conclusion

Homoepitaxially MOVPE grown GaN reveals outstanding optical quality. Linewidths as narrow as 0.11 meV for the (D^0,X) transition at 4.2 K are by a factor of 7 narrower than the best values for heteroepitaxially MOVPE grown GaN on sapphire using ELOG. The pretreatment of the substrates with the CAIBE etching process has proven to be mandatory to achieve improved surface morphologies without scratches, enabling fabrication of critical device structures, e.g. laser diodes. Homoepitaxy dramatically improves the crystal quality of the grown GaN layers to a level that cannot be reached with sapphire substrates.

References

[1] S. Nakamura, M. Senoh, N. Iwasa and S. Nagahama, “High - brightness InGaN blue, green and yellow light emitting diodes with quantum well structures”, *Jap. J. Appl. Phys.*, vol. 34, pp. L 797–L 799, 1995.

[2] S. Nakamura, M. Senoh, S. Nagahama, N. Iwasa, T. Yamada, T. Matsushita, H. Kiyoku, Y. Sugimoto, T. Kozaki, H. Umemoto, M. Sano and K. Chocho, “InGaN/GaN/AlGaN-based laser diodes with modulation-doped strained-layer superlattices grown on an epitaxially laterally overgrown GaN substrate”, *Appl. Phys. Lett.*, vol. 72, pp. 211–213, 1997.

[3] S. Nakamura, M. Senoh, S. Nagahama, N. Iwasa, T. Yamada, T. Matsushita, H. Kiyoku, Y. Sugimoto, T. Kozaki, H. Umemoto, M. Sano and K. Chocho, “Continuous-wave operation of InGaN/GaN/AlGaN-based laser diodes grown on GaN substrates”, *Appl. Phys. Lett.*, vol. 72, pp. 2014–2016, 1998.

[4] J.F.H. Nicholls, H. Gallagher, B. Henderson, C. Trager-Cowan, P.G. Middleton, K.P. O’Donell, T.S. Cheng, C.T. Foxon, and B.H.T. Chai, “Growth and optical properties of GaN grown by MBE on novel lattice-matched oxide substrates”, *Mat. Res. Soc. Symp. Proc.*, vol. 395, pp. 535–539, 1996.

[5] H. Teisseyre, P. Perlin, T. Suski, I. Grzegory, S. Porowski, J. Jun, A. Pietraszko, and T. D. Moustakas, “Temperature dependence of the energy gap in GaN bulk single crystals and epitaxial layer”, *J. Appl. Phys*, vol. 76, pp. 2429–2434, 1994.

[6] M. Schauler, F. Eberhard, C. Kirchner, V. Schwegler, A. Pelzmann, M. Kamp, and K. J. Ebeling, “Dry etching of GaN substrates for high-quality homoepitaxy”, *Appl. Phys. Lett.*, vol. 74, number 8, 1999.

[7] B. Beaumont, M. Vaille, G. Nataf, A. Bouillé, J.-C. Guillaume, P. Vénnègues, S. Haffouz, and P. Gibart, “Mg-enhanced lateral overgrowth of GaN on patterned GaN/sapphire substrate by selective Metal Organic Vapor Phase Epitaxy”, *MRS Internet J. Nitride Semicond. Res.*, vol. 3, art. 20, 1998.

Optimization and characterization of MBE grown InGaAs/AlGaAs GRINSCH structures

Roland Jäger and Eckard Deichsel

We report on the characteristics of optimized graded-index separate-confinement heterostructures (GRINSCH) for InGaAs/AlGaAs broad-area laser diodes. The epitaxial structure consists of a single 8 nm InGaAs quantum well in the active region and AlGaAs cladding layers. For n-type and p-type doping, elemental silicon and CBr_4 as carbon source have been used, respectively. To improve the optical field distribution and the carrier confinement in the active region, different GRINSCH profiles have been investigated. Substrates of different suppliers have also been used in order to assess the influence of defects on device properties.

1. Introduction

High-power broad-area multimode lasers are attractive devices for a wide range of applications. For most of them, a small far field pattern is preferred. Because of the dependency between far field and near field pattern via Fourier transformation, latter has to be improved. The refractive index profile based on the Al content in the GRINSCH region determines this near field pattern width. Other parameters like optical power densities on the facets, intrinsic absorption, filling factors, catastrophic optical mirror damage levels (COMD), threshold current densities and filamentation are influenced by the refractive index profile. Furthermore, carrier confinement in the active zone can be improved leading to a higher characteristic temperature and therefore an increased maximum optical CW power level which is limited by thermal rollover.

2. Experimental procedure

The epitaxial GRINSCH structure has been grown using a solid source Riber 32P MBE. A single 8-nm-thick $In_{0.15}Ga_{0.85}As$ quantum well operating at an emission wavelength of $\lambda = 950\,\mathrm{nm}$ has been centered within graded-index AlGaAs layers surrounded by $Al_{0.3}Ga_{0.7}As$ cladding layers. A highly p-doped ($2 \cdot 10^{20}\ \mathrm{cm}^{-3}$) GaAs cap layer concludes the laser structure. Four GRINSCH structure types have been used for a comparison of the laser characteristics, which are depicted in Fig. 1.

To investigate the influence of the substrate quality on the laser performance, a series of identical structures has been grown on n-type GaAs substrates of four different suppliers. Three of them have been made using vertical gradient freeze (VGF), the fourth using horizontal bridgeman (HB) crystal growth technique.

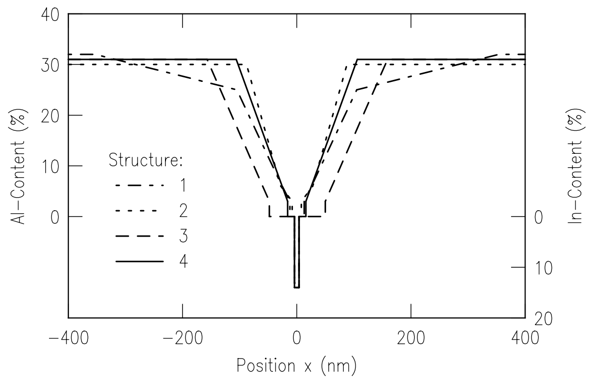

Fig. 1. GRINSCH structures of four epitaxial samples.

3. Characterization

For quick characterization of the four different epitaxial samples in Fig. 1, broad-area lasers have been fabricated in a simple single-mask process. After Ti/Pt/Au p-contact metallization the ridge has been defined by self-aligning wet-chemical etching, followed by substrate thinning and Ge/Au/Ni/Au n-contact metallization. Bars with different cavity lengths have been cleaved and measured under pulsed conditions.

Pulsed P-I characteristics for different cavity lengths have been measured. The differential efficiencies η_{d} and the threshold current densities j_{th} versus cavity length are shown in Fig. 2 and 3, respectively.

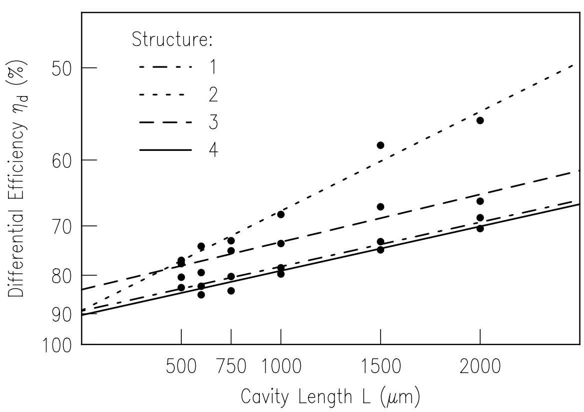

Fig. 2. Internal efficiency and intrinsic absorption of the four epitaxial samples.

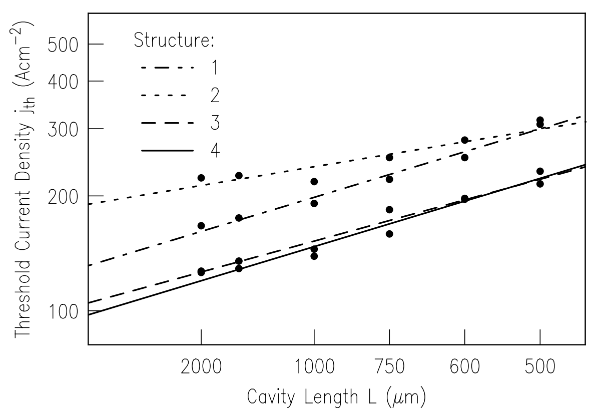

Fig. 3. Threshold current density of the four epitaxial samples.

The internal efficiency η_{i} and intrinsic absorption α_{i} are determined from Fig. 2. Values for the internal efficiency η_{i} of up to 90 % have been achieved. The intrinsic absorption α_{i} is calculated to be as low as 1.8 cm^{-1}.

The threshold current densities for infinite long devices $j_{\mathrm{th,L}\to\infty}$, given by intercept point of the fit and ordinate in Fig. 3 have been improved. Values of 100 Acm^{-2} have been achieved, leading to threshold currents less than 100 mA in pulsed operation for a 500 μm $\times$ 100 μm broad-area device.

Structure	η_i [%]	α_i [cm^{-1}]	$j_{th,L\to\infty}$ [Acm^{-2}]	j_{tr} [Acm^{-2}]	Θ_{FWHM} [°]
1	90	1.8	131	123	38
2	90	3.8	191	178	30
3	85	1.9	103	98	34
4	90	1.8	98	92	34

Tab. 5. Comparison of the four epitaxial structures.

Table 5 gives an overview over the characteristic parameters of the four structures. Reproducible results have been achieved for internal efficiencies and intrinsic losses. Threshold current densities and far-field angles have been improved.

Due to the experiments according to substrate quality, Structure 4 has been grown four times on substrates of different suppliers. The results are shown in Tab. 6.

Substrate	η_i [%]	α_i [cm^{-1}]	$j_{th,L\to\infty}$ [Acm^{-2}]	j_{tr} [Acm^{-2}]	Θ_{FWHM} [°]
A	90	1.7	98	92	33
B	90	2.0	95	89	36
C	90	1.9	119	113	34
D	90	1.8	98	92	34

Tab. 6. Comparison of four different substrate suppliers.

The main parameters as internal efficiencies, absorption losses and threshold current densities does not vary strongly. Only Substrate C shows slightly increased values in threshold current densities.

4. Conclusion

In summary, we have optimized the GRINSCH zone for 950 nm InGaAs/AlGaAs broad-area laser diodes. To improve the far field pattern and the carrier confinement in the active region, modified GRINSCH profiles have been investigated. Highest internal efficiencies of 90 % and far-field angles of 30° have been achieved. Substrates of different suppliers have also been investigated. It was possible to show, that the main device parameters do not depend on the substrate manufacturers in this comparison.

Short Pulse Electroluminescence of GaN based Light Emitting Diodes

Veit Schwegler and Arthur Pelzmann

GaN based light emitting diodes have been investigated concerning their electroluminescence behavior under short pulse operation. The optical response has been measured for different wavelengths and time slots. The decay time of the electroluminescence being in the range of 1 - 100 ns is a powerful measure for the recombination mechanism of the EL.

1. Introduction

In recent years an impressive progress has been made in the development of nitride based devices. High brightness blue, green and amber light emitting diodes (LEDs) as well as most recently long-live blue laser diodes have been demonstrated [1][2]. In spite of very high dislocation densities ($10^8 - 10^{10}\mathrm{cm}^{-2}$), caused by heteroepitaxial growth, the realized GaN-based light emitters show external quantum efficiencies up to 10%-16%. To develop such high brightness LEDs an efficient injection of the carrier into the active layer and a detailed knowledge about recombination mechanisms, which take place, are necessary. Usually photoluminescence (PL) measurements where performed to examine optical processes in the epitaxial layers. Furthermore, time resolved PL of LED structures has been performed to learn about recombination dynamics [3]. However, it is not clear whether emission mechanisms obtained by optical excitation can be simply transferred to the case of device operation, where the electrons and holes are injected from the n- and p-doped cladding layers.

2. Experimental Setup

The LED structures under investigation were an AlGaN/GaN double heterostructure LED (DH) with a 150 nm thick Zn-doped GaN layer as active recombination zone and an InGaN/GaN single quantum well structure (SQW). The devices were soldered on a BNC connector and dc biased with 0.1 mA during pulse excitation via a bias-T. Electrical pulses with 10 ns or 15 ns pulse length were generated using a Tektroniks 109 mercury pulser or an Avtech AVI-C. The reflection of the current pulse was minimized by adding an impedance matching resistance network to the device under test. The optical response of the LEDs were detected by a Hamamatsu photo multiplier tube (PMT). Light output and current were sampled in time with a Tektroniks sampling oscilloscope TDS520. An Acton 500 monochromator was used for spectrally resolved measurements.

3. Measurements and Results

Figure 1 shows the optical response over all wavelengths of a Zn-doped DH-LED and a SQW-LED, both electrically pumped with 10 ns long current pulses of 1 A. Due to the short pulse width even at those high currents the optical characteristics of the devices should not be influenced by thermal effects, also

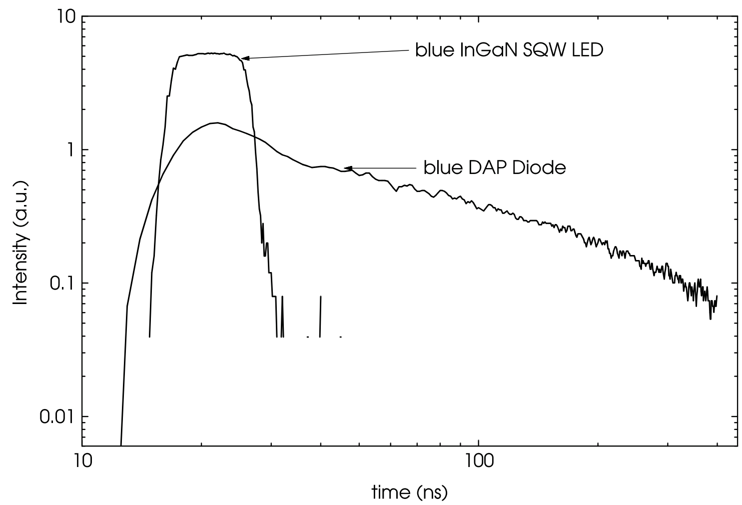

Fig. 1. Photomultiplier response of the AlGaN/GaN-DH LED and InGaN-SQW LED after electrical 10 ns excitation.

device degradation is avoided. A significant difference concerning the decay times of the LEDs can be seen. The decay time of the InGaN SQW device is approx. 1 ns. For the Zn-doped DH structures two exponential decay times with values of 2-3 ns and approx. 96 ns are observed.

The origin of these two different carrier lifetimes is revealed by the time resolved electroluminescence spectra of the Zn-doped AlGaN/GaN-DH LED, shown in figure 2 for various times after excitation with 15 ns pulses. Along with the visible peak, centered at 421 nm, a narrower UV peak is observed, which has a center wavelength of 367 nm with a full width half maximum (FWHM) of 8 nm. The visible emission is attributed to recombination via Zn-recombination centers. At high injection carrier densities the Zn-recombination centers which have a very slow decay time saturate and an additional UV band is pumped, based on an efficient band-band recombination mechanism with faster decay times. A slight peak shift of the UV emission can be observed which might be generated by band filling effects. The almost two magnitudes longer decay time of the visible emission can be explained by localization of carriers at the Zn atoms, which increases the carrier lifetime.

The time resolved spectra of the InGaN/GaN SQW LED are depicted in figure 2. Even at high current pulses no UV band is generated. The single peak emission is centered at 427 nm and has a FWHM of 19.9 nm. The emission maximum shifts after the electrical pulse excitation from 427 nm to 429 nm. Since the radiative lifetime seems to increase with higher In content, this could be caused by In fluctuation in the active layer [4].

4. Conclusion

Time resolved short pulse electroluminescence has proven its suitability to investigate recombination processes in GaN based devices. The different decay times of the optical transitions give an evidence about the efficiency, nature and place of the observed recombination process.

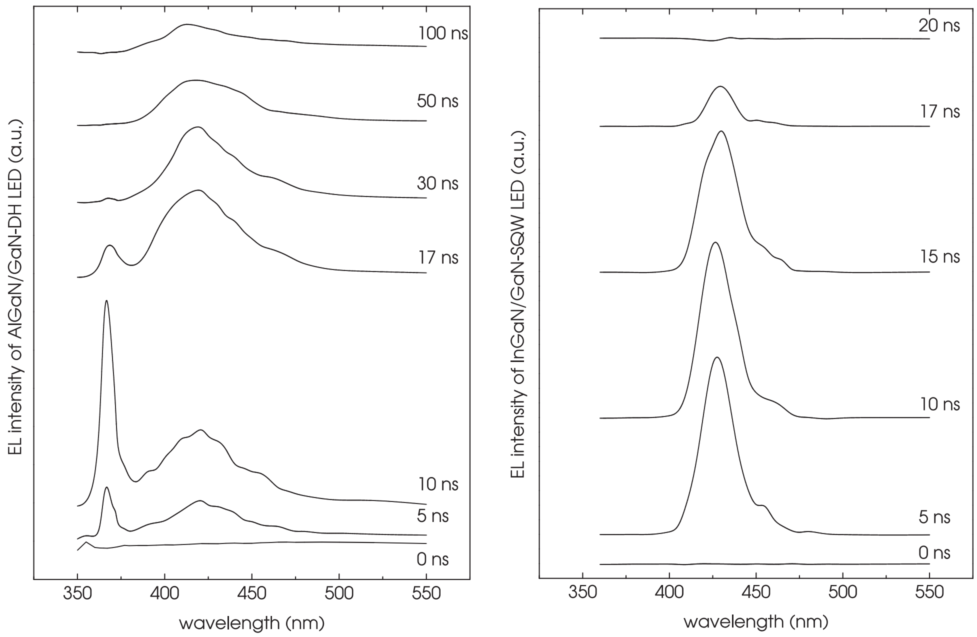

Fig. 2. Time-resolved electroluminescence spectra of a Zn-doped AlGaN/GaN-DH LED and a InGaN-SQW LED, which were extracted from the optical response of the device.

References

[1] S. Nakamura, M. Senoh, N. Iwasa, and S. Nagahama, "High-Brightness InGaN Blue, Green and Yellow Light-Emitting Diodes with Quantum Well Structures", *Jap. J. Appl. Phys.*, vol. 34, pp. L797–L799, 1995.

[2] S. Nakamura, M. Senoh, S. Nagahama, N. Iwasa, T. Yamada, T. Matsushita, H. Kiyoku, Y. Sugimoto, T. Kozaki, H. Umemto, M. Sano, and K. Chocho, "InGaN/GaN/AlGaN-based laser diodes with cleaved facets grown on GaN substrates", *Appl. Phys. Lett.*, vol. 73, pp. 832–834, 1998.

[3] G. Mohs, B. Fluegel, H. Giessen, H. Tajalli, N. Peyghambarian, P. Chiu, B. Phillips, and M. Osinski, "Photoluminescence decay dynamics in an InGaN/AlGaN/GaN double-heterostructure blue-light-emitting diode", *Appl. Phys. Lett.*, vol. 67, pp. 1515–1517, 1995.

[4] Y. Narukawa, S. Saijyo, Y. Kawakami, and S. Fujita, "Time-resolved electroluminescence spectroscopy of InGaN single quantum well LEDs", *Proc. 2nd International Conference on Nitride Semiconductors (ICNS'97)*, pp. 226–227, Tokushima, Japan, Oct. 1997.

Ph.D. Theses

[Ph.D.-1] Reiner, G., *Molekularstrahlepitaxie für hocheffiziente Laserdioden mit Vertikalresonator*, Ph.D. Thesis, Dept. of Optoelectronics, University of Ulm, 1998.

[Ph.D.-2] Sowada, D., *Material- und Prozeßtechnologien für langwellige Laserdioden mit Vertikalresonator*, Ph.D. Thesis, Dept. of Optoelectronics, University of Ulm, 1998.

[Ph.D.-3] Faltin, K., *Untersuchungen zur Nahfeldverteilung von Transversalmoden in Laserdioden mit Vertikalresonator*, Ph.D. Thesis, Dept. of Optoelectronics, University of Ulm, 1998.

Diploma Theses and Semester Projects

[D-1] Förstner, Jörg, *Aufbau und Integration eines DSP-Systems zur Verarbeitung der Meßdaten von Rasterkraftmikroskopen*, Diploma Thesis, Dept. of Experimental Physics, University of Ulm, 1998.

[D-2] Beierlein, Tilman Artur, *Herstellung und Charakterisierung von dünnen InGaN Schichten und ihre Anwendung in organischen Schichten*, Diploma Thesis, IBM-Rüschlikon, Switzerland, 1998.

[D-3] Vogelmann, Holger Laurenz, *Vertikalemittierende Dioden-Kaskaden-Laser*, Semester Project, Dept. of Optoelectronics, University of Ulm, 1998.

[D-4] Palm, Michael, *Entwicklung einer Prozetechnologie zur Herstellung von GaN-basierten, kantenemittierenden Leuchtdioden*, Semester Project, Dept. of Optoelectronics, University of Ulm, 1998.

[D-5] Lorch, Steffen, *Reactive ion Etching with CH4/H2/Ar on InP and SiCl4/(Ar) on AlGaAs*, Semester Project, University of York, UK, 1998.

[D-6] Gürel, Cüneyt, *Aufbau eines Messplatzes zur Bestimmung der Absorption in Wellenleitern*, Semester Project, Dept. of Optoelectronics, University of Ulm, 1998.

[D-7] Riedel, Markus, *Untersuchung und Realisierung eines kompakten faseroptischen Systems zur Wellenlängenmessung*, Diploma Thesis, Daimler-Benz AG, Ulm, 1998.

[D-8] Walker, Craig, *Monolithic Integration of Semiconductor Lasers and Photo Diodes using Dry Etched Mirror Facets*, Diploma Thesis, Dept. of Optoelectronics, University of Ulm, 1998.

[D-9] Sönmez, Ertuğrul, *Herstellung und Charakterisierung von zweidimensionalen Vertikallaserdiodenarrays*, Diploma Thesis, Dept. of Optoelectronics, University of Ulm, 1998.

[D-10] Czwella, Dirk, *Antireflexionsbeschichtungen für Laserdioden und Laserdiodenverstrker*, Diploma Thesis, Dept. of Optoelectronics, University of Ulm, 1998.

[D-11] Graf, Jürgen, *Aufbau und Charakterisierung eines 8 x 8 Laserdiodenarrays für die Flip-Chip Technologie*, Diploma Thesis, Dept. of Optoelectronics, University of Ulm, 1998.

[D-12] Mohn, Brigitta, *Herstellung und Charakterisierung von Diodenlaserbarren höchster Ausgangsleistung*, Diploma Thesis, Dept. of Optoelectronics, University of Ulm, 1998.

[D-13] Mederer, Felix, *Untersuchung von parallelen optischen Datenübertragungsstrecken mit Vertikallaserdioden*, Diploma Thesis, Dept. of Optoelectronics, University of Ulm, 1998.

[D-14] Scherer, Marcus, *Optimierung ohmscher Kontakte auf Mg-dotiertem Galliumnitrid*, Semester Project, Dept. of Optoelectronics, University of Ulm, 1998.

[D-15] Kunze, Jochen, *Wachstum und Charakterisierung von InGaN MQW Schichten für Leuchtdioden*, Diploma Thesis, Dept. of Optoelectronics, University of Ulm, 1998.

[D-16] Unold, Heiko Johannes, *Vertical Cavity Diode Lasers in Densely Packed Array Arrangement*, Diploma Thesis, Dept. of Optoelectronics, University of Ulm, 1998.

Talks and Seminars

[T-1] H.Y.A. Chung, G. Stareev, J. Joos, and J. Mähnss, "Gas source MBE growth of InAsP/InGaAsP QWs GRINSCH lasers showing low threshold current densities and high power", *National MBE workshop*, Hamburg, Germany, Sept., 1998.

[T-2] K.J. Ebeling, "Optical Interconnect Technology", *9. Edgar Lüscher Seminar*, Serneus, Switzerland, Feb., 1998.

[T-3] K.J. Ebeling, "High Efficiency and High Power Vertical Cavity Laser Diodes and Arrays", *Italian-German International Symposium on Microcavities - Quantum Electrodynamics and Devices*, Menaggio, Italy, Apr., 1998.

[T-4] K.J. Ebeling, "State-of-the-Art in Semiconductor Laser Research", *Halbleiterlaserworkshop, Fachbereich Physik*, Universität Marburg, Germany, June, 1998.

[T-5] K.J. Ebeling, "Vom Photonenzähmen und Profitstreben: Neuere Entwicklungen bei Halbleiterlasern", *Walter-Schottky-Institut*, TU München, Germany, June, 1998.

[T-6] K.J. Ebeling, "Vertical Cavity Surface Emitting Laser Diodes: Basics and Applications I-III", *Summer School*, St. Andrews, Scotland, June, 1998.

[T-7] K.J. Ebeling, "Vertical cavity laser diodes and arrays for data transmission and high power generation", *Summer School and European Optical Society Topical Meeting on Semiconductor Microcavity Light Emitters, Tutorial*, Ascona, Switzerland, Sept., 1998.

[T-8] K.J. Ebeling, "Epitaxie auf GaN Substraten: Neue Perspektiven für Grundlagenforschung und Anwendungen", *Photonik-Symposium der Volkswagenstiftung*, Seeheim-Jugenheim, Germany, Oct., 1998.

[T-9] K.J. Ebeling, "Höchstbitratiger optischer Datentransfer zwischen Prozessorchip-Modulen im Esprit-Projekt OIIC (Optically Interconnected Integrated Circuits) der Europäischen Gemeinschaft", *Vorstellung des 5. Rahmenprogramms der Europäischen Union für Forschung, "Technologische Entwicklung und Demonstration"*, Haus der Wirtschaft, Stuttgart, Germany, Nov., 1998.

[T-10] K.J. Ebeling, "Laserdioden mit Vertikalresonator und deren Anwendungen", *Physikalische Gesellschaft, Ortsverband Aalen*, Fachhochschule Aalen, Germany, Dec., 1998.

[T-11] K.J. Ebeling, "Vertikal emittierende Laser (VCSELs) für breitbandige optische Übertragung", *Seminar Technische Physik*, Universität Würzburg, Germany, Dec., 1998.

[T-12] K.J. Ebeling, "VCSELs als Quellen für optische Polymerfaser-Systeme", *ITG-Fachgruppentreffen "Optische Polymerfasern"*, Universität Ulm, Germany, Dec., 1998.

[T-13] I. Ecker, S. Menzel, M. Kamp, and K.J. Ebeling, "GSMBE von GaInAsN", *Deutscher MBE Workshop*, Hamburg, Germany, Sept., 1998.

[T-14] M. Golling, “Gas source MBE von InAlGaP/InGaP MQW Laserdioden”, *Deutscher MBE Workshop*, Hamburg, Germany, Sept., 1998.

[T-15] J. Heerlein, “Diodenlaserarrays und einmodige Diodenlaser mit instabilen Resonatoren für hohe Leistungen”, *2. Statusseminar, BMBF project* MILASI, Gera, Germany, Mar., 1998.

[T-16] J. Heerlein, “Kantenemittierende Laser mit seitlicher Oxidschicht zur transversal einmodigen Wellenführung”, IAF Freiburg, Germany, July, 1998.

[T-17] C. Kirchner, “Wachstum nitridischer Bauelementstrukturen mit MOVPE”, *AIXTRON*, Aachen, Germany, Sept., 1998.

[T-18] M. Kamp, M. Mayer, A. Pelzmann, C. Kirchner, and K.J. Ebeling, “Growth kinetics of group III nitrides using Ammonia in MBE”, *Proc. Int. GaN Workshop*, Schloss Ringberg, Jan., 1998.

[T-19] M. Kamp, “GaN basierende Halbleiter: Anwendungen, Grundlagen und Technologie”, *Materialwissenschaftliches Kolloquium der Universität Braunschweig*, Braunschweig, Germany, July, 1998.

[T-20] M. Kamp, C. Kirchner, M. Mayer, A. Pelzmann, V. Schwegler, and K.J. Ebeling, “Epitaxie auf GaN Substraten: Neue Perspektiven für Grundlagenforschung und Anwendungen”, *VW-Photonik Symposium*, Darmstadt, Germany, 1998.

[T-21] M. Kamp, C. Kirchner, M. Mayer, A. Pelzmann, V. Schwegler, and K.J. Ebeling, “ Perspectives of GaN Substrates for Devices”, *Third Symposium on III-V Nitride Materials and Processes, Electrochemical Society Meeting*, Boston, MA, USA, Dec., 1998.

[T-22] M. Kamp, A. Pelzmann, C. Kirchner, M. Mayer, and K.J. Ebeling, “GaN homoepitaxy for Device Applications”, *CIST*, Hsin-Chu, Taiwan, Dec., 1998.

[T-23] M. Kamp, “Solutions for heteroepitaxial growth of GaN and their impact on devices”, *ITRI*, Hsin-Chu, Taiwan, Dec., 1998.

[T-24] R. Michalzik, D. Wiedenmann, B. Weigl, R. King P. Schnitzer, C. Jung, W. Schmid, R. Jäger, M. Grabherr, and K.J. Ebeling, “Vertikallaserdioden – Physik und Anwendung”, *DPG Frühjahrstagung*, Konstanz, Germany, Mar., 1998.

[T-25] R. Michalzik, K.J. Ebeling, D. Wiedenmann, R. King, and P. Schnitzer, “Optische Kurzstreckenverbindungen mit Vertikallaserdioden”, *ITG/VDE-Workshop, Modellierung photonischer Komponeneten und Systeme MPKS*, Ilmenau, Germany, May, 1998.

[T-26] R. Michalzik, “Vertical cavity laser diodes - Principles and applications”, *LASERION Workshop 1998 on it Microfabrication, Nanostructured Materials and Biotechnology*, Schloß Ringberg, Germany, June, 1998.

[T-27] R. Michalzik, D. Wiedenmann, M. Kicherer, and K.J. Ebeling, “VCSEL Noise”, *Europ. Semicond. Laser Workshop*, El Escorial, Spain, Sept., 1998.

[T-28] R. Michalzik, D. Wiedenmann, R. King, P. Schnitzer, C. Jung, R. Jäger, and K.J. Ebeling, “VCSELs for high-speed optical data transmission”, *Bell Laboratories, Lucent Technologies*, Holmdel, NJ, USA, Nov., 1998.

[T-29] A. Pelzmann, C. Kirchner, M. Mayer, V. Schwegler, M. Schauler, M. Kamp, and K.J. Ebeling, "Blue light-emitting diodes on GaN substrates, growth and characterization", Mitsubishi Inc., Osaka, Japan, Nov., 1998.

[T-30] P. Unger, "Halbleiter-Diodenlaser", *Seminar* Technische Elektronik, *Gesamthochschule Kassel*, Kassel, Germany, May, 1998.

[T-31] P. Unger, "Hochleistungs-Diodenlaser im Materialsystem InGaAs/AlGaAs", *Seminar, 4. Physikalisches Institut, Universität Stuttgart*, Stuttgart, Germany, June, 1998.

[T-32] P. Unger, "Halbleiter-Diodenlaser mit hoher Ausgangsleistung", *Siemens AG, Zentralbereich Technik*, München, Germany, Oct., 1998.

Publications and Conference Contributions

[P-1] H.Y.A .Chung, G. Stareev, J. Joos J. Maehnss, and K.J. Ebeling, "Very low threshold current density 1.3 μm-InAsP/InGaAsP strained quantum well GRINSCH laser grown by Gas Source MBE", in *Proc. IPRM '98*, pp. 706–708, Tsukuba, Japan, May, 1998.

[P-2] H.Y.A .Chung, G. Stareev, J. Joos J. Maehnss, and K.J. Ebeling, "Gas source MBE growth of 1.3 μm–InAsP/InGaAsP quantum well GRINSCH lasers showing low threshold current densities and high output power", in *Proc. Tenth Int. Conference on MBE*, pp. 319–320, Cannes, France, Sept., 1998.

[P-3] K.J. Ebeling, R. Michalzik, R. King, P. Schnitzer, D. Wiedenmann, R. Jäger, C. Jung, M. Grabherr, and M. Miller, "Applications of VCSELs for optical interconnects", in *Proc. ECOC '98*, p. 453, Madrid, Spain, Sept., 1998.

[P-4] K.J. Ebeling, "Recent progress in vertical cavity surface emitting lasers", in *Proc. ISLC '98*, pp. 5–6, Nara, Japan, Oct., 1998.

[P-5] F. Eberhard, M. Schauler, E. Deichsel, C. Kirchner, and P. Unger, "Comparison of the etching behavior of GaAs and GaN in a chemically-assisted ion-beam etching system", in *Proc. Micro- and Nano-Engineering, MNE'98*, pp. 167–168, Leuven, Belgium, Sept., 1998.

[P-6] M. Grabherr, R. Jäger, M. Miller, C. Thalmaier, J. Heerlein, R. Michalzik, and K.J. Ebeling, "Bottom-emitting VCSELs for high cw optical output power", *IEEE Photon. Techn. Lett.*, vol. 10, pp. 1061–1063, 1998.

[P-7] M. Grabherr, M. Miller, R. Jäger, and K.J. Ebeling, "Efficient bottom emitting VCSEL arrays for high cw optical output power", *Electron. Lett.*, vol. 34, pp. 1227–1228, 1998.

[P-8] M. Grabherr, M. Miller, R. Jäger, R. Rösch, U. Martin, and K.J. Ebeling, "Densely packed high power VCSEL arrays", in *Proc. ISLC'98*, pp. 245–246, Nara, Japan, Oct., 1998.

[P-9] J. Heerlein, M. Grabherr, R. Jäger, and P. Unger, "Single-mode AlGaAs-GaAs lasers using lateral confinement by native-oxide layers", *IEEE Photonics Technology Lett.*, vol. 10, pp. 498–500, 1998.

[P-10] J. Heerlein, E. Schiehlen, R. Jäger, and P. Unger, "63 % wall-plug efficiency InGaAs/AlGaAs broad area laser diodes and arrays", in *Proc. CLEO Europe 98, CThG2*, p. 267, Glascow, UK, Sept., 1998.

[P-11] J. Heerlein, S. Gruber, and P. Unger, "Mode analysis of semiconductor lasers using lateral confinement by native-oxide layers", *IEEE J. Quantum Electron.*, vol. 34, pp. 1953–1958, 1998.

[P-12] J. Heerlein, S. Gruber, M. Grabherr, R. Jäger, and P. Unger, "High-efficiency laterally oxidized InGaAs/AlGaAs single-mode lasers", in *Proc. ISLC'98*, pp. 219–220, Nara, Japan, Oct., 1998.

[P-13] R. Jäger, J. Heerlein, E. Deichsel, and P. Unger, "63 % wallplug efficiency MBE grown InGaAs/AlGaAs broad-area laser diodes and arrays with carbon p-type doping using CBr_4", in *Proc. Tenth Int. Conference on MBE*, pp. 135–136, Cannes, France, Sept., 1998.

[P-14] G. Jost, U. Martin, R. Jäger, J. Heerlein, and P. Unger, "High-power tapered semiconductor amplifier with Nd:YAG microcrystal master laser oscillator", in *Proc. CLEO Europe 98, CTuI34*, Glascow, UK, Sept., 1998.

[P-15] G. Jost, U. Martin, R. Jäger, J. Heerlein, E. Deichsel, and P. Unger, "High-power, single frequency semiconductor amplifier system with feedback-insensitive Nd:YAG microcrystal master oscillator", in *Proc. LEOS '98, vol. 1*, pp. 350–351, Orlando, FL, USA, Dec., 1998.

[P-16] C. Jung, R. King, R. Jäger, M. Grabherr, F. Eberhard, R. Michalzik, and K.J. Ebeling, "Highly efficient oxide confined VCSEL arrays for parallel optical interconnects", in *Optics in Computing OC '98*, pp. 2–5, Brugge, Belgium, Jun., 1998.

[P-17] R. King, R. Michalzik, C. Jung, M. Grabherr, F. Eberhard, R. Jäger, and K.J. Ebeling, "Oxide confined 2D VCSEL arrays for high-density inter/intra- chip interconnects", in *Proc. SPIE OPTOELECTRONICS '98 - Vertical-Cavity Surface-Emitting Lasers II*, vol. 3286, pp. 64–71, San Jose, California, USA, Jan., 1998.

[P-18] R. King, R. Michalzik, R. Jäger, F. Eberhard, C. Jung, M. Grabherr, and K.J. Ebeling, "Vertical-cavity surface-emitting laser diode arrays for parallel optical interconnects within multichip modules", in *Proc. PIERS '98 - Progress in Electromagnetics Research Symposium*, p. 1066, Nantes, France, Jul., 1998.

[P-19] R. King, D. Wiedenmann, P. Schnitzer, R. Jäger, R. Michalzik, and K.J. Ebeling, "Single-mode and multimode 2D VCSEL arrays for parallel optical interconnects", in *Proc. ISLC '98*, pp. 103–104, Nara, Japan, Oct., 1998.

[P-20] M. Mayer, A. Pelzmann, M. Kamp, and K.J. Ebeling, "Reactive MBE group III nitrides: High quality homoepetaxial GaN and ultra-violet light emitting diodes", in *Proc. Tenth Int. Conference on MBE*, pp. 203–204, Cannes, France, Sept., 1998.

[P-21] M. Mayer, A. Pelzmann, C. Kirchner, M. Schauler, F. Eberhard, M. Kamp, P. Unger, and K.J. Ebeling, "Device performance of ultra-violet light emitting diodes grown by MBE", *J. of Crystal Growth*, vol. 189-190, pp. 782–785, 1998.

[P-22] R. Michalzik, M. Grabherr, and K.J. Ebeling, "High-power VCSELs: Modeling and experimental charaterization (invited)", in *Proc. Optoelectronics '98 - Vertical-Cavity Surface-Emitting Lasers II*, vol. 3286, pp. 206–219, San Jose, California, USA, Jan., 1998.

[P-23] R. Michalzik, D. Wiedenmann, B. Weigl, R. King P. Schnitzer, C. Jung, W. Schmid, R. Jäger, M. Grabherr, and K.J. Ebeling, "Vertikallaserdioden - Physik und Anwendung", in *DPG Frühjahrstagung*, p. 212, Konstanz, Germany, Mar., 1998.

[P-24] R. Michalzik, "Vertikallaserdioden", *Funkschau, Ausgabe 7/98*, pp. 91–93, 1998.

[P-25] R. Michalzik, M. Grabherr, R. Jäger, M. Miller, and K.J. Ebeling, "Progress in high power VCSELs and arrays", in *Proc. SPIE Photonics*, vol. 3419, pp. 187–195, Taipei, Taiwan, July, 1998.

[P-26] R. Michalzik, K.J. Ebeling, R. King, P. Schnitzer, D. Wiedenmann, C. Jung, and R. Jäger, "High-performance VCSEL array for optical interconnects", in *Proc. LEOS '98, vol. 2*, vol. 3419, pp. 29–30, Orlando, FL, USA, Dec., 1998.

[P-27] R. Michalzik and K.J. Ebeling, "Vertical cavity laser diodes - promising devices for optical interconnect applications", *Laser und Optoelektronik*, vol. 30, pp. 78–85, 1998.

[P-28] M. Miller, M. Grabherr, R. Jäger, U. Martin, and K.J. Ebeling, "High power 3×3 VCSEL array (invited)", in *Proc. CLEO Europe 98, CThG1*, Glasgow, UK, Sept., 1998.

[P-29] A. Pelzmann, C. Kirchner, M. Mayer, V. Schwegler, M. Schauler, M. Kamp, K.J. Ebeling, I. Grzegory, M. Leszczynski, G. Nowak, and S. Porowski, "Blue light emitting diodes on GaN substrates, growth and characterization", *J. of Crystal Growth*, vol. 189-190, pp. 167–171, 1998.

[P-30] W. Schmid, D. Wiedenmann, M. Grabherr, R. Jäger, R. Michalzik, and K.J. Ebeling, "CW-operation of a diode cascade InGaAs quantum well VCSEL", *Electron. Lett.*, vol. 34, pp. 553–555, 1998.

[P-31] P. Schnitzer, M. Grabherr, R. Jäger, C. Jung, and K.J. Ebeling, "Linear 1×8 GaAs VCSEL arrays for 24 Gbit/s data rate transmission", *Electron. Lett.*, vol. 34, pp. 187–18, 1998.

[P-32] P. Schnitzer, M. Grabherr, R. Jäger, C. Jung, R. King, R. Michalzik, D. Wiedenmann, and K.J. Ebeling, "Short distance polymer optical fiber data transmission at 2.5 Gb/s using GaAs vertical cavity surface emitting lasers at λ = 780 nm", in *Proc. OFC '98*, pp. 157–158, San Jose, CA, USA, Feb., 1998.

[P-33] P. Schnitzer, M. Grabherr, R. Michalzik, R. Jäger, J. Joos, C. Jung, R. King, W. Schmid, D. Wiedenmann, and K.J. Ebeling, "High performance VCSEL arrays for optical interconnection", in *Proc. ECTC '98*, pp. 762–770, Seattle, Washington, USA, May, 1998.

[P-34] P. Schnitzer, M. Grabherr, R. Michalzik, R. Jäger, J. Joos, C. Jung, R. King, W. Schmid, D. Wiedenmann, and K.J. Ebeling, "Hochbitratige Datenübertragung mit Vertikallasermatrizen", in *"Messung und Modellierung in der optischen Nachrichtentechnik", MMONT'98, VDE-IT6*, Günzburg, Germany, Mar., 1998.

[P-35] P. Schnitzer, M. Grabherr, R. Jäger, C. Jung, and K.J. Ebeling, "Bias-free 2.5 Gbit/s data transmission using polymide passivated GaAs VCSELs", *Electron. Lett.*, vol. 34, pp. 573–575, 1998.

[P-36] P. Schnitzer, M. Grabherr, R. Jäger, R. Michalzik, W. Schmid, and K.J. Ebeling, "GaAs VCSELs at λ = 780 nm for short distance polymer optical fiber links at 2.5 Gb/s", in *Proc. CLEO Europe 98, CTuC4*, p. 51, Glascow, UK, Sept., 1998.

[P-37] P. Schnitzer, R. Jäger, R. King, R. Michalzik, D. Wiedenmann, and K.J. Ebeling, "InGaAs VCSEL arrays for 1 Gbit/s bias-free and 8 Gbit/s biased data transmission", in *Proc. ECOC '98*, pp. 195–196, Madrid, Spain, Sept., 1998.

[P-38] P. Schnitzer, M. Grabherr, R. Jäger, R. King, R. Michalzik, D. Wiedenmann, F. Mederer, and K.J. Ebeling, "Vertical-cavity surface-emitting lasers for plastic optical fiber data links", in *Proc. POF '98*, pp. 157–162, Berlin, Germany, Oct., 1998.

[P-39] P. Schnitzer, R. Jäger, M. Grabherr, D. Wiedenmann, F. Mederer, and K.J. Ebeling, "GaAs VCSELs for biased and bias-free multi Gb/s data transmission over 4.3 km standard 1300 nm single-mode fiber", in *Proc. LEOS '98*, pp. 164–165, Orlando, FL, USA, Dec., 1998.

[P-40] P. Schnitzer, R. Jäger, C. Jung, R. Michalzik, D. Wiedenmann, F. Mederer, and K.J. Ebeling, "Biased and bias-free multi-Gb/s data links using GaAs VCSEL's and 1300 nm single-mode fiber", *Photon. Technol. Lett.*, vol. 10, pp. 1781–1783, 1998.

[P-41] D. Wiedenmann, P. Schnitzer, W. Schmid, C. Jung, M. Grabherr, R. Jäger, R. Michalzik, and K.J. Ebeling, "Extremely low intensity noise single-mode vertical cavity surface emitting lasers", in *CLEO Europe 98, CMH7*, p. 33, Glascow, UK, Sept., 1998.

[P-42] D. Wiedenmann, M. Grabherr, C. Jung, R. Jäger, R. Michalzik, P. Schnitzer, and K.J. Ebeling, "Feedback insensitive 3 Gb/s fiber interconnect with low noise single-mode VCSEL", in *Proc. ECOC '98*, pp. 457–458, Madrid, Spain, Sept., 1998.

[P-43] D. Wiedenmann, P. Schnitzer, C. Jung, M. Grabherr, R. Jäger, R. Michalzik, and K.J. Ebeling, "Noise characteristics of 850 nm single-mode vertical cavity surface emitting lasers", *Appl. Phys. Lett.*, vol. 73, pp. 717–719, 1998.

[P-44] D. Wiedenmann, C. Jung, M. Grabherr, R. Jäger, U. Martin, R. Michalzik, and K.J. Ebeling, "Oxide-confined vertical-cavity semiconductor optical amplifier for 980 nm wavelength", in *Proc. CLEO '98*, pp. 378–379, San Francisco, CA, USA, May, 1998.

[P-45] Knüpfer B, M. Welkerand, C. Jung, D. Wiedenmann, K.J. Ebeling, Ch. Oehler, W. Geißelbrecht, S. Malzer, and G.H. Döhler, "Novel VCSEL-based smart pixel for high contrast high-gain and high-speed optical switching", *SPIE Proc.*, vol. 3288, pp. 23–32, 1998.

[P-46] B. Holländer, S. Mantl, C. Kirchner, A. Pelzmann, M. Kamp, K. J. Ebeling, S. Christiansen, and H. P. Strunk, "Ion channeling studies of GaN layers on C-oriented sapphire", *Nuclear Instruments and Methods in Physics Research B 136-138*, pp. 1248–1252, 1998.

[P-47] T. Suski, J. Jun, M. Leszczynski, H. Teisseyre, S. Strite, A. Rocket, A. Pelzmann, M. Kamp, and K.J. Ebeling, "Optical activation and diffusivity of ion-implanted Zn acceptors in GaN under high pressure, high temperature annealing", *J. Appl. Phys.*, vol. 84, pp. 1155–1157, 1998.

[P-48] K. Kornitzer, K. Thonke, R. Sauer, M. Mayer, M. Kamp, and K.J. Ebeling, "Photocurrent and photoluminesence measurements in the near-band-edge region of 6H GaN", *J. Appl. Phys.*, vol. 83, pp. 4397–4402, 1998.

[P-49] S. Christiansen, M. Albrecht, H.P. Strunk, C. Zanotti-Fregonara, G. Salviati, M. Mayer, A. Pelzmann, and M. Kamp, "Structural and luminesence properties of homoepitaxial GaN layers", *submitted to Mat. Res. Soc. Symp. Proc. of Spring Meeting 1998*, 1998.

[P-50] B. Holländer, S. Mantl, A. Pelzmann, C. Kirchner, M. Mayer, M. Kamp, K. J. Ebeling, S. Christiansen, and H. P. Strunk, "Ion scattering studies of defects in GaN thin films on C-orientated sapphire", *Mat. Res. Soc. Symp. Proc.*, vol. 512, pp. 543–548, 1998.

[P-51] A. Bramati, A.Z. Khoury, J.-P. Hermier, E. Giacobino, J.-Ph. Poizat, P. Grangier, K.J. Ebeling, and P. Schnitzer, "Transverse modes correlations and intensity noise in VCSELs", in *Proc. EQEC'98, QThB4*, p. 172, Glasgow, Scottland, 1998.

[P-52] B. Dhoedt, R. Baets, P. Van Daele, P. Heremans, J. Van Campenhout, J. Hall, R. Michalzik, A. Schmid, H. Thienpont, R. Vounckx, A. Neyer, D.C. O'Brien, and J. Van Koetsem, "Optically interconnected integrated circuits to solve the CMOS interconnect bottleneck", in *Proc. ECTC'98*, pp. 992–998, Seattle, WA, USA, May, 1998.

[P-53] C. Degen, J.-L. Vey, W. Elsäßer, P. Schnitzer, and K.J. Ebeling, "Amplitude noise squeezed light from polarisation singlemode VCSEL", *Electron. Lett.*, vol. 34, pp. 1585–1587, 1998.

[P-54] M. Welker, Knüpfer B, Ch. Oehler, W. Geißelbrecht, G.H. Döhler, C. Jung, D. Wiedenmann, and K.J. Ebeling, "An active smart pixel with low optical input energy, high contrast and high switching speed", in *Proc. CLEO Europe 98, CThB4*, p. 251, Glasgow, UK, Sept., 1998.

[P-55] L. Zei, K. Obermann, K. Petermann, D. Wiedenmann, and K.J. Ebeling, "Turn-on jitter of zero-biased polarization controlled single-mode VCSELs", in *Proc. ECOC '98*, pp. 287–288, Madrid, Spain, Sept., 1998.

[P-56] E. Zeeb, J. Heinrich, M. Rode, K. Pressmar, and D. Seidl, "Compact transceiver module for POF-based bidirectional data buses", in *Proc. POF '98*, pp. 216–221, Berlin, Germany, Oct., 1998.

[P-57] M. Jönck, B. Wittmann, A. Neyer, R. Michalzik, and D. Wiedenmann, "POF-based integrated circuit interconnects", in *Proc. POF '98*, pp. 130–131, Berlin, Germany, Oct., 1998.

[P-58] M. Jönck, B. Wittmann, R. Michalzik, D. Wiedenmann, and A. Neyer, "8$\times$8 POF based interchip interconnection with 2.5 Gbit/s per channel data transmission", in *Proc. ECOC '98*, pp. 35–36, Madrid, Spain, Sept., 1998.

[P-59] M. Grabherr, M. Miller, R. Jäger, R. Michalzik, U. Martin, H. Unold, and K.J. Ebeling, "High power VCSELs - single devices and densely packed arrays", *to be published in IEEE J. Selected Topics Quantum Electron.*, vol. 4, 1998.

[P-60] J. Heerlein, S. Gruber, M. Grabherr, R. Jäger, and P. Unger, "Highly-efficient laterally oxidized λ = 950 nm InGaAs/AlGaAs single-mode lasers", *to be published in IEEE J. Selected Topics Quantum Electron.*, vol. 4, 1999.

[P-61] J. Heerlein, R. Jäger, and P. Unger, "InGaAs-AlGaAs broad-area lasers with high conversion efficiency", *submitted to IEEE Photon. Techn. Lett.*, vol. 11, 1999.

[P-62] C. Jung, R. King, R. Jäger, M. Grabherr, F. Eberhard, R. Rösch, U. Martin, D. Wiedenmann, H.J. Unold, R. Michalzik, and K.J. Ebeling, "64 channel flip-chip mounted selectively oxidized GaAs VCSEL array for parallel optical interconnects", in *Proc. SPIE OPTOELECTRONICS '99 - Vertical-Cavity Surface-Emitting Lasers III*, vol. 3627, San Jose, CA, USA, Jan., 1999.

[P-63] M. Kamp and H. Riechert, "MBE growth of GaN and related compounds", *book chapter in Properties of GaN and related Compounds, edt. J.H. Edgar, S. Strite, I. Akasaki, H. Amano, and C. Wetzel, emis datas review series, INSPEC, IEE UK*, vol. 23, pp. 426–440, 1999.

[P-64] M. Kamp, A. Pelzmann, C. Kirchner, M. Mayer, K.J. Ebeling, M. Leszczynski, I. Grzegory, T. Suski, and S. Porowski, "GaN homoepitaxy for Device Applications (invited)", *MRS Internet J. Nitride Semicond. Res., 451, G.10.2*, 1998.

[P-65] M. Kamp, "Solutions for heteroepitaxial growth of GaN and their impact on devices (invited)", *to appear in Optical and Quantum Electronics (special issue)*, 1999.

[P-66] M. Kamp, "High-resolution PL spectra of donor- and acceptor-bound excitons in homoepitaxial GaN-layers", *GaN workshop continues the substrate search, III-Vs Review*, vol. 11 (6), pp. 42–44, 1999.

[P-67] R. King, R. Michalzik, D. Wiedenmann, R. Jäger P. Schnitzer, T. Knödl, and K.J. Ebeling, "2D VCSEL arrays for chip-level optical interconnects", in *Proc. SPIE OPTOELECTRONICS '99 - Vertical-Cavity Surface-Emitting Lasers III*, vol. 3627, San Jose, California, USA, Jan., 1998.

[P-68] M. Mayer, A. Pelzmann, H.Y. Chung, M. Kamp, and K.J. Ebeling, "Reactive MBE of group III nitrides: high quality homoepitaxial GaN and ultra-violet emitting diodes", *J. Cryst. Growth*, vol. 201/202, pp. 318–322, 1999.

[P-69] R. Michalzik, R. King, D. Wiedenmann, P. Schnitzer, and K.J. Ebeling, "Modeling and application of VCSELs for optical interconnection", in *Proc. SPIE OPTOELECTRONICS '99 - Physics and simulation of optoelectronic devices VII*, vol. 3625, San Jose, California, USA, Jan., 1999.

[P-70] M. Schauler, F. Eberhard, C. Kirchner, V. Schwegler, A. Pelzmann, M. Kamp, K.J. Ebeling, F. Bertram, T. Riemann, J. Christen, P. Prystawko, M. Leszczynski, I. Grzegory, and S. Porowski, "Dry-etching of GaN substrates for high-quality homoepitaxy", *Appl. Phys. Lett.*, vol. 74, pp. 1123–1125, 1999.

[P-71] W. Schmid, F. Eberhard, M. Schauler, M. Grabherr, R. King, M. Miller, E. Deichsel, G. Stareev, U. Martin, R. Jäger, J. Joos, R. Michalzik, and K.J. Ebeling, "Infrared light-emitting diodes with lateral outcoupling taper for high extraction efficiency", in *Proc. SPIE OPTOELECTRONICS '99 - Light-emitting diodes: research, manufacturing, and applications III*, vol. 3621, San Jose, CA, USA, Jan., 1999.

[P-72] P. Schnitzer, M. Grabherr, R. Jäger, F. Mederer, R. Michalzik, D. Wiedenmann, and K.J. Ebeling, "GaAs VCSEL's at $\lambda = 780$ and 850 nm for short distance 2.5 Gb/s plastic optical fiber data links", *IEEE Photon. Techn. Lett., in press*, vol. 11, 1998.

[P-73] D. Wiedenmann, R. King, C. Jung, R.Jäger, R. Michalzik, P. Schnitzer, M. Kicherer, and K.J. Ebeling, "Design and analysis of single-mode oxidized VCSELs for high-speed optical interconnects", *to be published in IEEE J. Selected Topics Quantum Electron.*, vol. 4, 1998.

[P-74] D. Mistele, J. Aderhold, H. Klausing, T. Rotter, O.K. Semchinova, J. Stemmer, D. Uffmann, J. Graul, F. Eberhard, M. Mayer, M. Schauler, and M. Kamp, "Influence of pre-etching on specific contact parameters for metal-GaN contacts", *to be published in Semicond. Science and Techn.*, 1999.

[P-75] I. Daumiller, C. Kirchner, M. Kamp, K.J. Ebeling, L. Pond, C.E. Wetzel, and E. Kohn, "Evaluation of AlGaN/GaN HFETs up to 750 °C", *to be published in Electronic Device Lett.*, 1999.

[P-76] C. Bozdog, H. Przybylinska, G. D. Watkins, V. Härle, F. Scholz, M. Mayer, M. Kamp, R.J. Molnar, and B. Molnar, "Optical detection of electron paramagnetic resonance in electron-irradiated GaN", *submitted to Phys. Rev. B*, 1999.

[P-77] A. Bramati, J.-P. Hermier, A.Z. Khoury, E. Giacobino, P. Schnitzer, R. Michalzik amd K.J. Ebeling, J.Ph. Poizat, and Ph. Grangier, "Spatial distribution of the intensity noise of a VCSEL", *submitted Electron. Lett.*, 1999.

[P-78] P. Prystawko, M. Leszczynski, A. Sliwinski, H. Teisseyre, T. Suski, M. Bockowski, S. Porowski, J. Domagala, C. Kirchner, A. Pelzmann, M. Schauler, and M. Kamp, "Epitaxy of ternary nitrides on GaN single crystals", *J. Cryst. Growth*, vol. 198/199, pp. 1061–1065, 1999.

[P-79] R. Cheung, S. Withanage, R.J. Reeves, S.A. Brown, I. Ben-Yaacov, C. Kirchner, and M. Kamp, "Reactive ion etch-induced effects on the near-band-edge luminescence in GaN", *accepted for Appl. Phys.*, 1999.

[P-80] K. Kornitzer, M. Grehl, K. Thonke, R. Sauer, C. Kirchner, V. Schwegler, M. Kamp, M. Leszczynski, I. Grzegory, and S. Porowski, "High-resolution PL spectra of donor- and acceptor-bound excitons in homoepitaxial GaN-layers", *submitted to Phys. Rev. Lett.*, 1999.